



Title	希土類金属間化合物の強磁場磁性
Author(s)	杉山, 清寛
Citation	大阪大学, 1988, 博士論文
Version Type	VoR
URL	https://hdl.handle.net/11094/978
rights	
Note	

The University of Osaka Institutional Knowledge Archive : OUKA

<https://ir.library.osaka-u.ac.jp/>

The University of Osaka

HIGH FIELD MAGNETISM
OF
RARE EARTH INTERMETALLIC COMPOUNDS

by

Kiyohiro SUGIYAMA

DISSERTATION IN PHYSICS



THE OSAKA UNIVERSITY
GRADUATE SCHOOL OF SCIENCE
TOYONAKA, OSAKA

HIGH FIELD MAGNETISM
OF
RARE EARTH INTERMETALLIC COMPOUNDS

by

Kiyohiro Sugiyama

DISSERTATION IN PHYSICS

THE OSAKA UNIVERSITY
GRADUATE SCHOOL OF SCIENCE
TOYONAKA, OSAKA

March, 1988

CONTENTS

PART I. MULTI-LAYER LONG-PULSE MAGNET

ABSTRACT	1
§ 1 INTRODUCTION	2
§ 2 DESIGN AND CONSTRUCTION OF MAGNET	6
§ 3 ENERGY SOURCE	22
§ 4 DATA PROCESSING SYSTEM	29
§ 5 MAGNET AND MAGNETIC FIELD CHARACTERISTICS	37
§ 6 HIGH FIELD MAGNETIZATION OF CONDUCTIVE MATERIALS	49
APPENDIX A	57
APPENDIX B	58
APPENDIX C	59
APPENDIX FIGURES	60
REFERENCES	64

PART II HIGH FIELD STUDIES OF SOME INTERMETALLIC COMPOUNDS

- A - HIGH FIELD MAGNETIZATION OF GdB_6

ABSTRACT	66
§ 1 INTRODUCTION	67
§ 2 CRYSTAL STRUCTURE AND MAGNETIC PROPERTIES OF GdB_6	68
§ 3 EXPERIMENTAL PROCEDURES AND THE RESULTS	70
§ 4 MAGNETIC STRUCTURE OF GdB_6	77
§ 5 DISORDERED MODEL	85
REFERENCES	96

- B -	FIELD-INDUCED METALLIC STATE IN YbB_{12}	
	UNDER HIGH MAGNETIC FIELD	
	ABSTRACT	98
§ 1	INTRODUCTION	99
§ 2	ELECTRIC AND MAGNETIC PROPERTIES	101
§ 3	EXPERIMENTAL PROCEDURES	105
§ 4	EXPERIMENTAL RESULTS	108
§ 5	FIELD-INDUCED METALLIC STATE AND	116
	THE MAGNETIZATION	
	REFERENCES	123
- C -	HIGH FIELD PROPERTIES OF	
	HIGH- T_c SUPERCONDUCTORS	
	ABSTRACT	125
§ 1	INTRODUCTION	126
§ 2	CRYSTAL STRUCTURE OF 123-COMPOUNDS AND	127
	THE SUPERCONDUCTING PROPERTIES	
§ 3	EXPERIMENTAL PROCEDURE	130
§ 4	UPPER CRITICAL FIELD H_{c2}	134
	AND NORMAL RESISTIVITY	
	REFERENCES	150
	ACKNOWLEDGEMENTS	153

PART I

MULTI-LAYER LONG-PULSE MAGNET

ABSTRACT

A long-pulse magnet with the pulse width of 20~40 msec has been designed and constructed. The maximum field is 400 kOe (40 Tesla) and the magnet is complementally used for the standard maraging-steel short-pulse magnet with the pulse width of 0.4 msec up to 700 kOe. The new magnet is effective for single crystal measurements of metals and alloys with the electrical resistivity of the order of micro-ohms for which the short-pulse magnet is not applicable because of the Joule-heating due to field -induced eddy current.

The long-pulse magnet is designed based on the multi-layer theory of the magnet and two-layer polyhelical winding with Cu-Cr,Zr wire is adopted. Highly qualified pulse field with the uniformity of more than 99.7 % in a volume of 1 cm³ is obtained.

The magnetic field generation and various measurements are controlled and data-processed by a computer-control system which is also applicable to the maraging-steel magnet.

Applications of the long-pulse magnet have been done for some intermetallic compounds and typical magnetization data are presented.

§ 1 INTRODUCTION

There has been a growing interest in the production and application of strong magnetic fields in recent years. Since successful generation of high magnetic fields up to 320 kOe by Kapitza using a motor generator in 1924,¹⁾ various methods to generate high magnetic fields have been proposed and developed. After the pioneer work by Kapitza, Wall produced 200 kOe pulsed magnetic field using a capacitor bank²⁾ and Bitter constructed a D.C. high field magnets at MIT.³⁾ Nowadays, the superconducting magnet can be used to produce D.C. field up to 175 kOe. For higher D.C. field up to 311 kOe, it is now available to use the hybrid magnet,⁴⁾ i.e., a combined magnet of the Bitter type and a superconducting magnets. However, it is now difficult to produce the D.C. field higher than 350 kOe and much higher fields have been obtained only by the pulsed systems.

So far, magnetic fields higher than 1 MOe were obtained only in a few microseconds by using a small one-turn coil with high current rate and by means of field compression methods utilizing chemical implosive power or electromagnetic force.⁵⁾ In these methods, the magnetic fields are produced with sacrifices of coils and samples, i.e., coils and samples are broken in each shot of magnetic fields due to the implosive or electromagnetic force acting on the coils. Furthermore, the short duration time limits wide application of these fields to various precise measurements.

In 1975, Date proposed a new method to produce a strong magnetic field without destroying coils.⁶⁾ The point is to use a

multi-layer coil in which the current density is controlled so as to keep the force acting on each layer to be equal within the material strength. He designed and constructed magnets based on his idea and produced a field of 1.07 MOe in a bore of 2 mm without coil destruction.^{7), 8)} The coils are cut out of one block of maraging steel which is the strongest steel at present. For practical use, one-layer magnets with 500 kOe in 60 mm bore and two-layer magnets with 700 kOe in 20 mm bore are available with time duration of 0.4 msec in the High Field Laboratory, Osaka University.⁹⁾ In the facility, magnetization, magnetoresistance, magneto-optics and far-infrared ESR measurements have been carried out for various of samples of gas, liquid and solid phases. These pulse magnets are suitable for the measurements of insulators, semiconductors and low conductive metals. In the case of conductive samples such as pure metals, powdered specimens are used to avoid Joule heating due to eddy current.

Recently, increasing interests are focused on highly conductive materials with 4f- and 5f-electrons, such as the dense Kondo system, heavy fermion system and high-Tc superconductors.^{10), 11)} Bulky samples such as single crystals of these conductive materials are difficult to measure by the standard maraging-steel short-pulse magnet of the pulse width of 0.3~0.4 msec. For example, URu_2Si_2 with the thickness of 0.5 mm at 1.3 K shows the temperature increase of about 10 K at the peak field of 500 kOe. The magnetocaloric effect due to paramagnetic impurities is also not negligible. Accordingly, it is necessary to design and construct a new magnet with longer pulse duration to

cover the wide range of sample resistivity with appropriate sample size.

The Amsterdam group constructed a pulse magnet up to 400 kOe which is driven by a motor-generator and is cooled in liquid neon.¹²⁾ Their magnet can provide the width of 600 msec, i. e. about one second pulse field with the pulse-form control system. However, their construction cost is expensive and the running cost, for example, the cost of liquid neon is also expensive and the handling is not easy compared with liquid nitrogen. Considering these facts, we decided to construct a new multi-layer long-pulse magnet with the width of about 20~40 msec which is between the pulse widths of the maraging steel magnet and the Amsterdam magnet.

The basic requirements for the design of the new magnet is similar to those of the short-pulse magnets. The magnet should be strong against the electromagnetic force, easy to use with high precision magnetic measurements. A strong magnet is basically realized by the multi-layer structure as is in the short pulse magnet and the easy handling is obtained by keeping enough space at liquid helium temperatures. The precise experiment can be done by producing highly uniform magnetic field.

The development of the long-pulse magnets and their applications are described in this paper. Designs and constructions of the long-pulse magnets are presented in § 2 and designs and techniques of the capacitor bank are in § 3. In section 4, the data processing system is evolved. Section 5 shows the characteristics of the magnets and its field

generation. The applications of the magnet to the measurements of low conductive materials are presented in section 6.

Appendices A~C are devoted to the computer programs of data processing and typical data-handling-processes are presented by Figs.A1~A4.

§ 2 DESIGN AND CONSTRUCTION OF MAGNET

The basic method of the pulsed magnet design has been established especially for usual polyhelical solenoid. Accordingly, the main interests in the magnet design come from the requirements in the scientific problems to be studied. One of them is the necessity in the metal physics. As is briefly described in the introduction, new aspects of many metallic and intermetallic materials appear after the construction of the multi-layer maraging steel magnet in Osaka University.¹³⁾ Especially, striking developments in the rare earth and actinide compounds attract much attention. The well known key words in these compounds are valence fluctuations, dense-Kondo state, heavy Fermions and high T_c superconductors. The related materials usually have the residual electrical resistivity of several micro ohms for their highly qualified specimens. When our maraging steel magnet with the pulse width of 0.3~0.4 msec is used for these materials, temperature increase due to the induced eddy current is serious and the experiments are limited to the thin films and powder specimens. Generally speaking, there are three undesirable effects for metal study in the pulse field measurements. One of them is the magnetic field inhomogeneity produced by the skin effect. The second one is the Joule heating due to induced shielding electrical current and the last one is the magneto-caloric effect due to magnetic impurities or host spin itself. The first effect is not so serious and common in metals. The last one depends on the materials and the method of avoiding the magneto-caloric effect has been investigated and

reported.¹⁴⁾ So it is out of the present considerations.

We decided to construct a long pulse magnet up to 400 kOe with the pulse width of 20~40 msec by considering various requirement in metal physics and needs of many users. This magnet covers a new region of material conditions. The effectiveness of this magnet is shown in Fig.1 where newly measurable material condition is shown. Assuming the specific heat and the density of copper metal, the lines of temperature increase of 1 K due to the Joule heating at 4.2 K under the pulsed field of 400 kOe are drawn in Fig.1 for the standard maraging steel magnet and newly designed magnet, respectively. If the resistivity of 1 m Ω cm is assumed for the material, the sample thickness should be less than 0.1 mm for the maraging steel magnet while more than 1 mm is allowed for the new magnet. Moreover, materials with the resistivity of about 10 $\mu\Omega$ cm, which is the standard value for most heavy Fermion and dense Kondo materials, are measurable when the thickness is of the order of 0.1 mm.

The next problem to be decided is the size of the magnet and the corresponding capacity of the energy source. There are many conventional polyhelical pulsed magnets of about 300 kOe in the world. Most of these magnet have the energy source of 10~100 kJoules. The magnet size is limited by the used energy. We set the energy of 500 kJoules for the capacitor bank. The reason is that enough large space should be kept for precise measurements. Moreover, it is theoretically clear that the multilayer magnet is effective to have a successive increase in the field intensity. Two-layer polyhelical magnets were designed by considering these

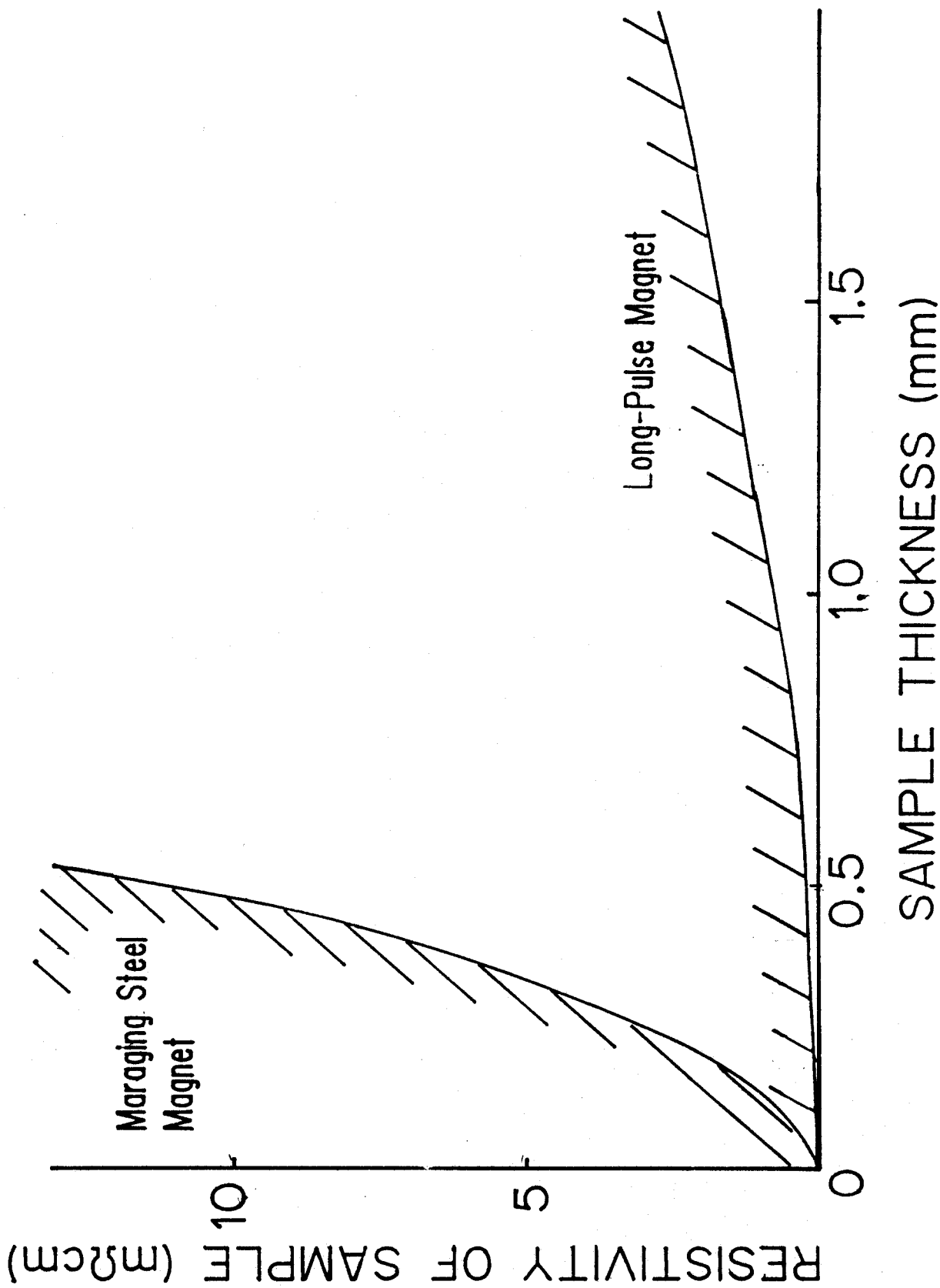


Fig. 1. Measurable region for conductive materials under pulsed magnetic field. Adiabatic temperature increase due to the Joule heating at 4.2 K is assumed to be 1 K where the specific heat and density of Cu metal are used.

conditions with the wire of Cu-Cr,Zr. Various material data are listed in Table I. The electrical resistivity should be lower than that of the maraging steel because the heat increase in the long-pulse magnet is more than ten times larger than the maraging steel magnet. Cu-Cr,Zr and Cu-Al₂O₃ were considered for the candidates and the former was adopted because the latter was difficult to obtain enough amount of the wire with the desired size and quality. The materials data of Cu-Cr,Zr used in the present study are listed in Table II. The standard formulae for designing the pulsed magnet are shown in Fig.2 with a schematic circuit diagram. The design data are listed in Table III.

The electrical resistances of the materials used for coil wire in the typical pulsed magnets are shown in Fig.3 with the standard pulse width for each magnets. As the heating is proportional to the pulse duration, the equivalent-heating condition is shown by straight lines with the tangent given in the figure. The three magnets are of the same order in the heating condition from each other. The temperature increase of the coil is shown in Fig.4 (a) as a function of magnet size. It is noticed that our magnet is designed so as to keep low heat production. In other words, such a soft design was possible under the condition of the large energy source. The expected tensile stress is shown in Fig.4 (b) where the comparison of one and two layer magnets is illustrated. The two-layer magnet is clearly effective for keeping safety force in coils.

Figure 5 shows the practical winding of the magnet. It is important to keep a tight holding of the coil-end because the

Table I Materials Data

(room temp.)

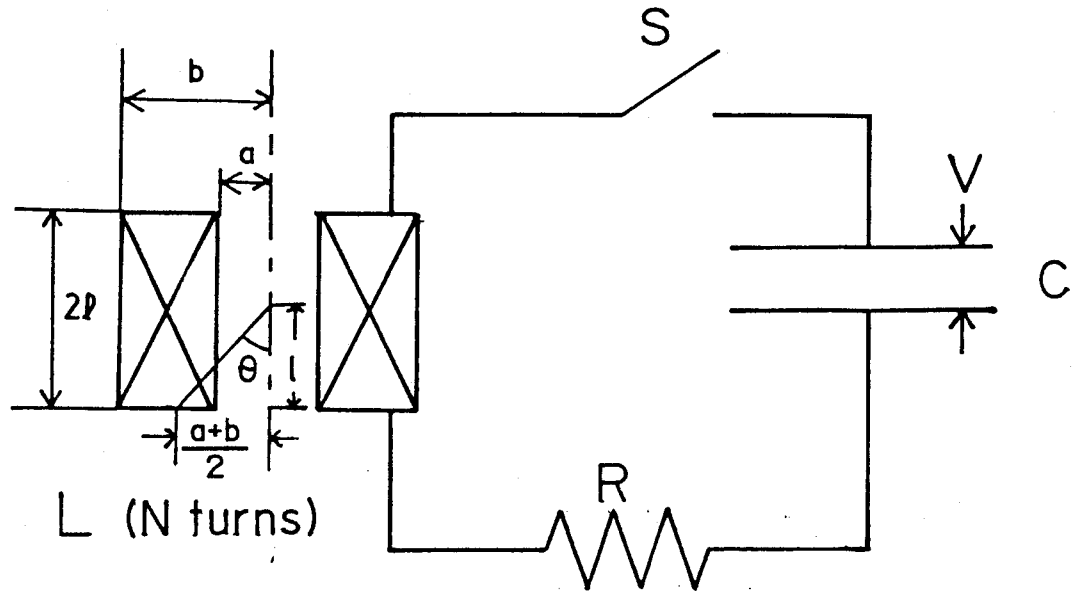
	Electrical Resistivity($\mu\Omega\text{cm}$)	Tensile Strength(kg/mm^2)
Maraging-Steel	50	240
SUS 304L	70	127
70-30 Brass	6.1	66
8%Phosphorous Bronze	13.1	79
Cu 2.0% Be	6.8	190
Cu 0.5% Be	3.4	110
Cu 0.7% Cr	2.0	38
Cu 0.15%Zr	1.8	23
Cu0.5%Cr0.16%Zr	2.1	48
Cu 0.7% Al_2O_3	2.0	48
NbTiTaZr:Cu =1:4	2.1	60
pure Cu	1.7	22.4

Table II Materials Data of Cu-CrZr

Doped metals Cr:0.52% Zr:0.16%
Mg:0.009%

Heat treatment : 450°C×2hr
Cold work rate : 80%

Characters	Values
Elastic modulus	13500 kg/mm
Tensile strength (293K)	62.5 kg/mm
(77K)	75.5 kg/mm
Yield strength	50.1 kg/mm
Hardness	135 Hv
Elongation	5 %
Electrical resistivity (293K)	2.22 $\mu\Omega\text{cm}$
(77K)	0.66 $\mu\Omega\text{cm}$
Thermal expansion coefficient	$1.65 \times 10^{-5} / ^\circ\text{C}$
Specific weight	8.92
Specific heat	0.1 cal/g°C



$$E = \frac{1}{2} CV^2, \quad \omega = \frac{1}{\sqrt{LC}},$$

$$\text{Pulse width } \Delta t = \frac{\pi}{\omega},$$

$$\text{Maximum current } I_0 = \sqrt{\frac{C}{L}} V, \quad (R \ll 2\sqrt{L/C}),$$

$$L \sim \frac{K \mu_0 \pi (a+b)^2}{8l} N^2, \quad \begin{array}{l} K: \text{Nagaoka coefficient} \\ \mu: \text{Vacuum permeability} \end{array}$$

$$R \sim \frac{\pi \rho (a+b)}{2l(b-a)} N^2, \quad \rho: \text{Electrical resistivity}$$

$$\text{Magnetic field } H_0 \sim \frac{IN}{2l} \cos \theta$$

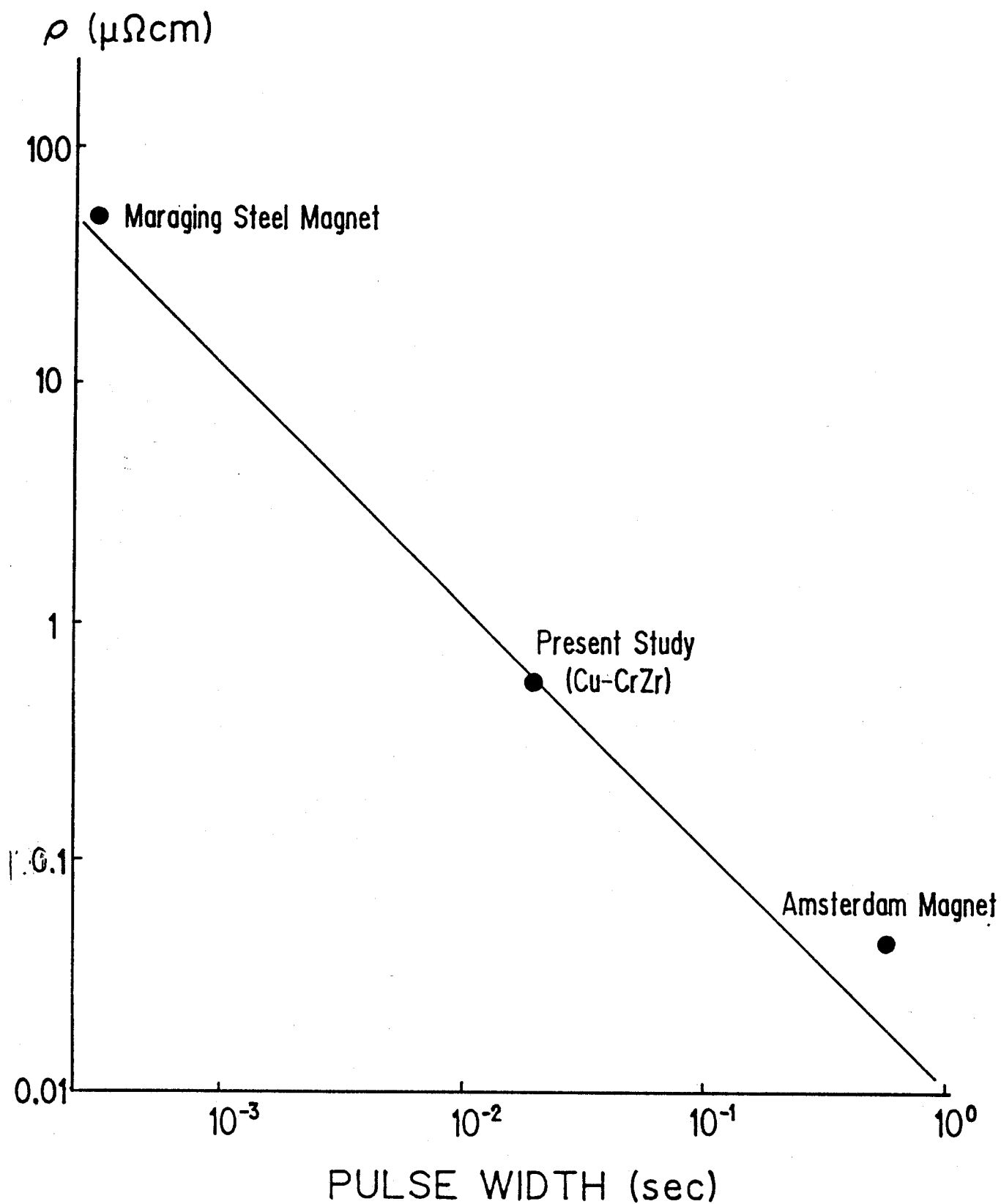
$$\text{Wire crosssection } S = 2l(a+b)/N$$

Fig. 2. Basic relations of the pulsed field generation and characteristics of the solenoid.

Table III Magnet Design Data

	220(2LP)28			170(2LP)18		
	inner coil	outer coil	total	inner coil	outer coil	total
a (mm)	15	42		10	42	
b (mm)	35	110		35	85	
l (mm)	60	75		50	65	
Layer	8	27		10	17	
N (turns)	213	900		220	490	
R ($m\Omega$)	31	440	471	41	222	263
L (mH)	0.53	60	66	0.64	13.1	16.4
Δt (msec)			40			20
H _{max} (kOe)	60	170	230	180	210	390
I ₀ (kA)			3.6			7.2
ΔT (K)			20			53

Fig. 3. Wire resistance and the pulse width of three typical magnets.
The straight line shows an equivalent-heating condition.



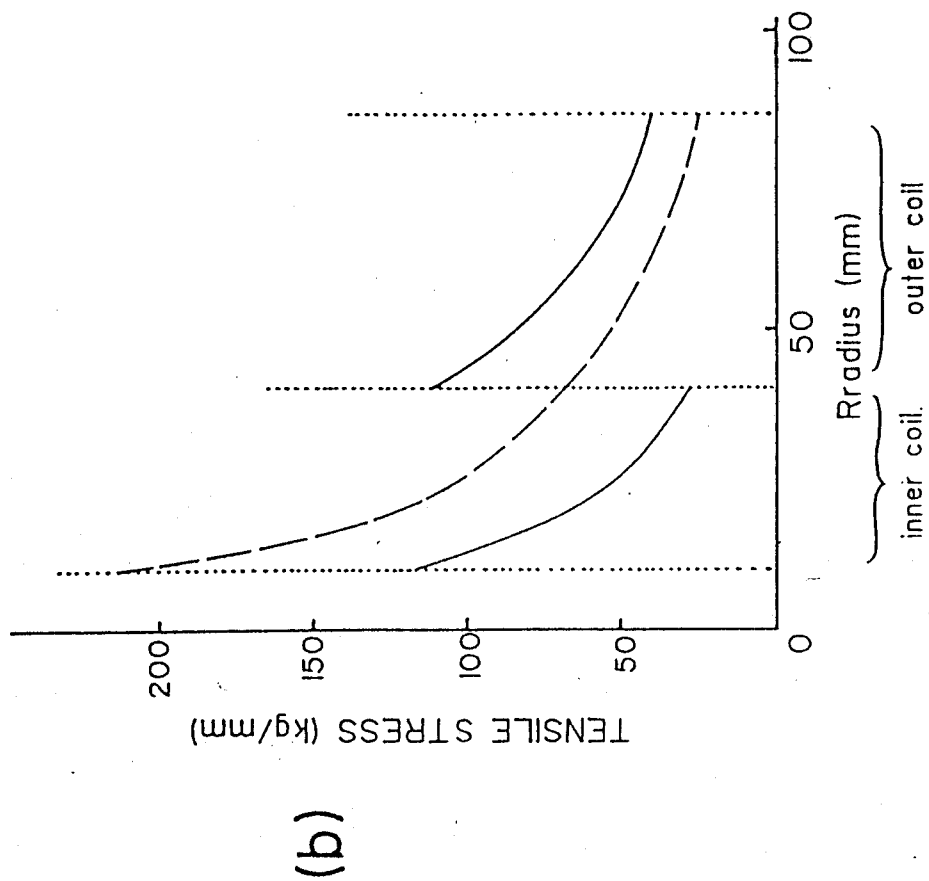
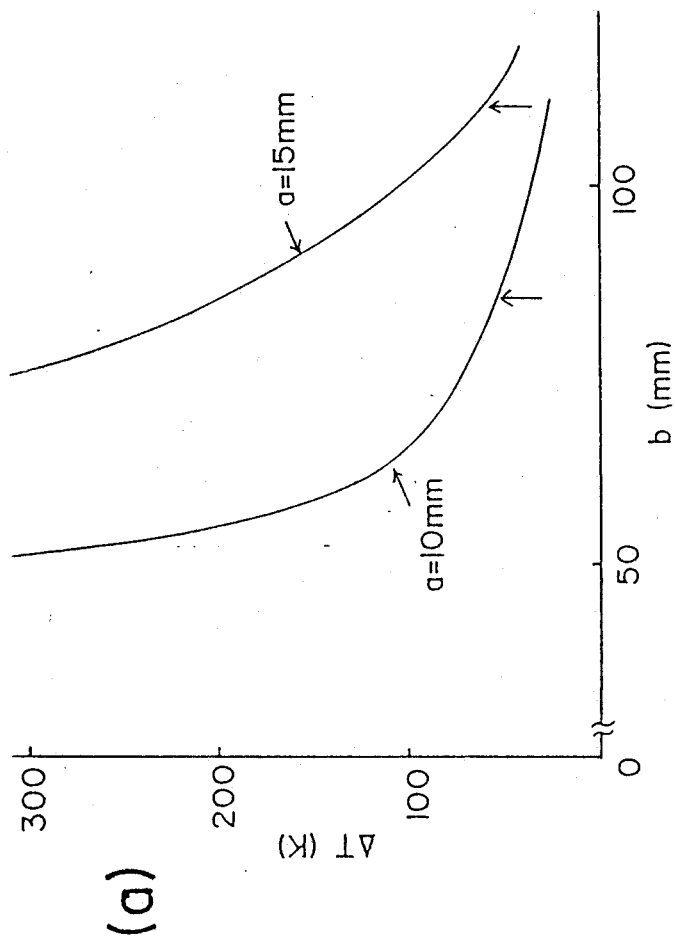


Fig.4. (a) Temperature increase ΔT as a function of magnet volume under the condition of $H_{\text{max}}=400\text{kOe}$, $\Delta t=20\text{msec}$. for $a=10\text{mm}$ and 40msec . for $a=15\text{mm}$, respectively, and $\rho=0.6+0.007\Delta T$. The starting temperature is 77K . Arrows show the testing points.

(b) Radial dependence of the tensile stress acting on the coil wire under the field of 400kOe . Homogeneous current density is assumed. A large stress at the inside of non-separated coil (broken line) is reduced by splitting the coil as are shown by solid lines. In the practical coils, the calculated stress is further reduced by the stainless cover and epoxy resin down to about 50 kg/mm^2 .

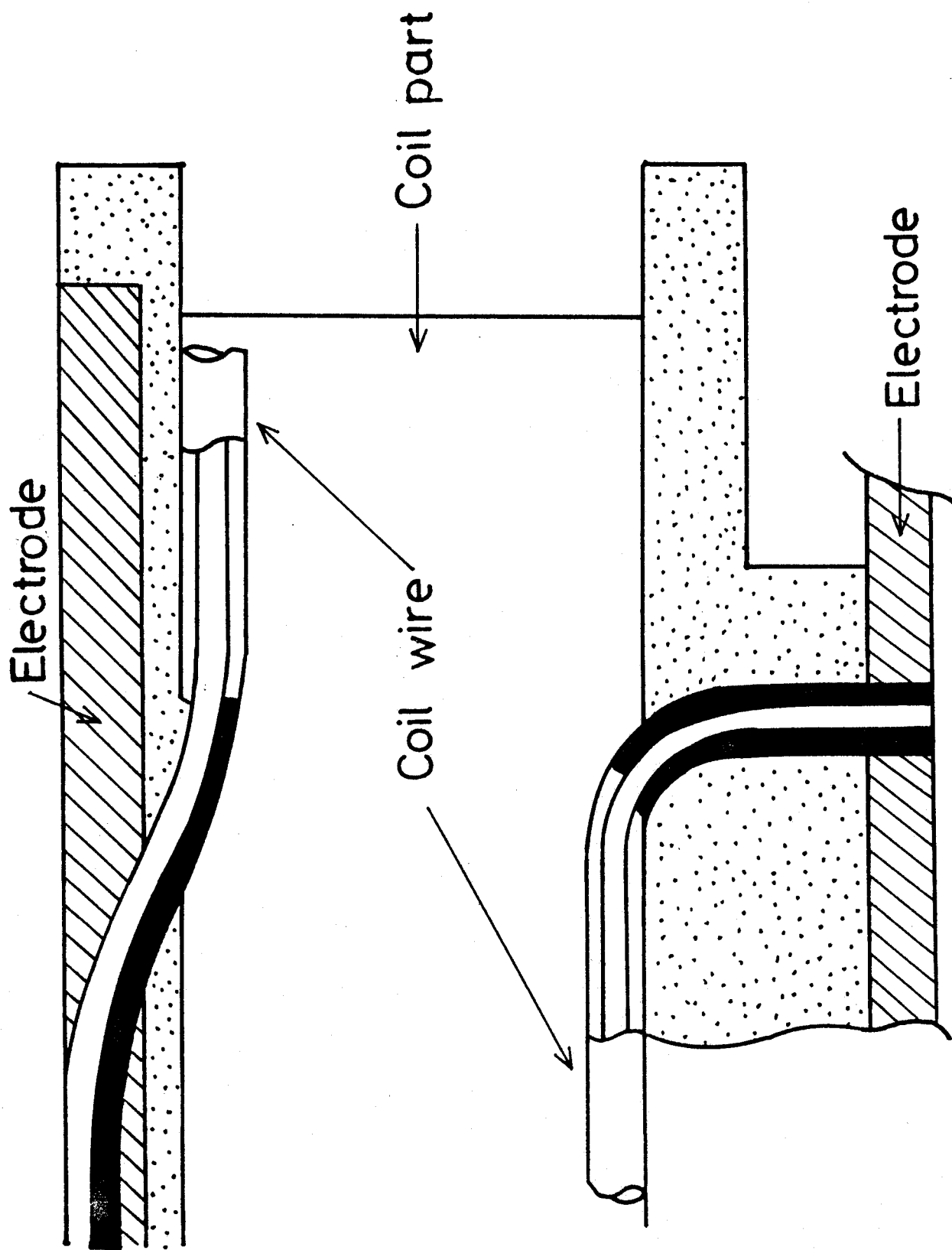


Fig. 5. Coil windings and coil-end holding. Black parts show supporting chips for cable wires. These are welded with wires and electrodes.

movabele coil end is destroyed by the electromagnetic force due to leakage flux of the magnetic field. Cut view of the whole magnet is shown in Fig.6. Inner and outer coils are shown by the cross-marks and the photographs are given in Fig.7. The current input and output are made by stainless plates and coils are suspended by FRP and stainless blocks. The pressurized epoxy-resin is injected into the inner and outer coils in vacuum. Two coils are independetly constructed so that they are easily combined or separeted. The outer coil is protected by the stainless tube.

The coils are cooled down to liquid nitrogen temperature and the cut view of the cryostat vessel is shown in Fig.8 with the photograph. The vessel is conventionally made of stainless bowl with urethane foam heat insulation and no vacuum dewar system is used. About 150 liters of liquid nitorogen are necessary to cool down the magnet and about 3 liters/hour should be added for maintenance. Fig.9 shows the initial cooling data of the magnet by liquid nitrogen.

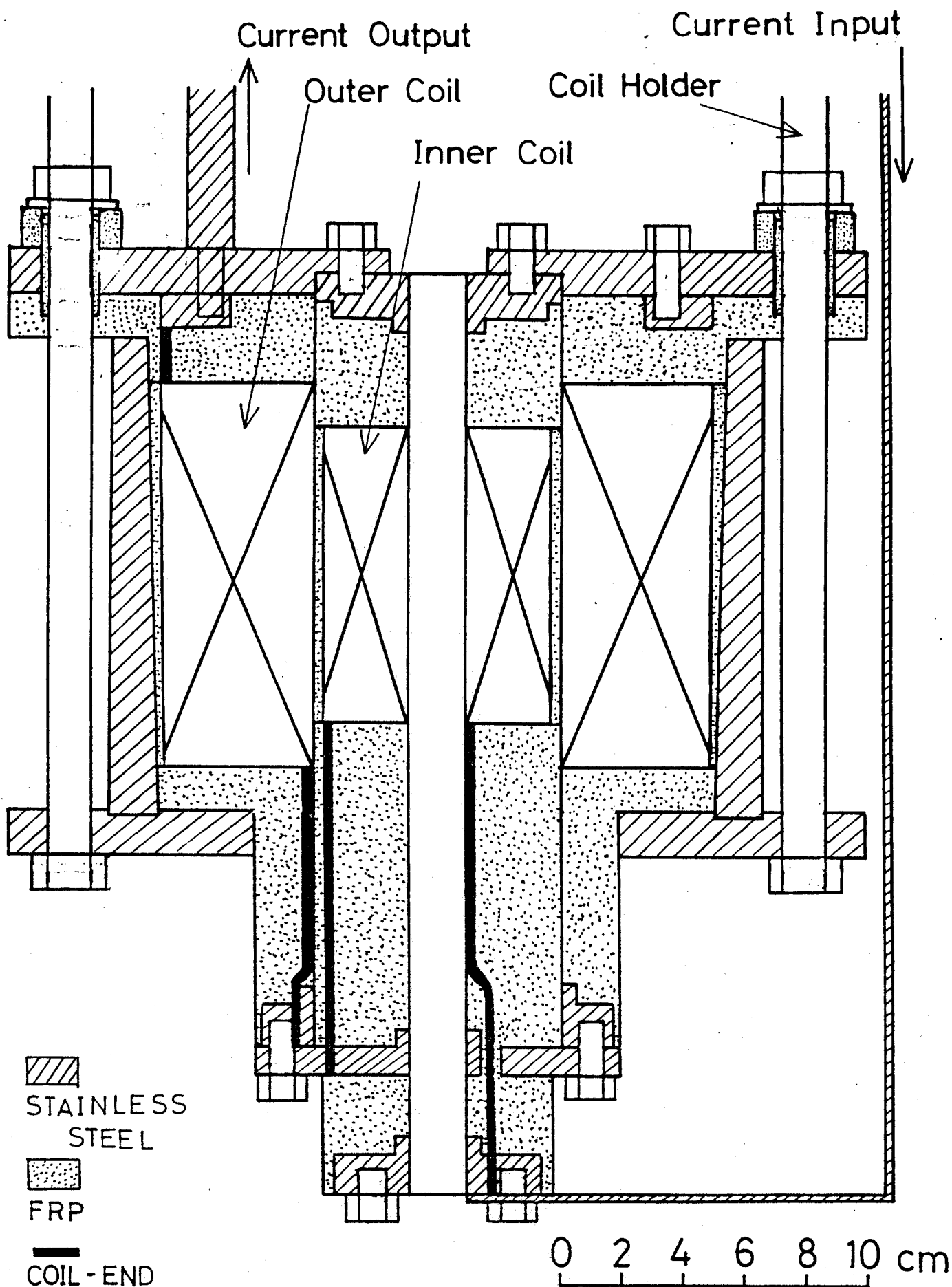


Fig. 6. Cut view of the magnet.

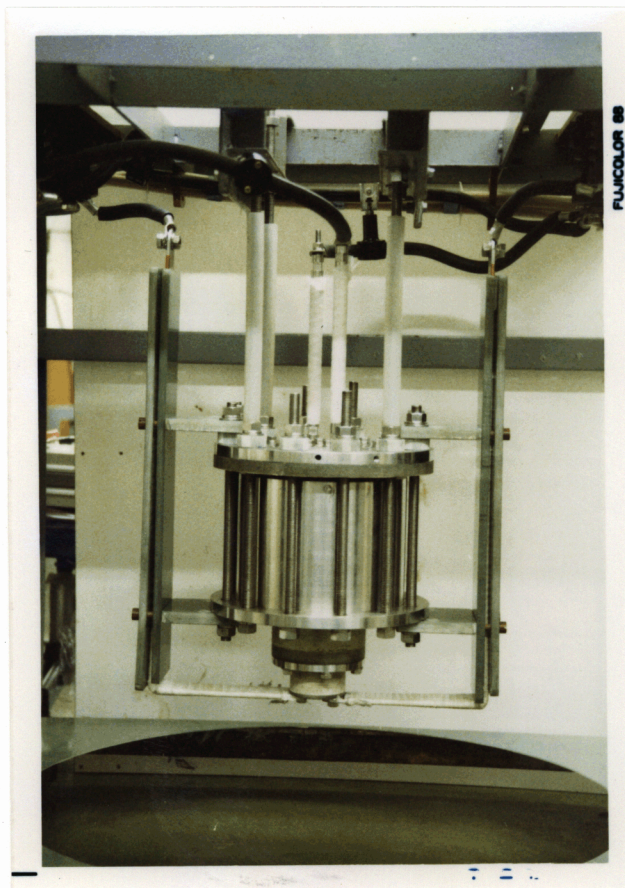
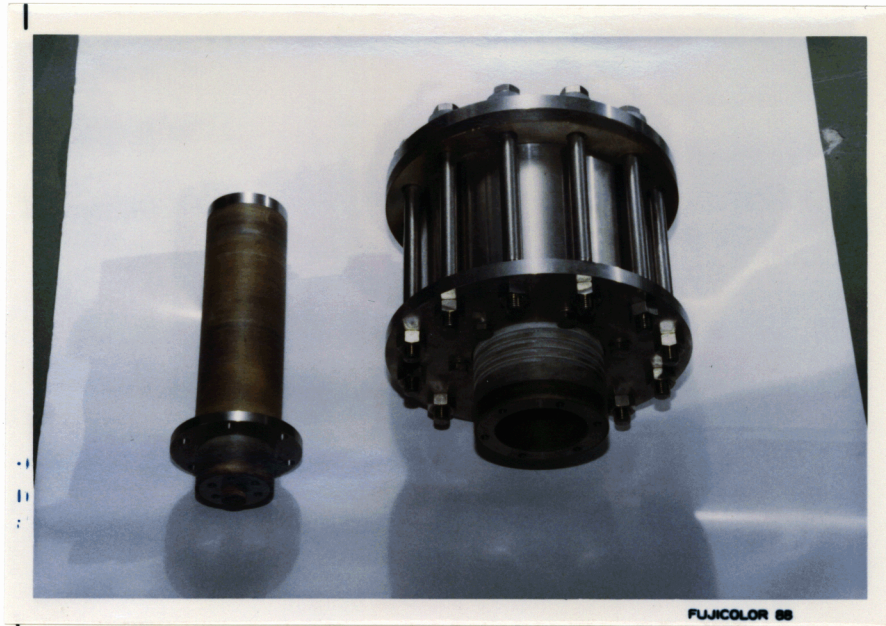


Fig. 7. Photographs of 170(2LP)18 magnet.

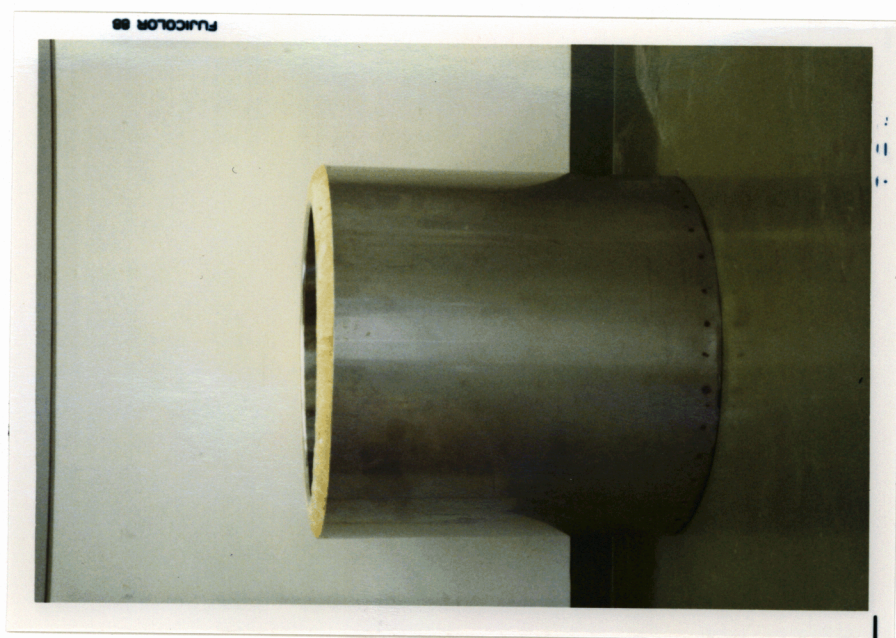
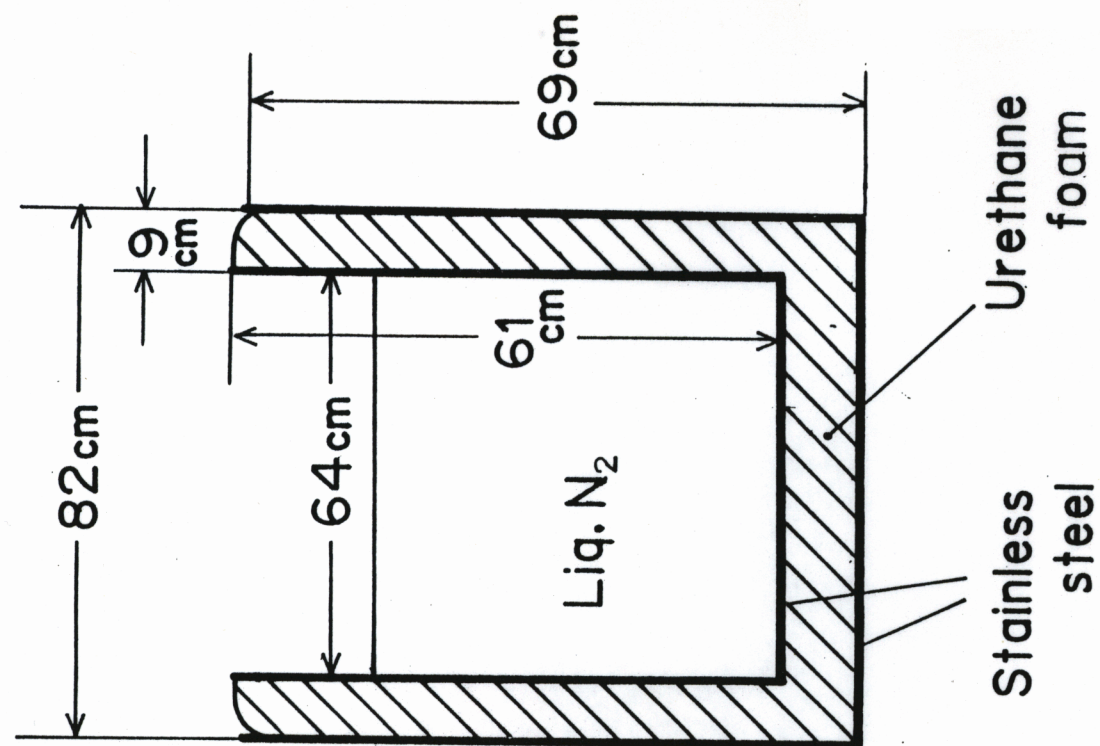


Fig. 8. Cut view and photograph of liquid nitrogen Vessel.

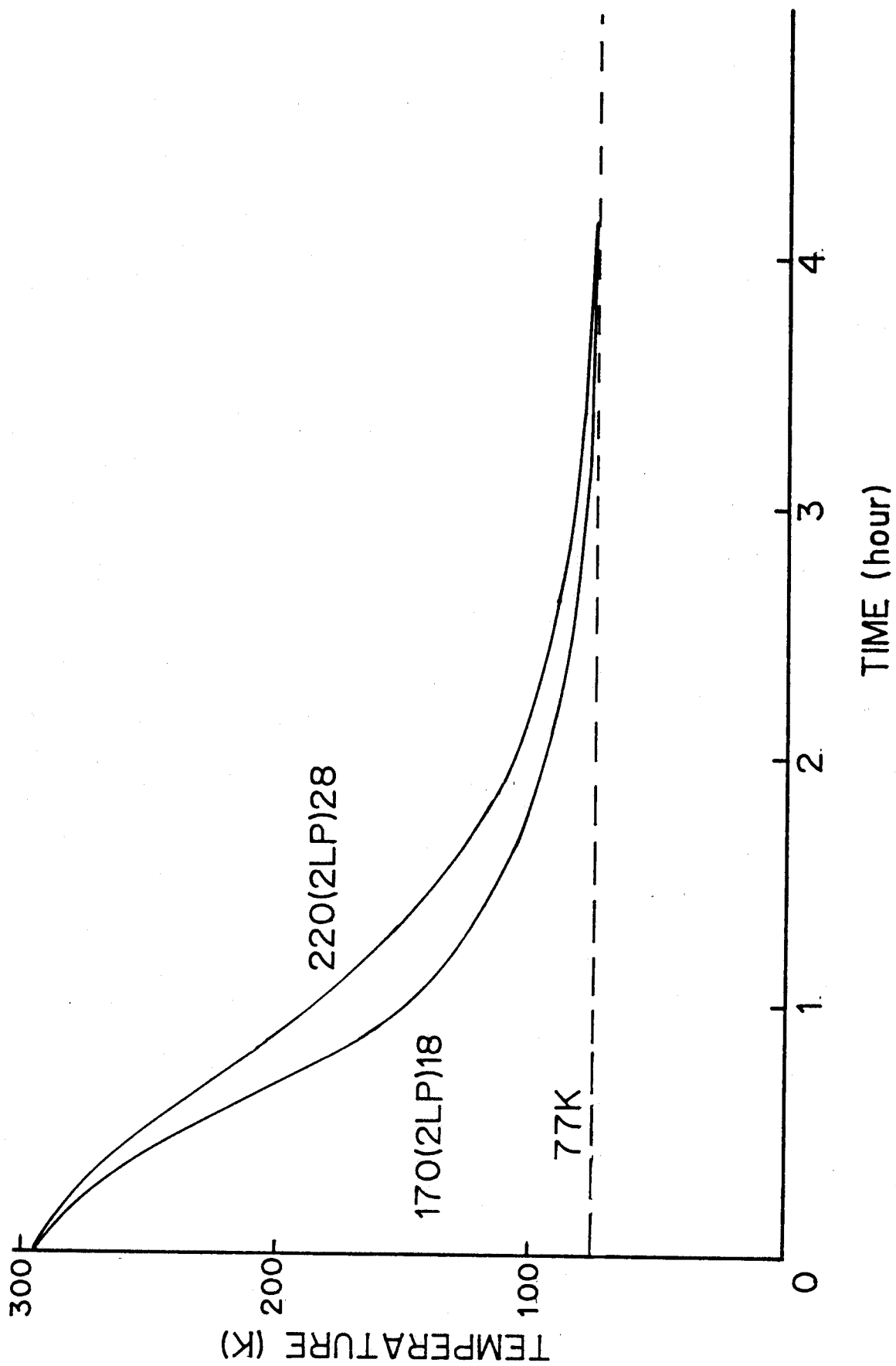


Fig. 9. Cooling characteristics of the magnets.

§ 3 ENERGY SOURCE

A block diagram of newly designed D-1 bank and magnet are shown in Fig.10. This bank is also used to the one-layer maraging-steel magnet developed before. The bank system can be divided into four sections, the air pressure control unit, magnetic field generation unit, high voltage trigger pulse generation unit and synchronous trigger pulse generation unit. The "pressurized spark gap" switches (G1-G4) are used in the new system. The switches of the same mechanism have been used in the D-2 system for several years and show very stable and low noise characteristics. The spark gap switches are pressurized appropriately with dried air from the air pressure control unit to attain high break down voltage and to make smooth switching. The pressures at the inlet and outlet of the gaps, P_{in} and P_{out} , are obtained to be about 1.5 (1.1) and 1.45 (1.05) kg/cm^2 for the charging voltage above (below) 10 kV, respectively. P_{in} and P_{out} for crowbar gaps G2 and G4 are pressurized a little higher than G1 and G3 to avoid accidental breakdown caused by start pulse noise. Dried air flows continuously during the operation through the gap volume and blows out contaminating materials produced by arc discharges. This is effective to avoid premature break down of the gaps caused by moisture and the conducting materials. Pushing a button of SW_2 , trigger pulses are generated by the synchronous trigger generation unit. One of them is directly fed into the high voltage trigger pulse generation unit which amplifies the pulse up to 30 kV and then trigger the start gap switches (G1, G2). Another pulse is delayed and is guided to

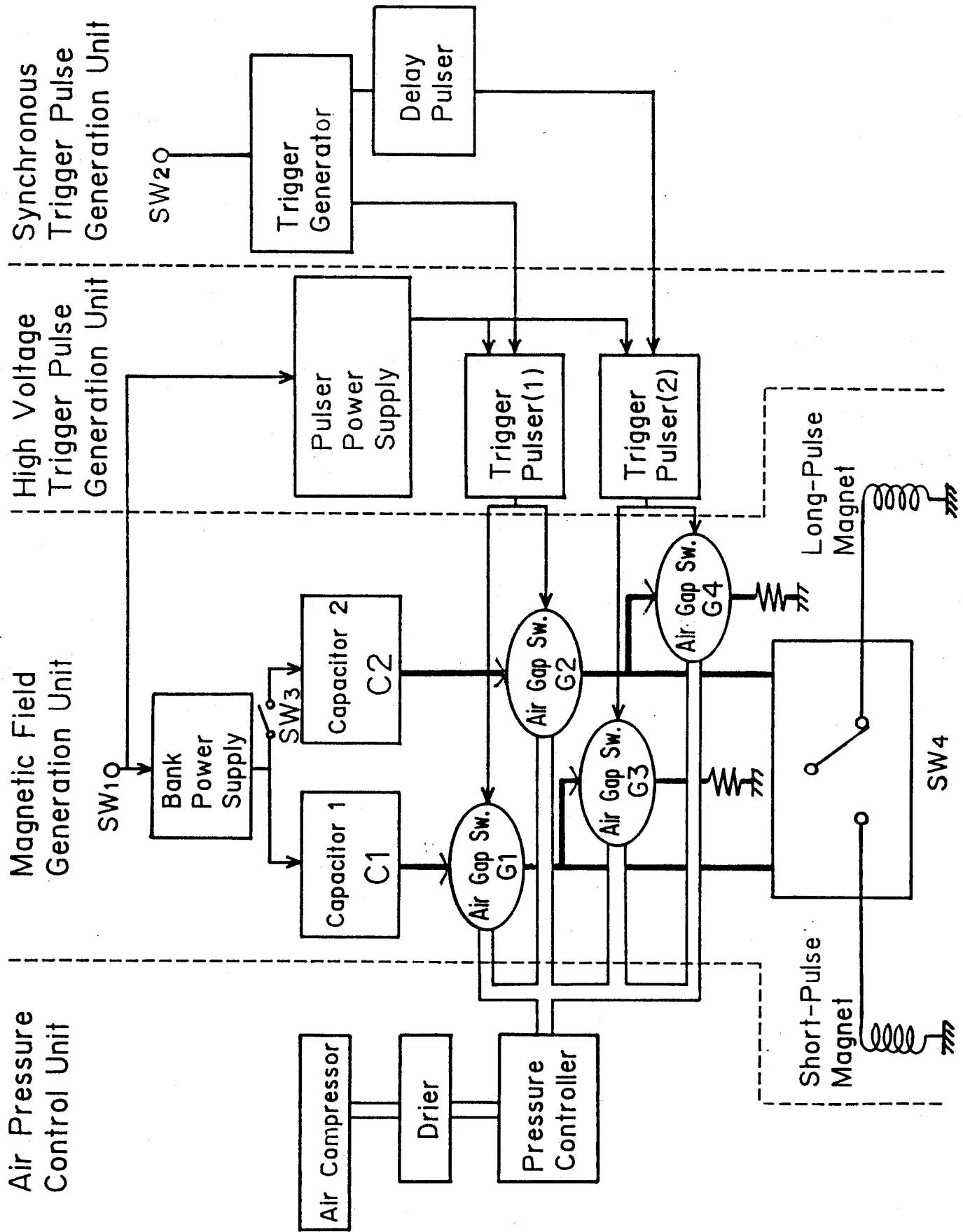


Fig. 10. Block diagram of the D-1 bank.

excite the crowbar switches (G3, G4).

The schematic circuit diagram of the magnetic field generation unit is shown in Fig.11. The bank consists of two 250 kJ units C1 and C2. Each of them has capacitance of 1.25 mF with maximum rating voltage of 20 kV. Total energy is easily selected to be 250 or 500 kJ by changing circuit connections (switch SW_3) depending on the maximum energy. The two magnets of different types can be driven alternatively by changing over the switch SW_4 . Charging of the capacitor begins by closing the switch SW_1 and stops automatically at the pre-set voltage. The capacitors C1 (C2) is discharged through the magnet when the spark gap G1 (G2) is switched on by a high voltage trigger pulse from the trigger pulser. The crowbar gap switch G3 (G4) is turned on just after the maximum field produced to avoid reversal charging of the capacitor and to elongate the pulse width of the magnetic field. Crowbar resistors, R_{cr} , are 1 Ω and 20 m Ω for the long- and the short-pulse magnets, respectively. The load magnet can be selected by changing the contact point of the switch SW_4 . Four types of the combinations of magnets and energies are possible by combining switches SW_3 and SW_4 , i.e., long-pulse magnet with 250 kJ, long-pulse magnet with 500 kJ, short-pulse magnet with 250 kJ and short-pulse magnet with 500 kJ.

The current duration for the long-pulse magnet is about hundred times compared with that of the short-pulse magnet. It is difficult to keep the arcs in the gaps during long-pulse field generation. This problem is solved by adjusting the arcing condition. The differential reactance is used in this new bank system to make sure the simultaneous arcing of the gaps. The

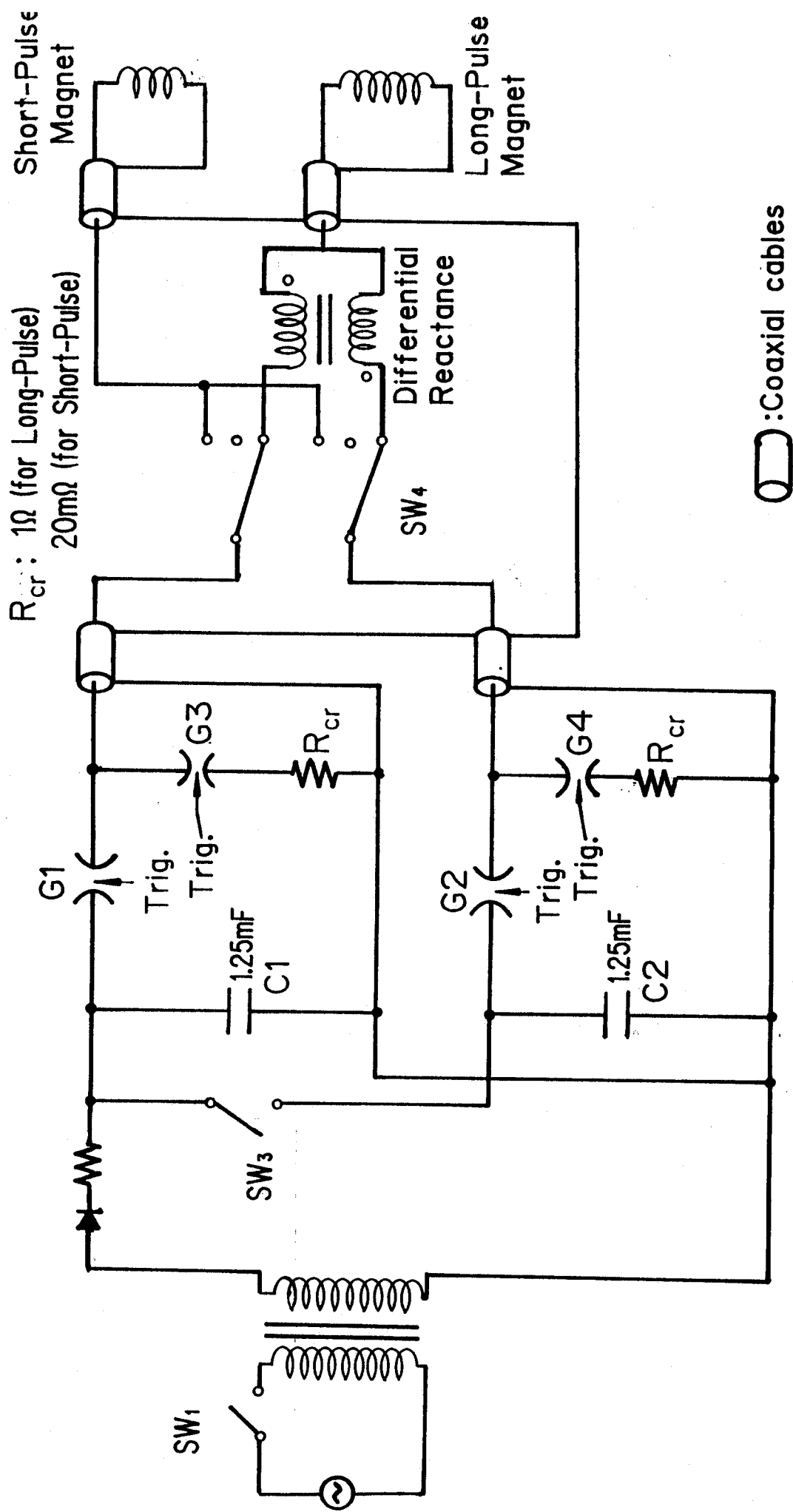


Fig. 11. Schematic circuit diagram of the magnetic field generation unit.

arcing of one gap induces voltage in the reactance of the other gap to start arking in it.

Figure 12 shows charging time required as a function of voltage. It takes three minutes to charge up to 500 kJ. The spark gap G2 is shown in Fig.13.

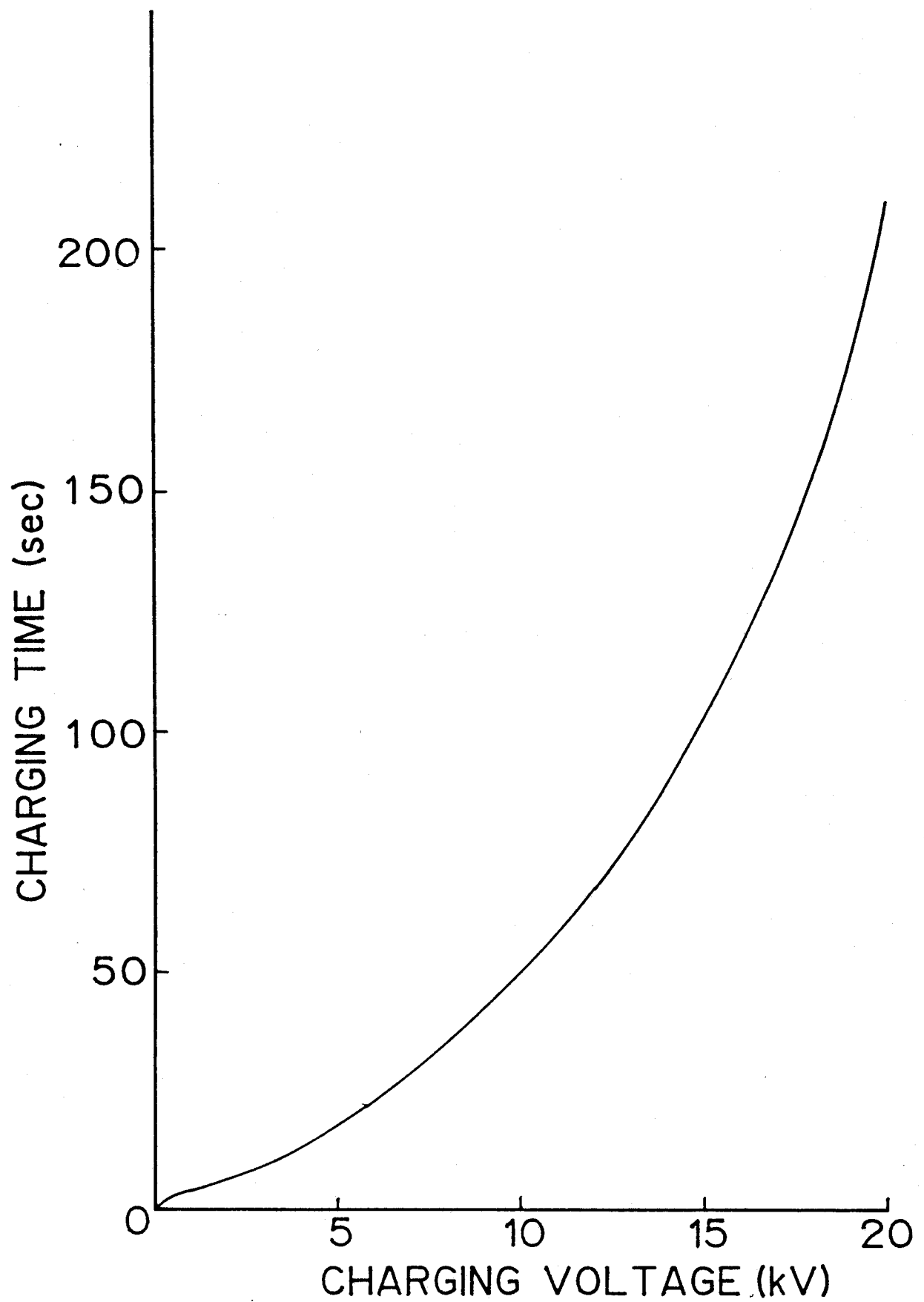


Fig. 12. Charge-up time of the D-1 bank.

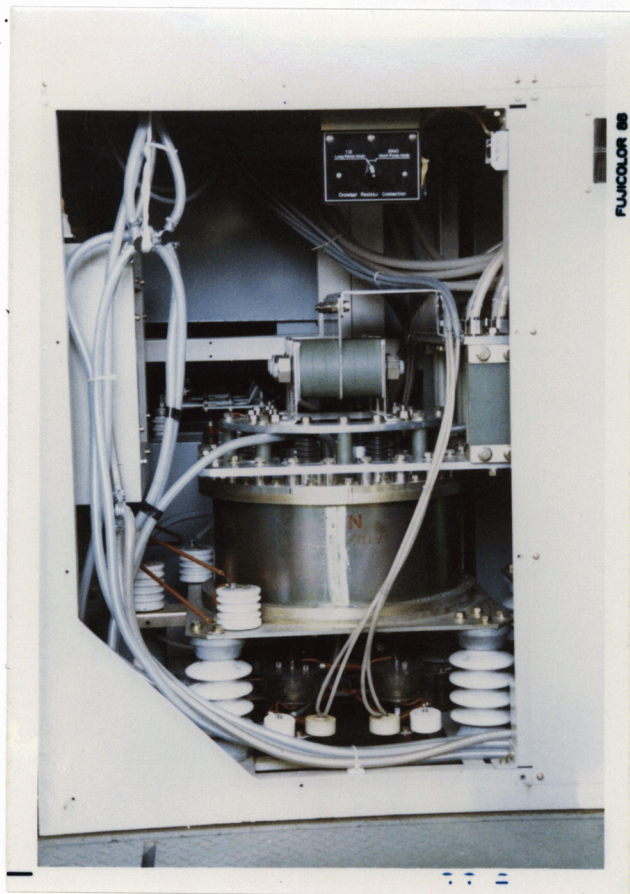


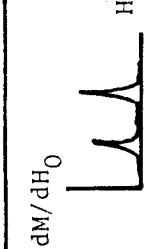


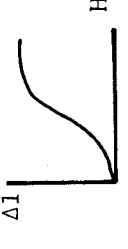




Fig. 13. Photograph of the spark gap switch.

§ 4 DATA PROCESSING SYSTEM

Pulsed signals of various experiments, including field intensity, are stored in a transient recorder (digital recorder) which has 4 k words 12 bit memories with highest sampling speed of 0.1 μ sec. The stored raw data should be converted into useful forms by analyzing related data. The standard methods of basic analysis for several high field experiments are shown in Fig.14. For example, the magnetization measurement is done by picking up induced voltage in the pick up coil, which consists of the true signal dM/dt and the back ground noise $B(t)$ originated to the unbalancing of the coil.¹⁵⁾ To obtain dM/dt , the background $B(t)$ has to be subtracted from the raw data and, if necessary, dM/dt is integrated to get magnetization $M(t)$ or divided with the field signal dH_0/dt to get susceptibility and then displayed as a function of field intensity $H_0(t)$. These data processings are realized by using a microcomputer having large memory size (1 Mbyte). Other functions are also required for the computer to acquire the data from the transient recorder or from a permanent memory (floppy disk system) and an interface function between the computer and the magnet control system is necessary. Basic high field measurements are done by this data processing system developed. However, very good system has been realized for the magneto-optics measurement by the Optical Multi-channel Analyzer (OMA) combined with the spectrometer, so that almost all of the optical experiments are done by using OMA except the measurement of the field intensity. It will be necessary in future to connect OMA with the computer to analyze the spectrum as a function

PHYSICAL OBJECT	APPEARED SIGNAL	DATA PROCESSING	RESULT
H_0	dH_0/dt	$\int (dH_0/dt) dt \rightarrow H_0(t)$	
$M(H_0)$	$\left\{ \begin{array}{l} dM/dt + B(t) \\ B(t) \end{array} \right\}$	$\int (dM/dt) dt \rightarrow M(H_0)$	
		$\{dM/dt + B(t)\} - B(t) \rightarrow (dM/dt)/(dH_0/dt) \rightarrow dM/dH_0$	
$\rho(H_0)$	$\left\{ \begin{array}{l} \rho(t) + B(t) \\ -\rho(t) + B(t) \end{array} \right\}$	$\{\rho(t) + B(t)\} - \{-\rho(t) + B(t)\} \rightarrow \rho(t) \rightarrow \rho(H_0)$	
ESR	$I(t)$	$I(t) \rightarrow I(H_0)$	
STRICTION (OPTICAL)	$\left\{ \begin{array}{l} I(t) \\ I(\Delta l) \text{ calib.} \end{array} \right\}$	$I(t) \xrightarrow{I(\Delta l) \text{ calib.}} \Delta l(t) \xrightarrow{H_0(t)} \Delta l(H_0)$	
BIREFRINGENCE	$I(t)$	$I(t) \xrightarrow{I(H_0)} \text{Rotation } \theta(H_0)$	
OPTICAL SPECTRA	$\left\{ \begin{array}{l} I(\nu, H_0) \\ I_0(\nu, 0) \end{array} \right\}$	$\frac{I(\nu, H_0)}{I_0(\nu, 0)} \xrightarrow{H_0(t)} \text{Spectrum analysis}$	

Δl :displacement, $I(t)$:light intensity, $B(t)$:background.

Fig. 14. Data processing of various physical variables

of field intensity or to process the data in more complicated way. Functions for magnetostriction and magnetobirefringence are complicated and partly depend on the experimental equipments so that they are left to be developed in future.

The principle of designing the data processing system is "simple and easy to use" with high reliability. It is important even though the program is a little complicated, because various users may use it who are familiar and not familiar with the computer. Figure 15 is the block diagram showing the relationship among the magnet, computer system and an operator. The equipment directly related to the data processing system developed is shown by the thick lines. The main part of the data processing system is 16 bit micro-computer, Fujitsu FM-16 β with 1 Mbyte memories. Two types of digital transient recorders, Iwatsu DM-2350 (maximum sampling speed of 20 nsec, memory 10 bit x 4 kwords) and Riken Denshi TCKK-4000E (100 nsec, 12 bit x 4 kwords) are supported by this system. DM-2350 is mainly used for the short-pulse magnet and TCKK-4000E is for the long-pulse magnet. DM-2350 is connected with the computer by GP-IB interface, but TCKK-4000E has no commercially available interface so that an original interface board is designed for this system. The block diagram of this interface board is illustrated in Appendix A. The block diagram and flow line of the program is shown in Fig.16. The data acquisition from the transient recorder to the computer is done automatically when the operator pushes a trigger button for the field generation and data are displayed on the screen. The numerical value of the data at the cursor position is displayed on the screen. Sixteen functions are ready to use

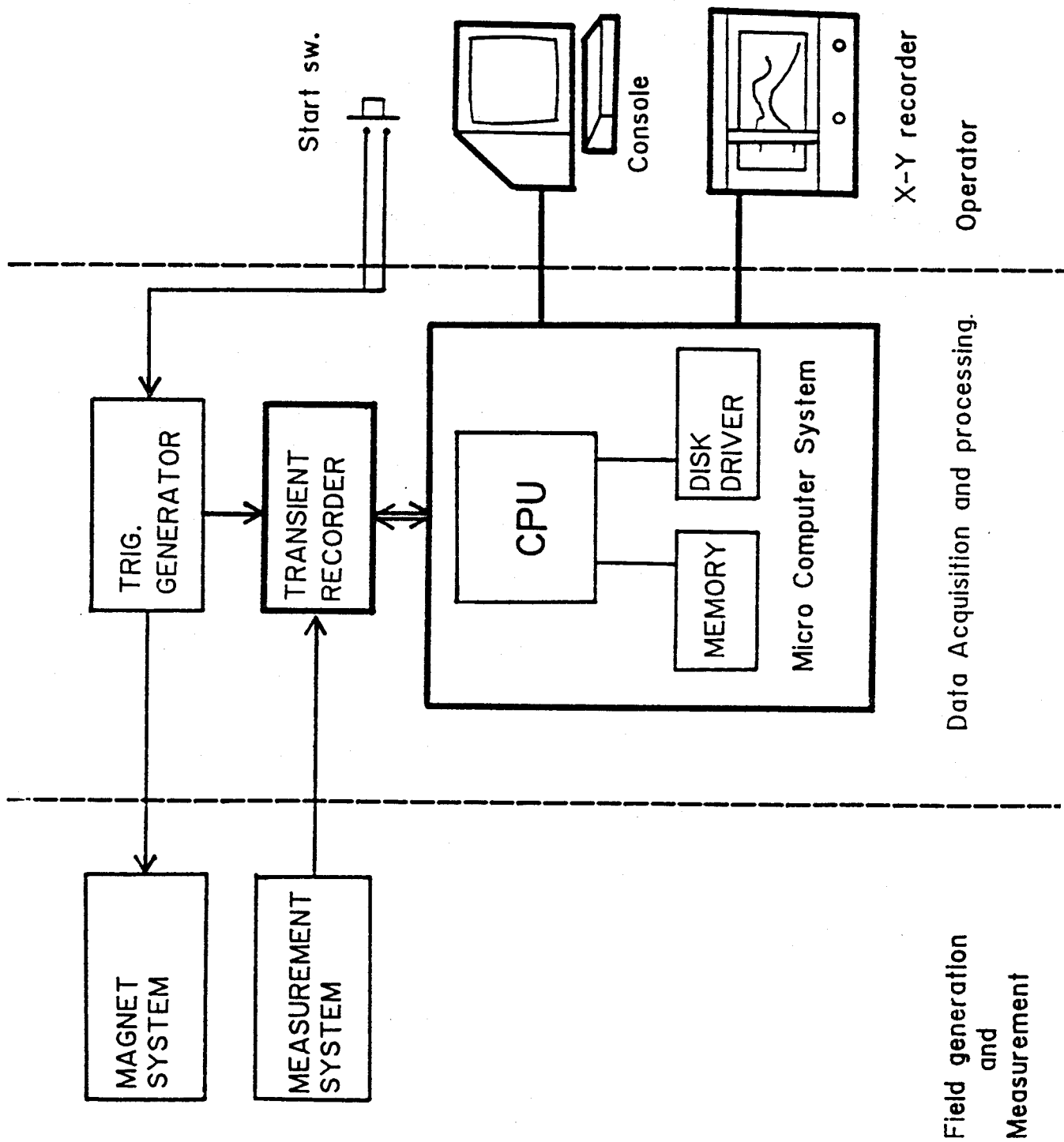


Fig. 15 Block diagram of the data

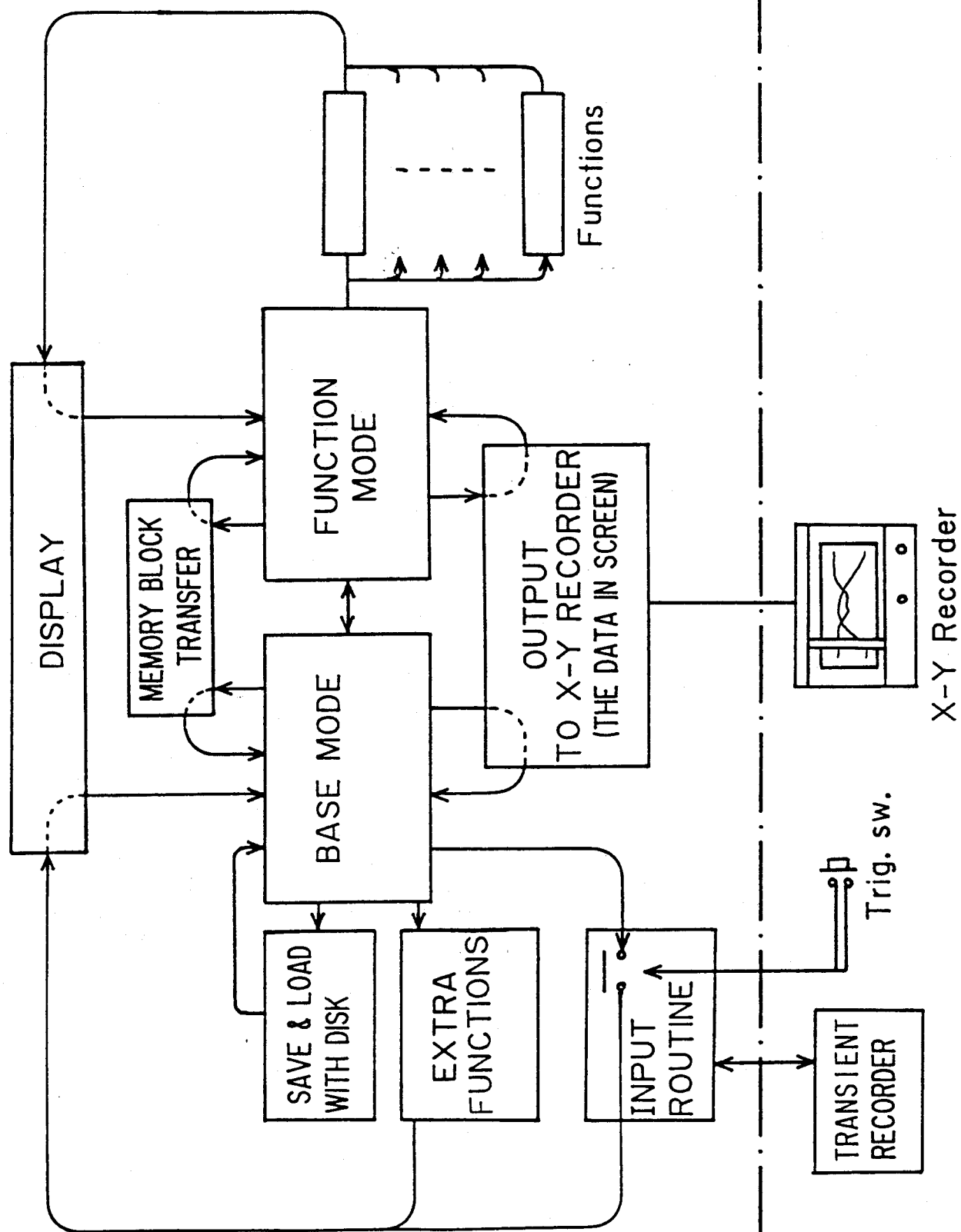


Fig. 16. Block diagram of the data processing program.

in the function mode for the data analysis as mentioned earlier. The list of functions is in Appendix B. The hard copy of the data displayed on the screen is obtained on the chart recorder. The program has sufficient free memories and Ram disk for extra functions to be developed in future as shown in the memory map of Appendix C. The stored data in a floppy disk can be analyzed on the MS-DOS operating system of a different type computer. A photograph of the computer system, transient recorders and magnet control system is shown in Fig.17.

The example of data processing for magnetization measurement is shown in Fig.18. The upper figure shows the hard copy of a raw data measured. DATA 3 and DATA 4 are dH_0/dt and $[dM/dt+B(t)]$, respectively. The lower one shows the magnetization M as a function of H_0 , which is obtained after the subtraction of background $B(t)$ and then integrated to get $M(t)$. Details of a data processing example are shown in Figs.A-1~A-4.

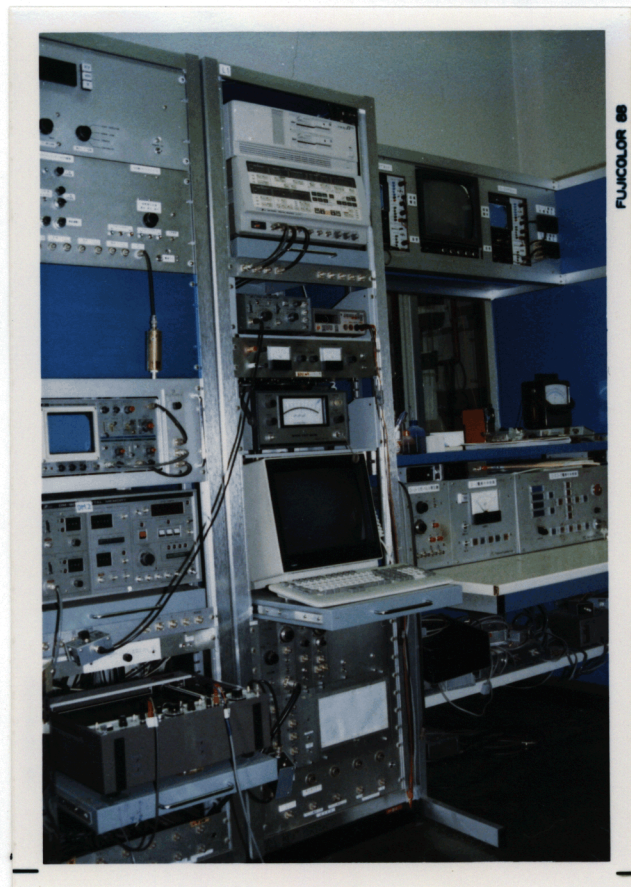
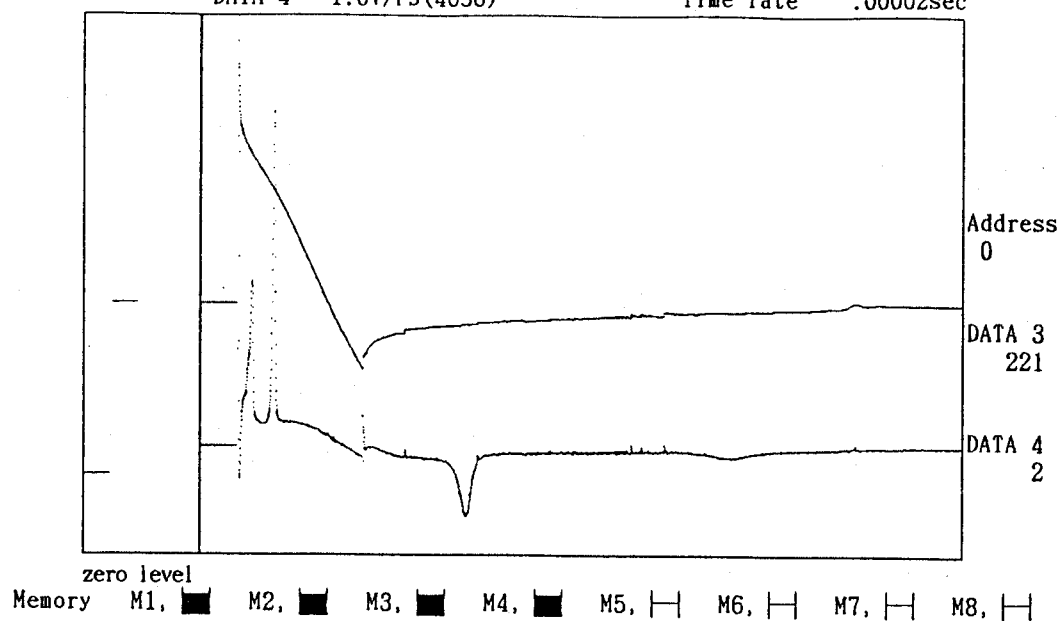


Fig. 17. Photograph of the data processing system.

File name = No file < BASE MODE > Diskette No.= MAG11
 DATA 3 20mV/FS(4096)
 DATA 4 1.0V/FS(4096) Time rate .00002sec



X-Y DISPLAY

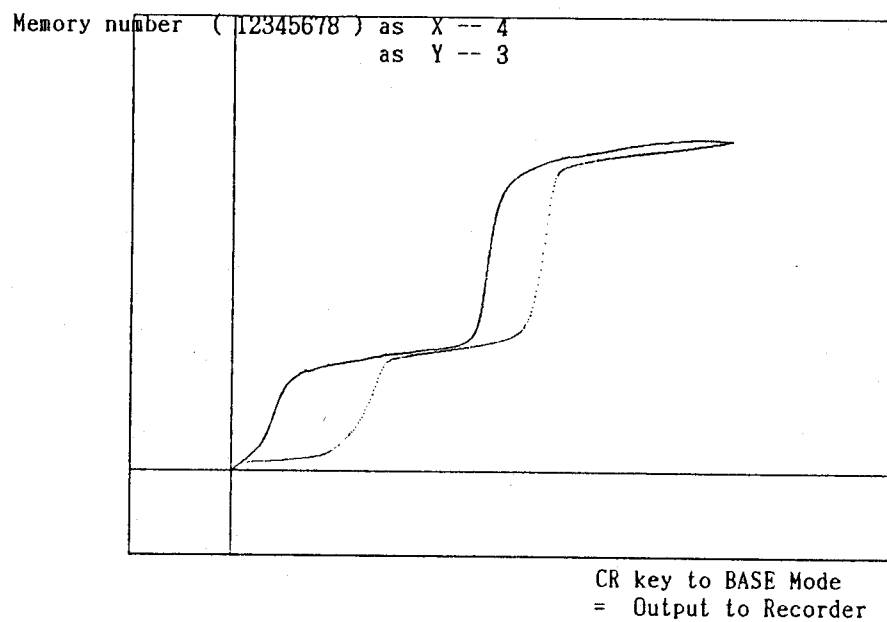


Fig. 18. Example the data processing. The input data of dm/dt given in the upper frame are integrated and displayed by the lower curve.

§ 5 MAGNET AND MAGNETIC FIELD CHARACTERISTICS

Characteristics of the pulsed magnetic fields are examined by using a pick-up coil and the data processing system described in the preceding section. The field pick-up coil is calibrated by utilizing the spin-flop signal of MnF_2 at 4.2 K which is observed at the field of 92.4 kOe.¹⁶⁾ A schematic diagram for the field measurements is shown in Fig.19. dH_0/dt signal from the pick-up coil is sent to the transient recorder and then into the computer system. The signal is numerically integrated and displayed on the screen. Pulse field curves produced by the 170(2LP)18 and 220(2LP)28 long-pulse magnets are shown in Figs. 20 and 21, respectively. The solid line in Fig. 20 is the pulse form with the crowbar circuit operated. The crowbar switches G3 and G4 are closed at about 13 msec after the field ignition. The pulse duration of the field is about 60 msec. The oscillating dotted curve in Fig.20 is obtained when the crowbar switch is open and the duration of half period is 20 msec. This oscillation mode is sometimes used to investigate the hysteresis phenomena. Figure 21 gives longer pulse duration of about 0.1 sec and the half period in the oscillation mode for this magnet is measured to be 40 msec.

Measured values of coil parameters are shown in Table IV. The inductance L and resistance R are obtained by using an LCR meter with the frequency of 120 Hz. The table shows that the magnets are constructed just as expected in the specifications of Table III. No observable change was found on the inductances of the both magnets even after ten shots of the maximum pulsed field

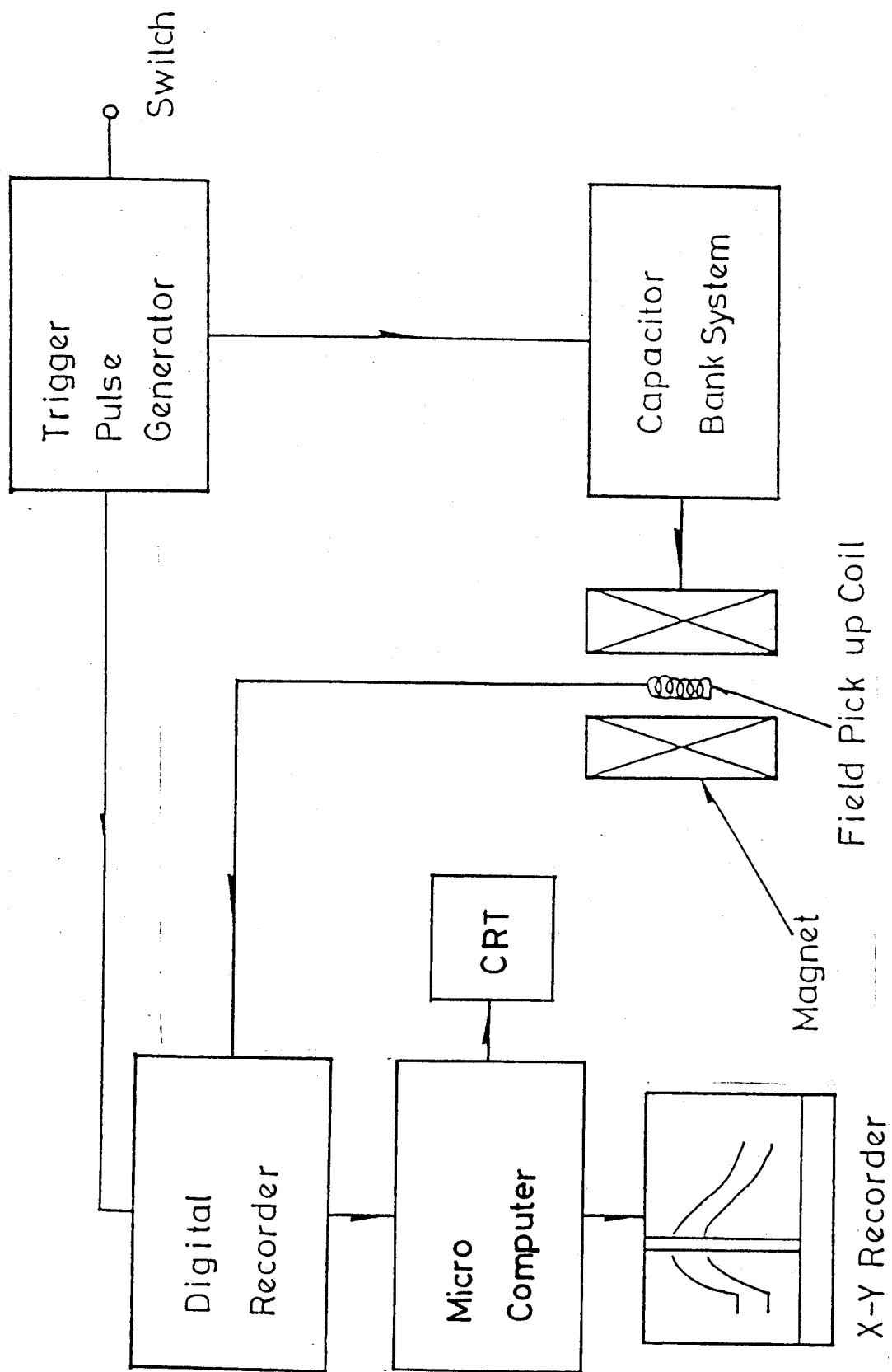


Fig. 19. Block diagram of the field generation and measurement.

170(2LP)18

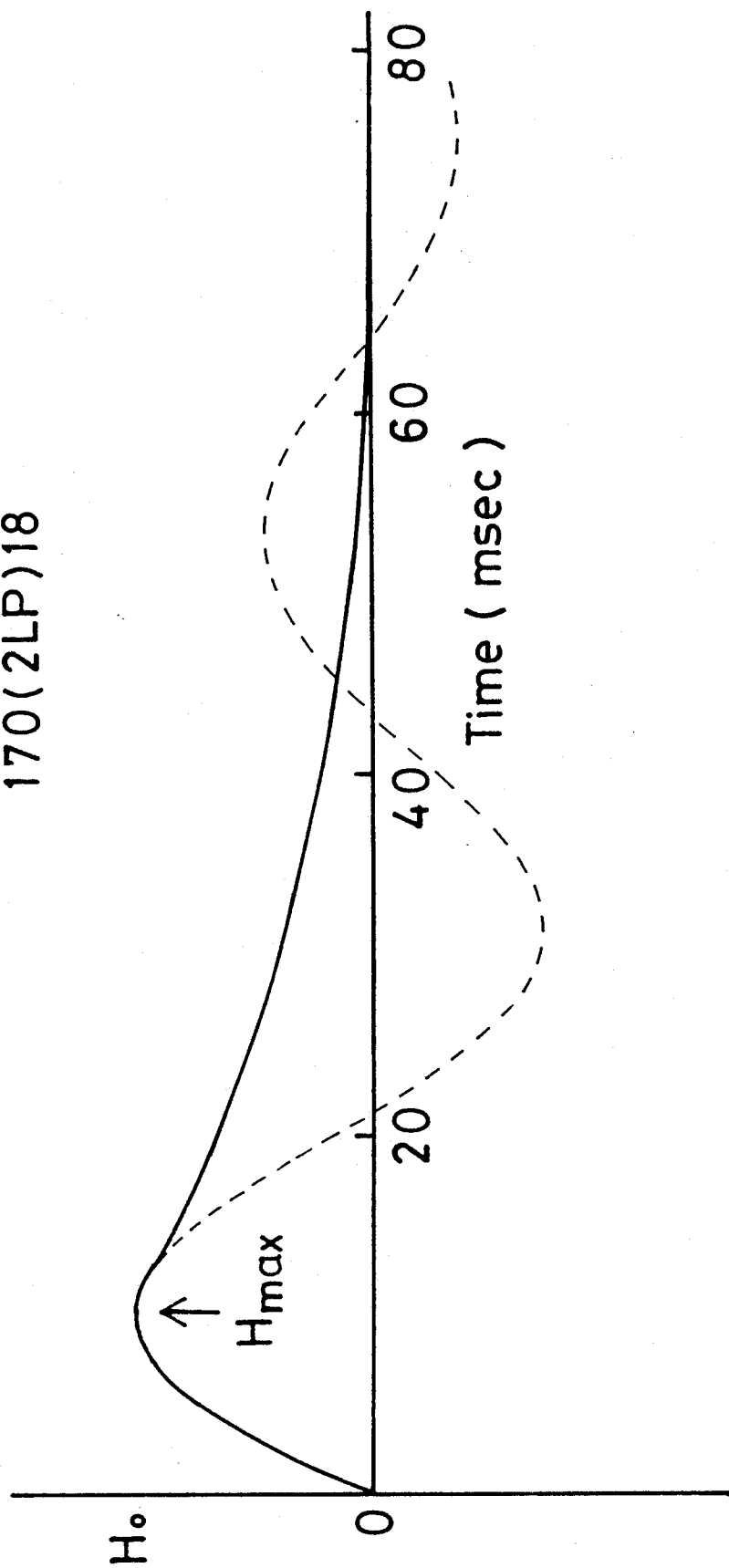


Fig. 20. Magnetic field profile of 170(2LP)18 magnet.

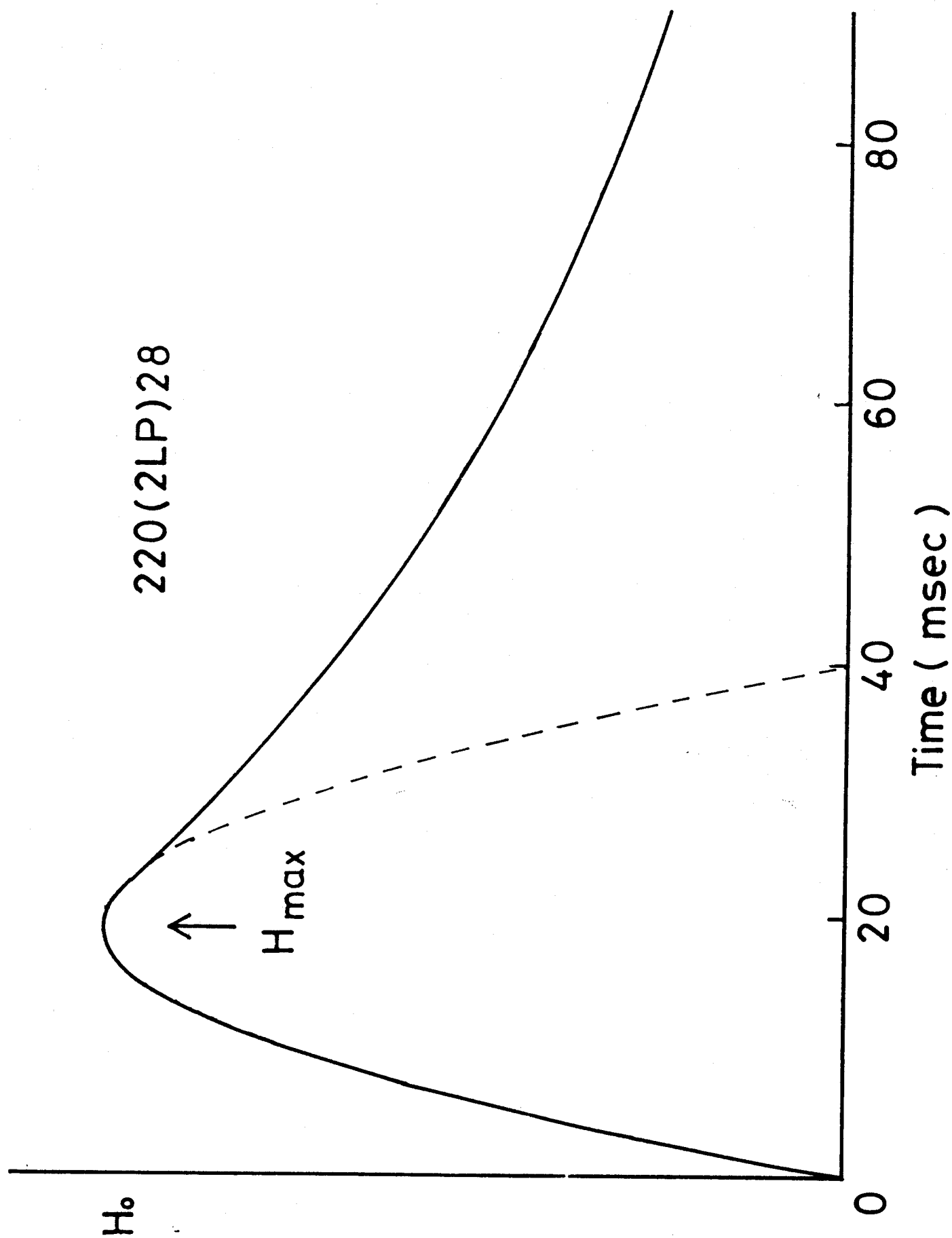


Fig. 21. Magnetic field profile of 220(2LP)28 magnet.

Table IV Characteristics of Long-Pulse Magnet

	$\Delta t(\text{msec})$ [with crowber.]	L (mH)	R (m Ω)	H_{max} (kOe)	E (kJ)
170(2LP)18	20 [60]	18	227	410	500
220(2LP)28	40 [120]	64	180	260	500

generation with 500 kJ energy. This means that the coil windings were not seriously deformed after these shots. The field intensities produced by the two long-pulse magnets are shown in Fig. 22 as a function of the charging voltage. The magnetic field increases linearly with voltage while the short-pulse magnet shows slight deviation from the linear dependence.¹³⁾ The difference comes from the fact that the current path of the former is strictly determined by the thin wire but the current in the latter coil flows in the plate-like wire and the current distribution is modified during the field generation.

To use the magnet for physical experiments, a field homogeneity at the center of the magnet is very important. Inhomogeneity, for example, induces the broadening of ESR line or the broadening of the phase boundary at the critical field. The measured field distribution of the magnet 170(2LP)18 is shown by curve A in Fig.23 with the cut view of the magnet. Curves B and C show the contribution of the first- and second- layer coils, respectively. The formula for accurate calculation of magnetic field distribution on the solenoid axis is well known and is given by

$$H_z = \frac{NI}{4l(b-a)} \left\{ (l+z) \ln \frac{b+\sqrt{b^2+(l+z)^2}}{a+\sqrt{a^2+(l+z)^2}} + (l-z) \ln \frac{b+\sqrt{b^2+(l-z)^2}}{a+\sqrt{a^2+(l-z)^2}} \right\} \quad (5.1)$$

The calculated curve is also shown by a dotted line in Fig. 23. It shows the good agreement with the experiment. The inhomogeneity is less than 0.3 % in a sphere with diameter of 12 mm at the center of the magnet. This volume is eight times

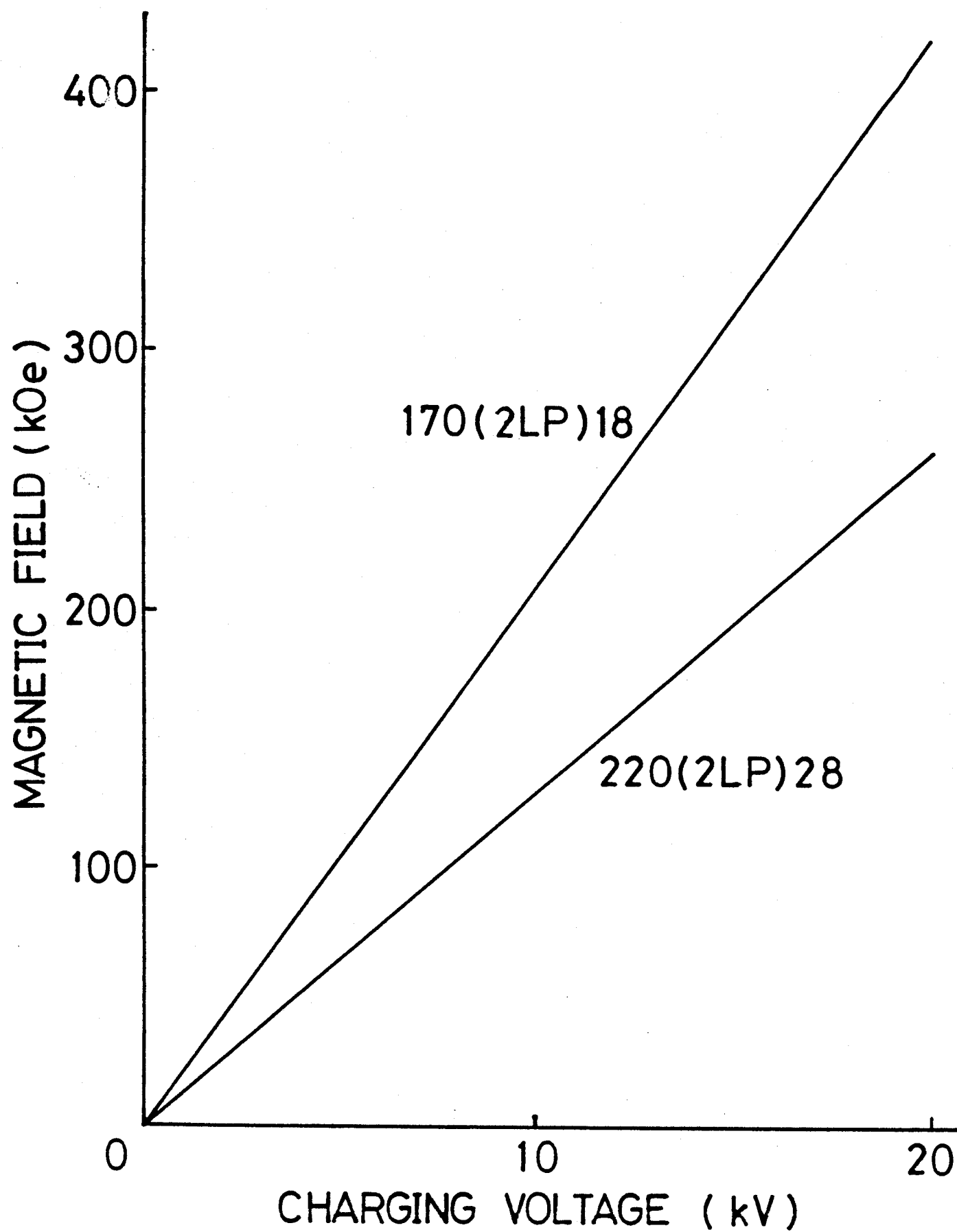


Fig. 22. Magnetic Field vs Capacitor voltage.

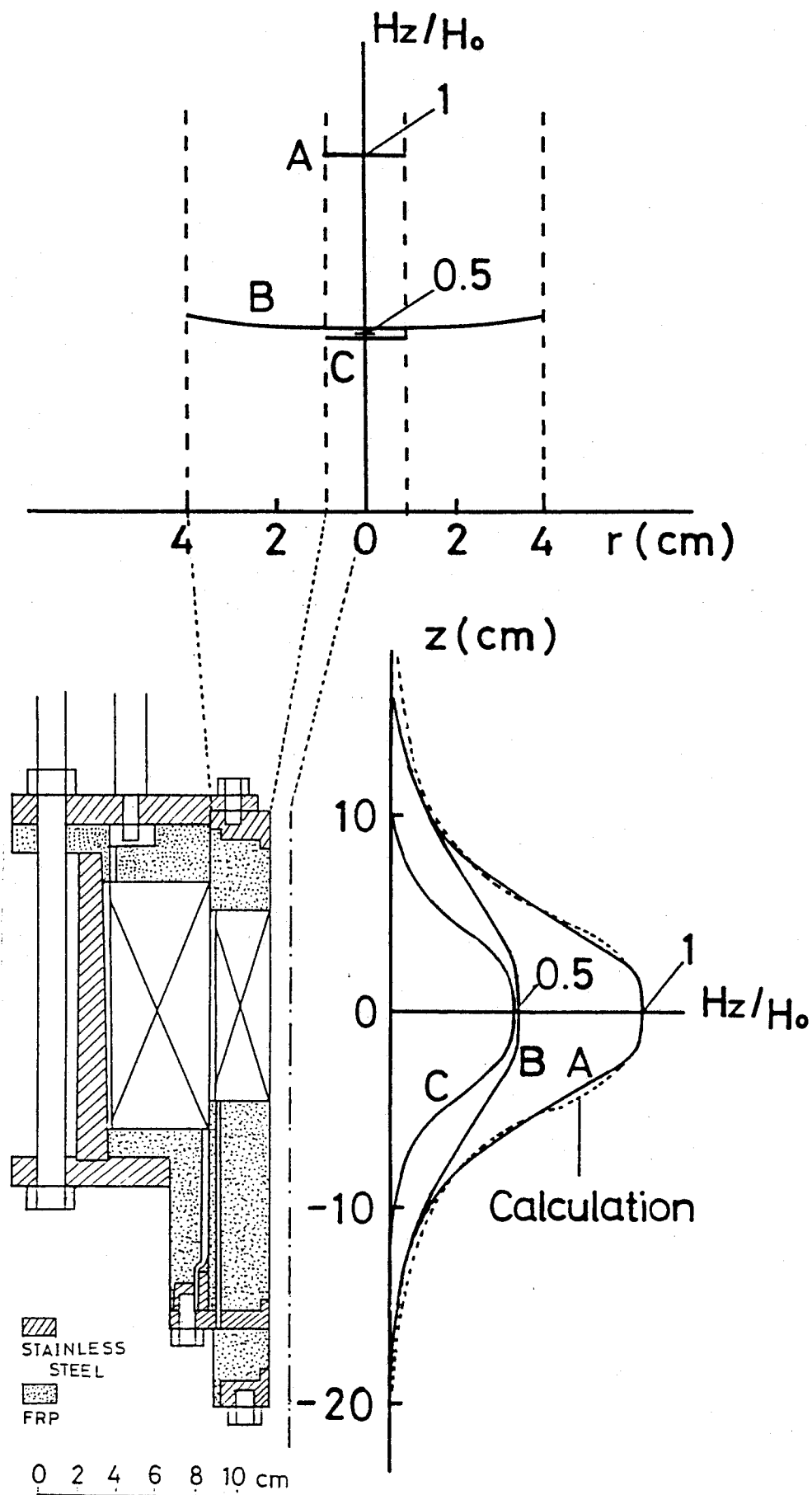


Fig. 23. Magnetic field distribution of 170(2LP)18 magnet.

larger than that of short-pulse magnet.¹³⁾

Figure 24 shows the time variation of the coil temperature after one shot of 400 kOe with the 170(2LP)18 magnet, which is obtained by the variation of coil resistance. Just after the shot, the temperature increases up to about 50 K and then decreases gradually with the time constant of 20 minutes. Waiting time for the next 400 kOe shot should be longer than 40 minutes to keep the temperature increase as low as possible and to avoid vibration of samples due to boiling of liquid nitrogen in the magnet bore. Evaporation amount of liquid nitrogen after each shot is given in Fig. 25 as a function of magnetic field intensity. After a 400 kOe shot, about 3 l of liquid nitrogen should be added for cooling of the magnet.

An interesting test of the pulsed field effect on the copper pipes is shown in Fig. 26. The metal tube is compressed by the force acting on the field-induced electrical current in the tube. The effect due to the short-pulse magnet is seen in the lower photograph. Copper tubes are crushed seriously while the upper pipes exposed to the long-pulsed magnet field are not deformed. Therefore, it becomes possible to do, for example, the ESR experiment with microwave cavity in the pulsed high magnetic fields. The microwave ESR experiment in the long-pulse magnet is now extending at the Research Center for Extreme Materials.

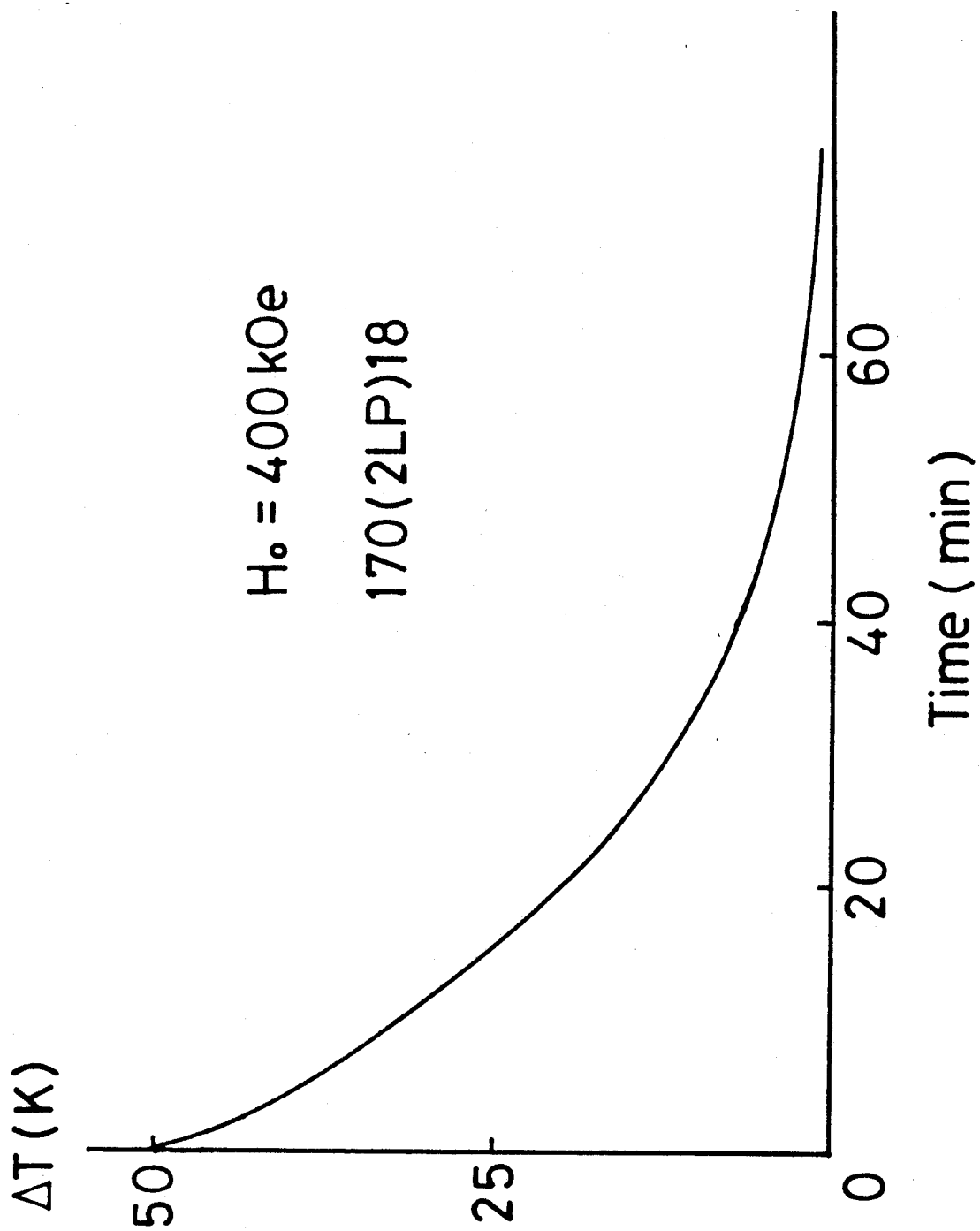


Fig. 24. Cooling characteristics after pulse field generation.

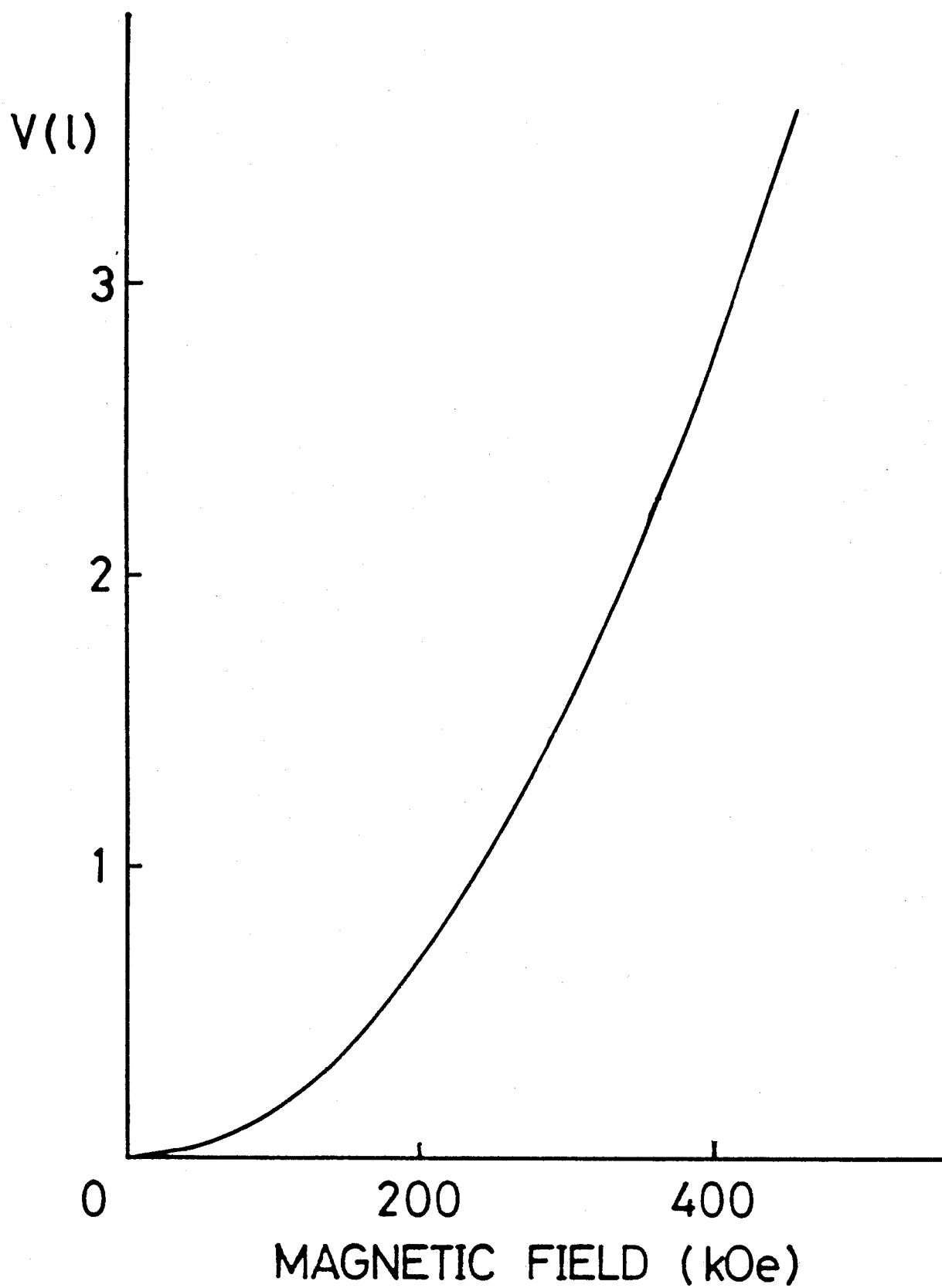


Fig. 25. Evaporation amount of liquid nitrogen by one shot.

Long-Pulse →

Short-Pulse →

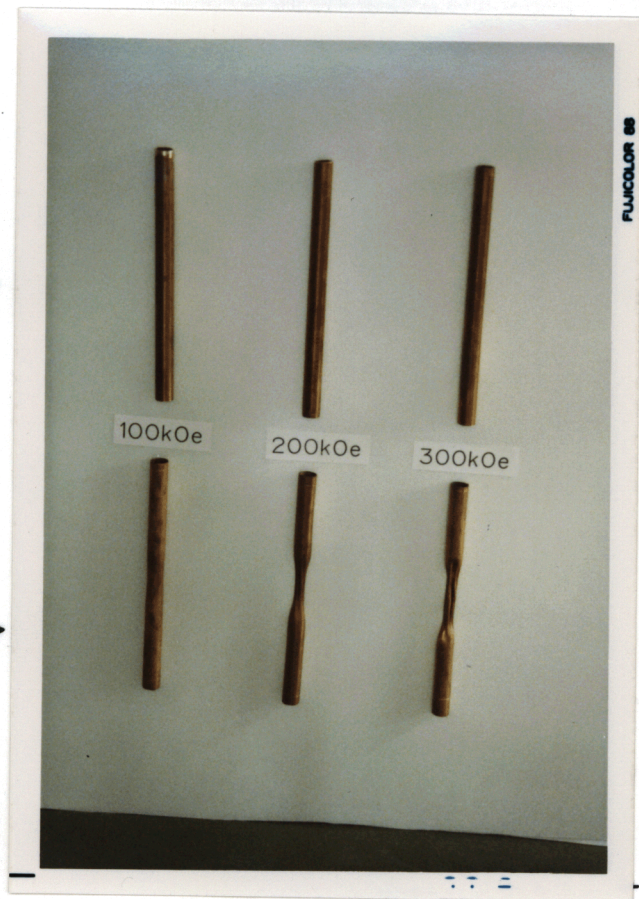


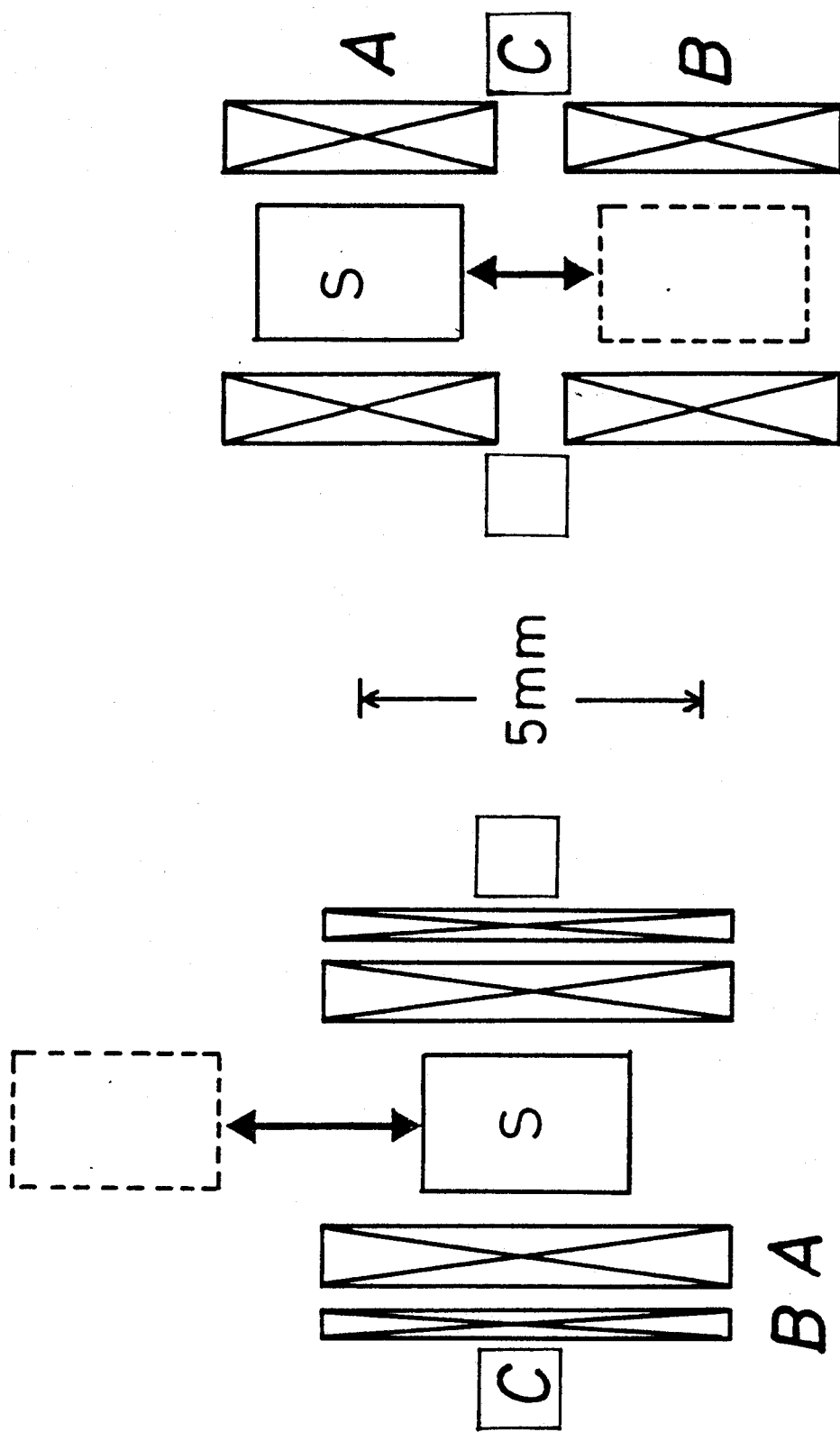
Fig. 26. Compression test of Cu-tubes by the long- and short-pulse magnets.

§ 6 HIGH FIELD MAGNETIZATION OF CONDUCTIVE MATERIALS

The magnetization measurement is done using a balanced pick-up coil. The technically important point is how to compensate background flux change due to a transient field, which is 10^4 - 10^5 times larger than the flux change due to the magnetization of the specimen. This is usually attained by using three coils A, B and C. The coil A picks up the magnetic flux change of the specimen while the coil B is wound in the opposite direction to A in order to compensate the background flux change. One turn coil C makes it possible to adjust further fine compensation by using a bridge balance technique. The sensitivity of the measurement strongly depends on the arrangement of these coils.

Figure 27 (a) is the coaxial standard pick-up coil which has been used in our laboratory with the short-pulse magnet.¹⁵⁾ The coil B (50 turns) is coaxially and oppositely wound on A (100 turns). The cross section of B is twice as large as that of A so as to make the net flux in A equal to that in B. The magnetization measurement is done with a sample in the pick-up coil at first and then without a sample. The magnetization M is obtained by subtracting the second signal $B_0(t)$ from the first one $[dM(t)/dt + B_0(t)]$. The fine adjustment coil C is wound on B.

The signal voltage induced in a pick-up coil is proportional to the flux change $d\phi/dt$ and number of turns N . $d\phi/dt$ in the long-pulse magnetic field is about 100 times smaller than that in the short-pulse magnetic field. Accordingly, increase in N or use of larger pick-up coil should be considered to keep the same sensitivity. Considering an enough space for high uniformity



(a) Co-axial Type (b) Separate Type

Fig. 27. Pick-up coils.

field region, the separate type pick-up coil shown in Fig.27(b) is adopted. The coil A (200 turns) and the coil B (200 turns) are wound oppositely to cancel out the external flux change and the fine adjustment coil C (one turn) is wound between A and B. The coil length is about twice of the coaxial type pick-up coil but the whole coils still in the homogeneous region. The magnetization measurement is done with a samples in A coil at first and then next in B coil. The magnetization M is obtained by subtracting the second signal $[dM(t)/dt - B_0(t)]$ from the first one $[dM(t)/dt + B_0(t)]$.

Comparison of the coaxial and separate type pick-up coils are considered in the following way: high sensitivity is obtained in the separate type but the background canceling is better in the coaxial type. Accordingly, the former is effective for the long-pulse magnet where $d\phi/dt$ is weak but high uniformity of the magnetic field is obtained in a wide space. On the other hand, the latter one is useful in the short-pulse magnet where the high uniformity is limited in a narrow but high $d\phi/dt$ space.

Figure 28 shows the block diagram of the magnetization measurement. Sample position in the pick-up coil is controlled by using a small DC motor. The dewar and cryostat system is similar to that of the two-layer short-pulse magnets.

Magnetizations of two conductive single crystals, the Ising spin system PrCo_2Si_2 and a weakly ferromagnetic CeRh_3B_2 , are measured. PrCo_2Si_2 is an Ising antiferromagnet with Néel temperature T_N of 30 K. Ising spins make antiferromagnetic chains along the c -axis. Below T_N , two incommensurate structures $k=(0,0,0.926)$ and $(0,0,0.777)$ $[2\pi/c]$ appear for $9\text{ K} < T < 17\text{ K}$

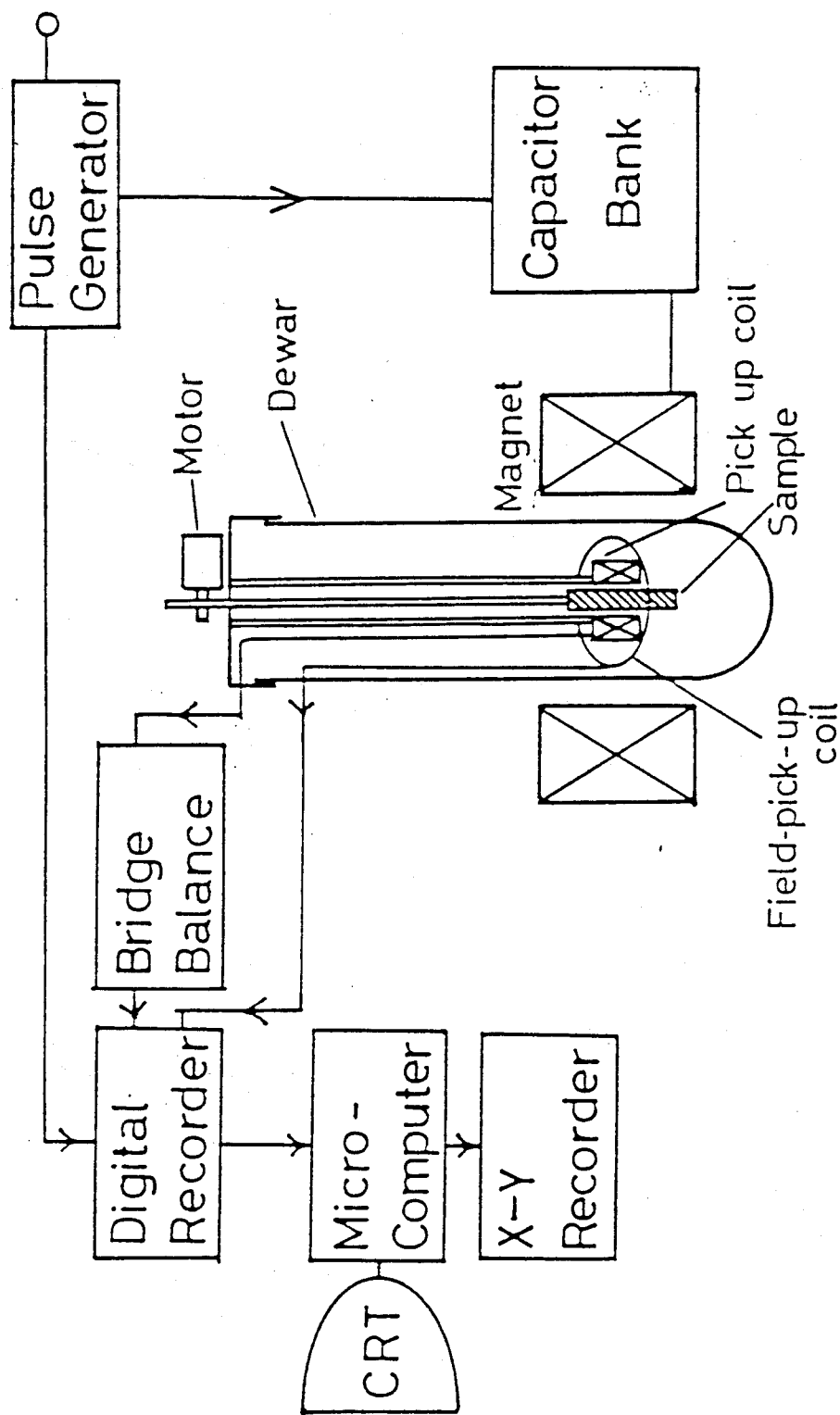


Fig. 28. Block diagram of magnetization measurement.

and $17\text{ K} < T < 30\text{ K}$, respectively. The simple antiferromagnetic structure is stable below 9 K .¹⁷⁾ Two metamagnetic step magnetizations are found by Shigeoka et al. at 4.2 K , under magnetic field up to 60 kOe . Moment at 60 kOe is about $0.6\ \mu_{\text{B}}/\text{Pr}$ and this value is smaller than full moment of Pr^{3+} of $3.2\ \mu_{\text{B}}$. It has small resistivity of $5\ \mu\Omega\text{cm}$ at 4.2 K and a single crystal grown by Shigeoka et al. has the thickness of about 2 mm . Figure 29 shows the results of magnetization measurements using the long- and short-pulse magnets. The dotted curve is obtained by the short-pulse magnetic field. It shows very large hysteresis due to the eddy current and one can not see any clear steps on the curve. However, the solid curve, which is measured under the long-pulse magnetic field, shows clear five metamagnetic transitions and gives the saturation moment of $3.2\ \mu_{\text{B}}/\text{Pr}$ above 120 kOe .

Another example is obtained in CeRh_3B_2 . This is a ferromagnet with Curie temperature T_{c} of 120 K and spontaneous magnetization of $0.38\ \mu_{\text{B}}$.¹⁸⁾ The crystal structure has a uniaxial anisotropy and magnetic moment is in the c-plane. The electrical resistivity is about $3\ \mu\Omega\text{cm}$. The interesting point is that the small spontaneous magnetization and large high-field susceptibility has been expected. The high field magnetization of the powder sample is observed up to 600 kOe by using the short-pulse magnet and large high field susceptibility is found. The magnetization measurement of the single crystal is carried out up to 400 kOe using the long-pulse magnet. The obtained magnetization curves are shown in Fig.30. It is found that the

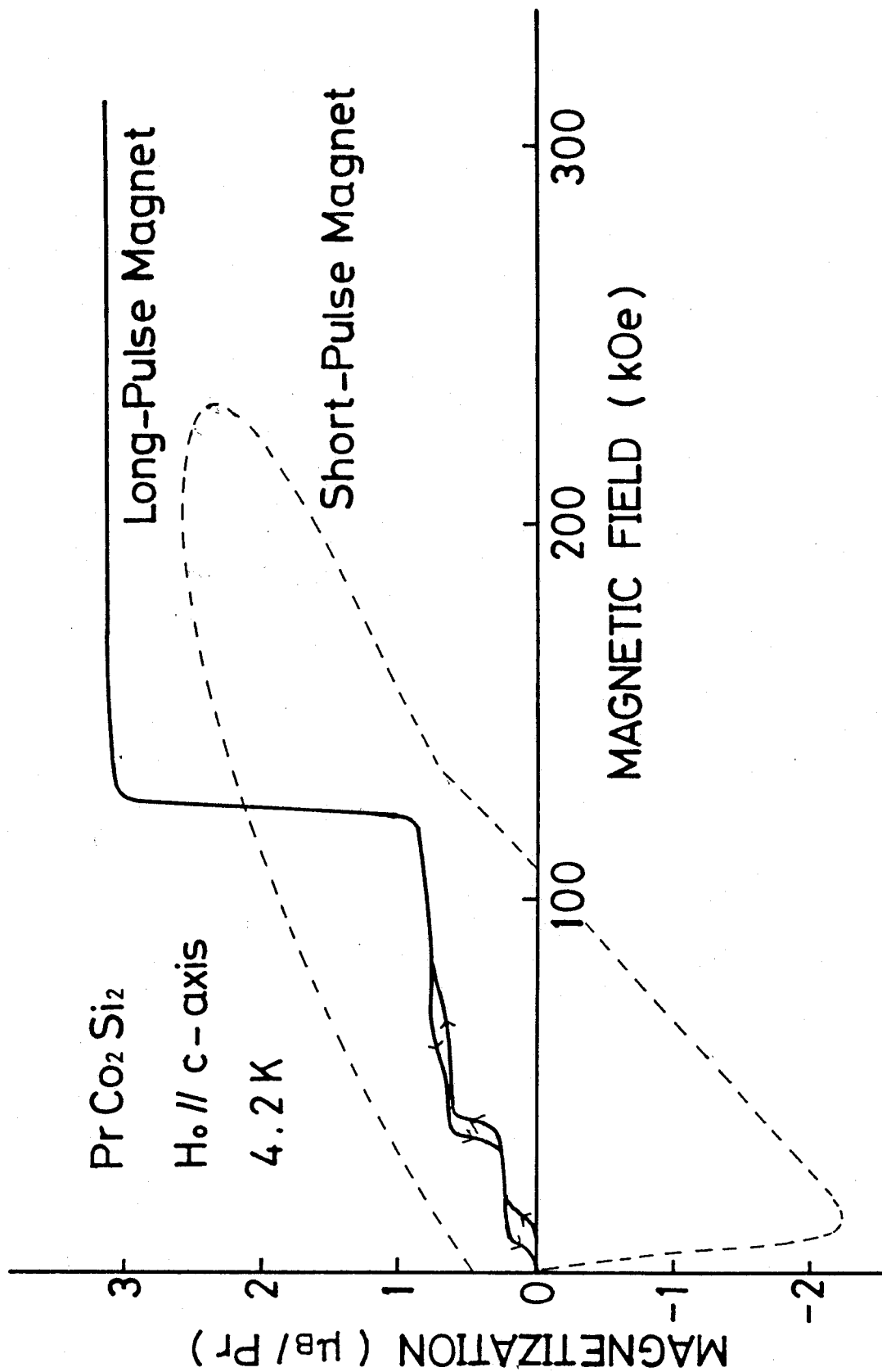


Fig. 29. Magnetization of PrCo_2Si_2 .

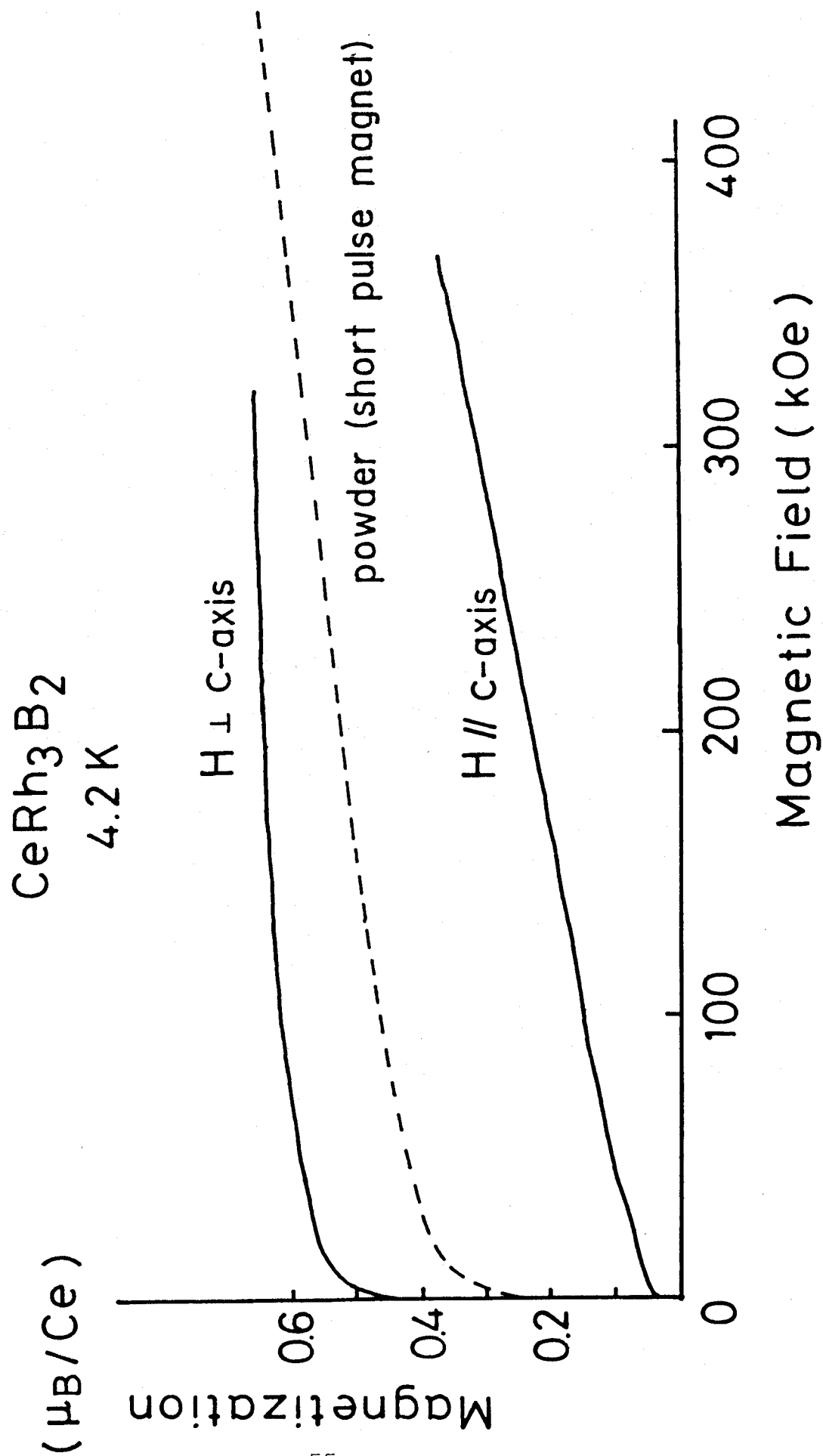
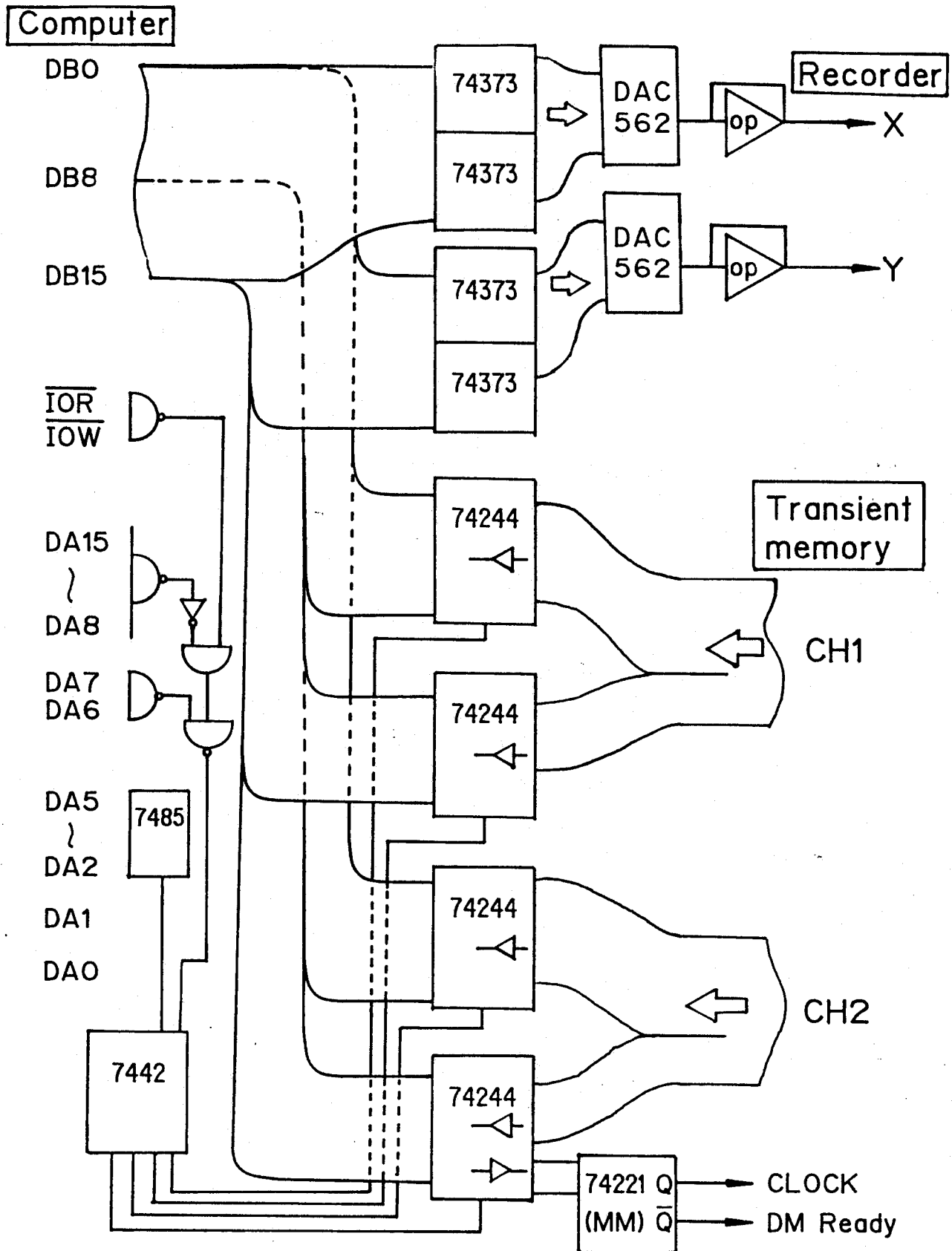


Fig. 30. Magnetization of CeRh_3B_2 .

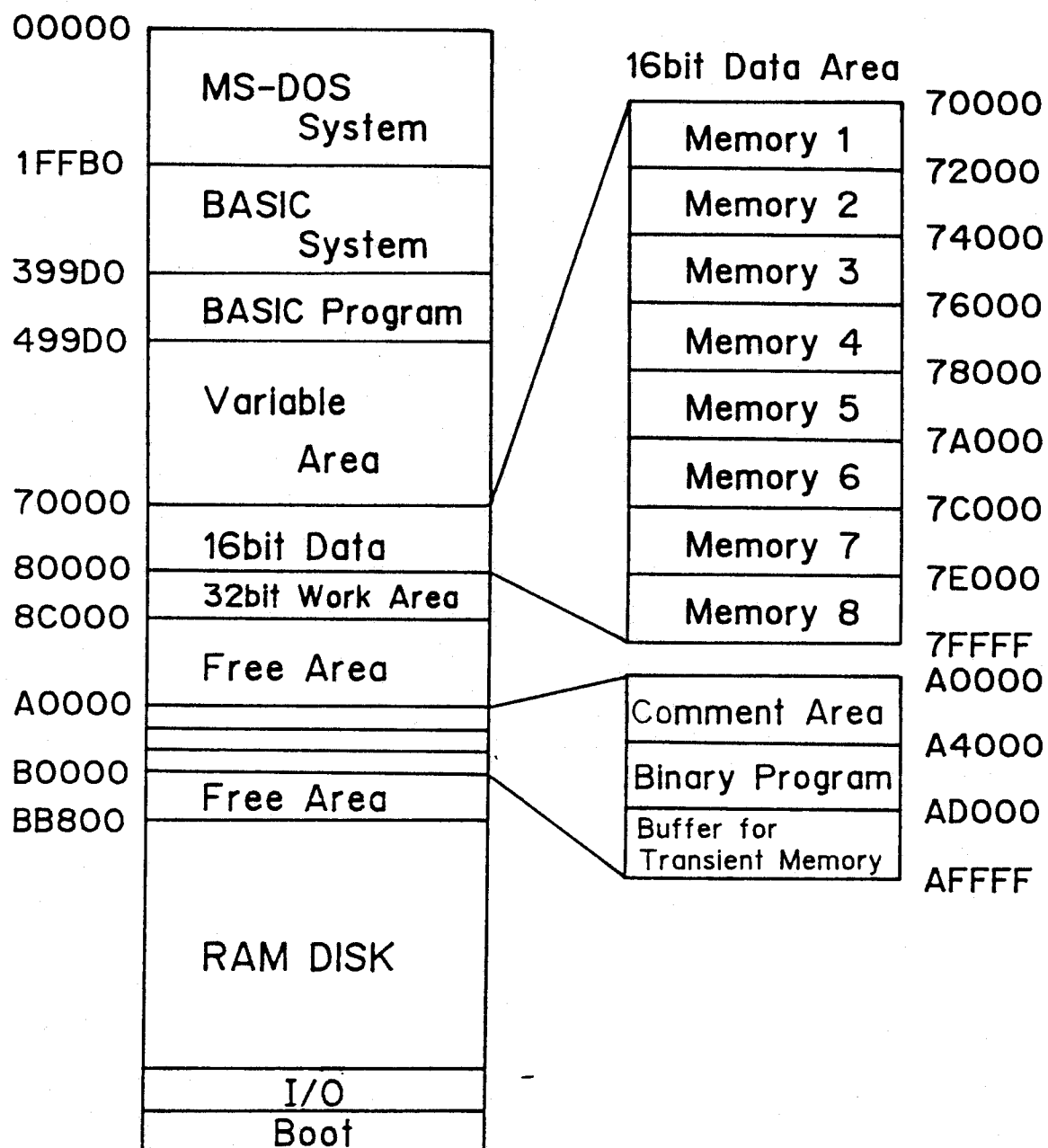
main part of the high field susceptibility seen in the powder sample is due to the increase in the magnetization perpendicular to the c-plane.



Functions of Data Processing

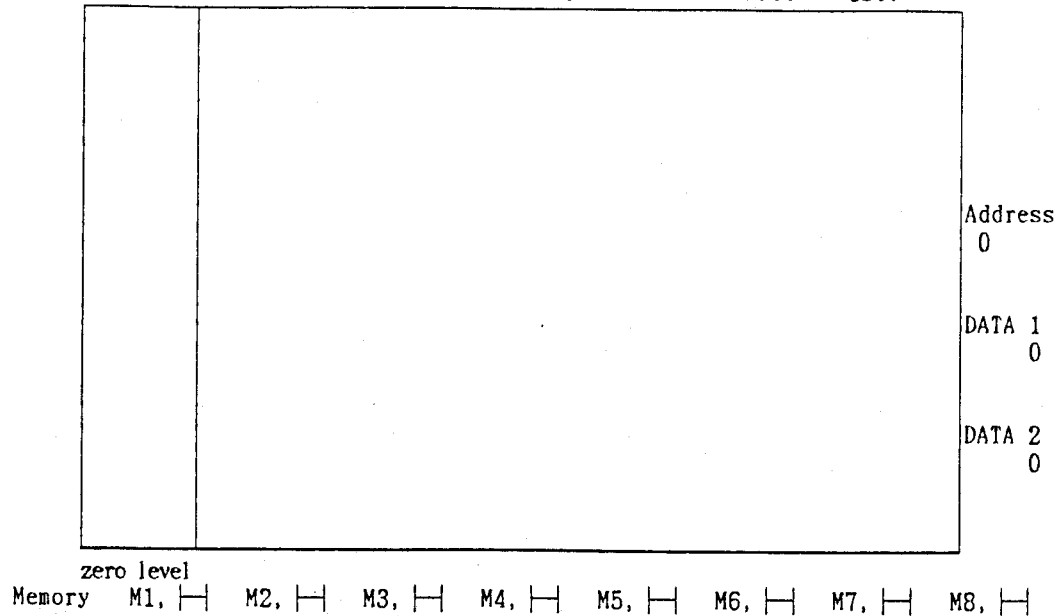
1. Data + Data
2. Data - Data
3. Data \times Data
4. Data \div Data
5. Data + const.
6. Data - const.
7. Data \times const.
8. Data \div const.
9. Integrate
10. zero level shift
11. word shift
12. Averaging
13. off set correction
14. Display (X-Y,Y-T)
15. write to X-Y recorder
16. Memory block transfer
17. Data set

Memory Map



File name = No file < BASE MODE > Diskette No.= MAG11

DATA 1 (4000) 0%
 DATA 2 (4000) 0% Time rate 0sec



File name = No File < BASE MODE > Diskette No.= MAG11

DATA 3 20mV/FS(4096)
 DATA 4 1.0V/FS(4096) Time rate .00002sec

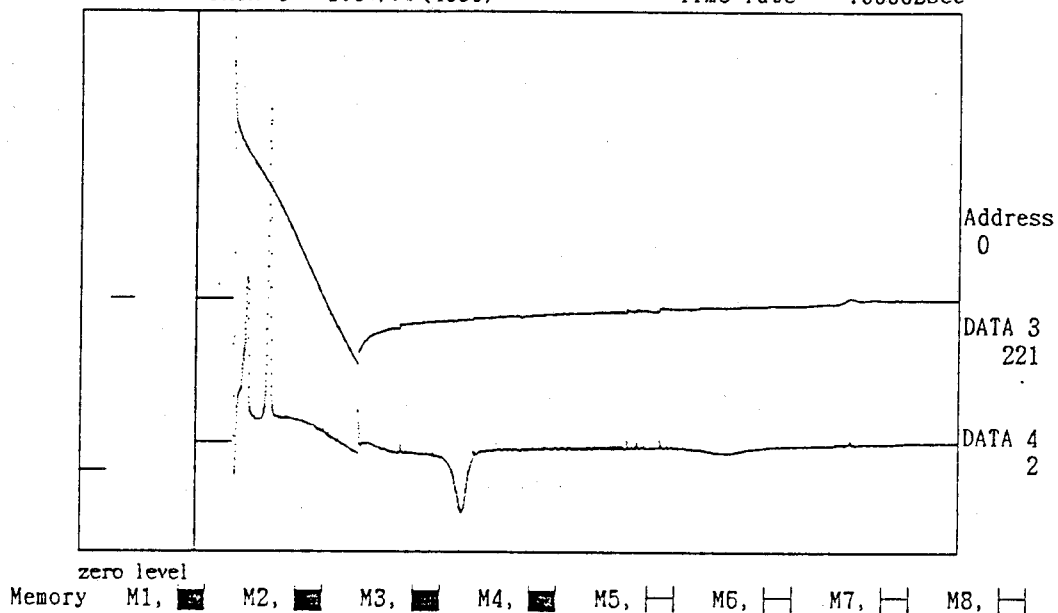


Fig. A-1. Example of the data processing.

(I). Data input to Memory 1 and 2.

They are transferred to Memory 3 and 4,
 respectively.

< Save to disk >

Diskette No.= MAG11

< MEMO >

Sample: Pr Co2 Si2 (single) FROM H.Fujii (hiroshima)

CHARGING VOLTAGE : 3.20 KV Magnet No. : LP

Field pick up coil const. : 0.132 kOe/mV

Temperature : 4.2 K

Range M1: 20mV/FS M2: 1.0V/FS M3: 20mV/FS M4: 1.0V/FS

Date : 88 , 1 , 18

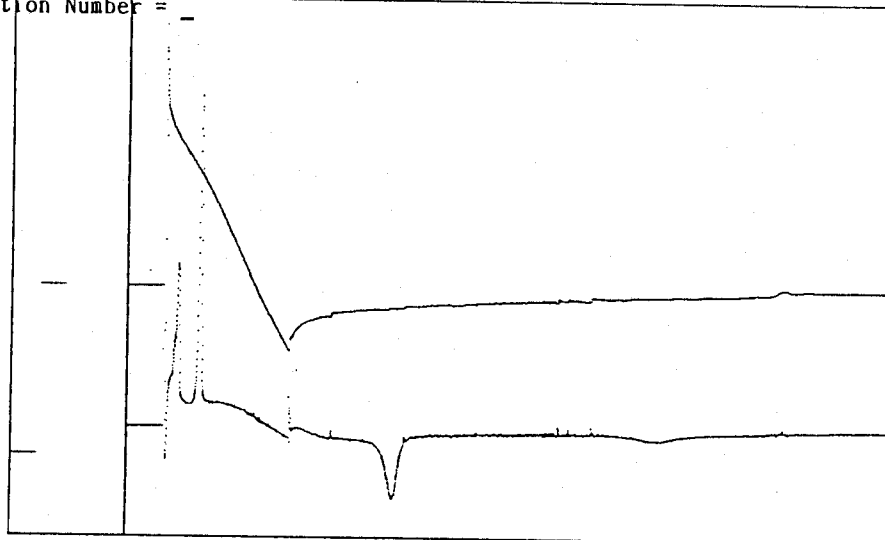
Operator : M.Ono,K.Yonenobu,K.Sugiyama

COMENT

H//C

* MEM +/- Const/ MEM / MEM + MEM * MEM - MEM -- MEM = Recorder
1 Integration 2 Transfer 3 Level Shift 4 Display 5 Average
6 Repair Pulse 7 Data Set 8 Data Shift

Function Number =

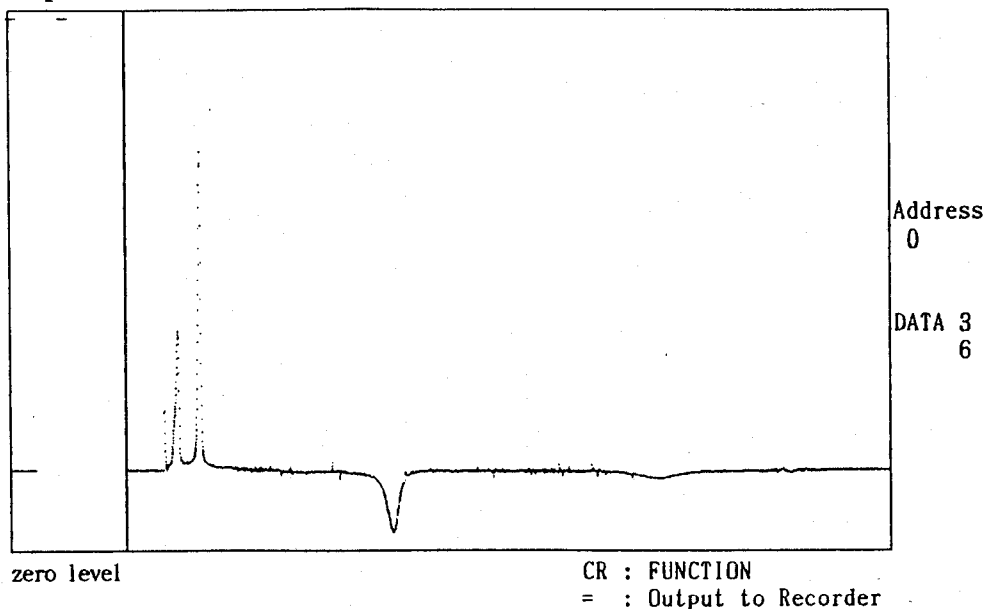


zero level

Fig. A-2. Example of the data processing.

(II) Used parameters and the function mode.

MEM A +- MEM B ==> MEM A
 MEM A = 3
 MEM B = 1
 + or -



Integration of MEM A ==> MEM A
 MEM A = 3

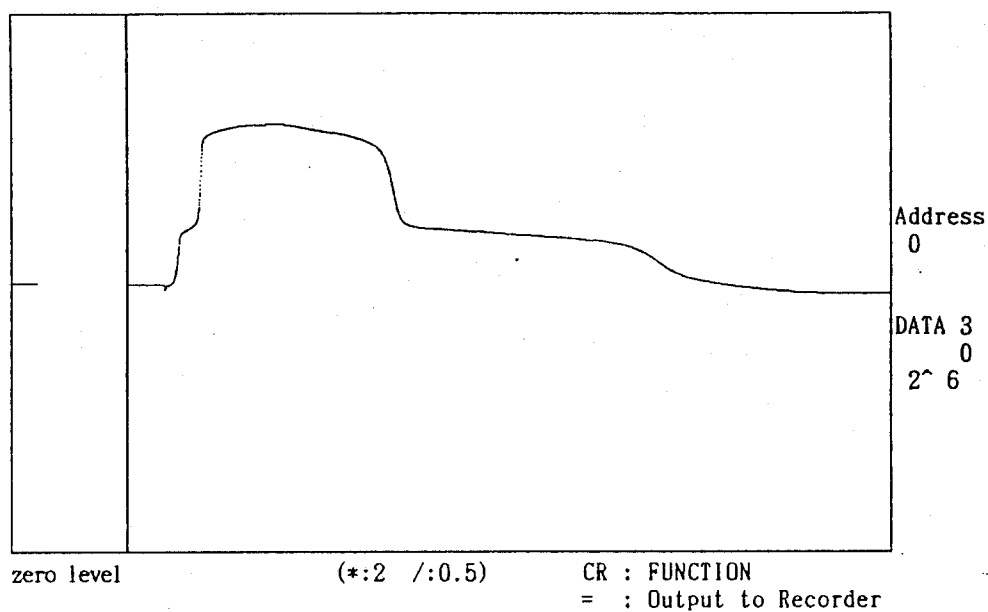


Fig. A-3. Example of the data processing.

(III) Subtractions and integrations of the magnetization signal.

Integration of MEM A ==> MEM A
MEM A = 4

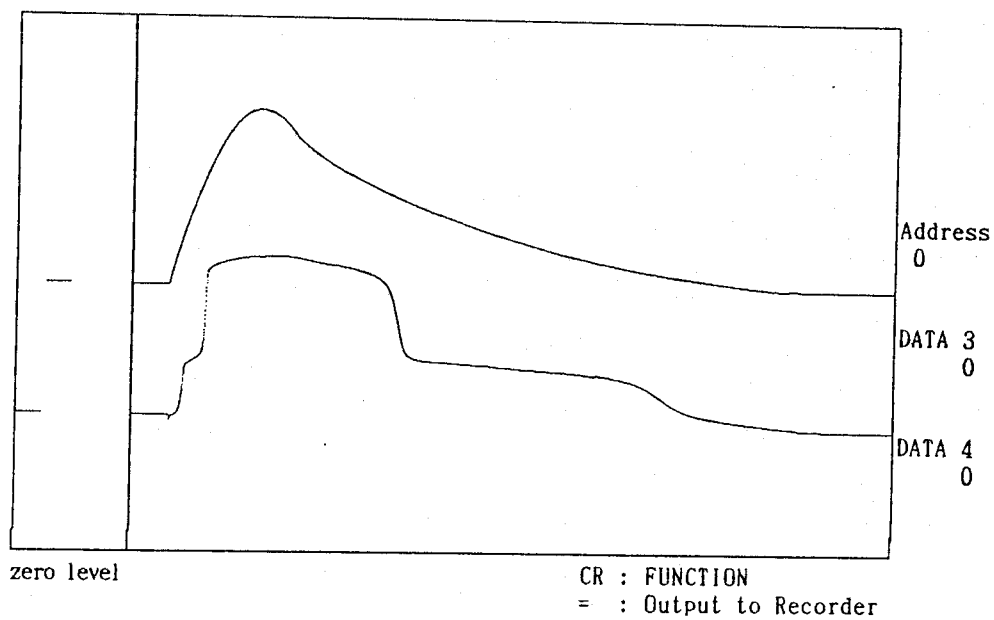
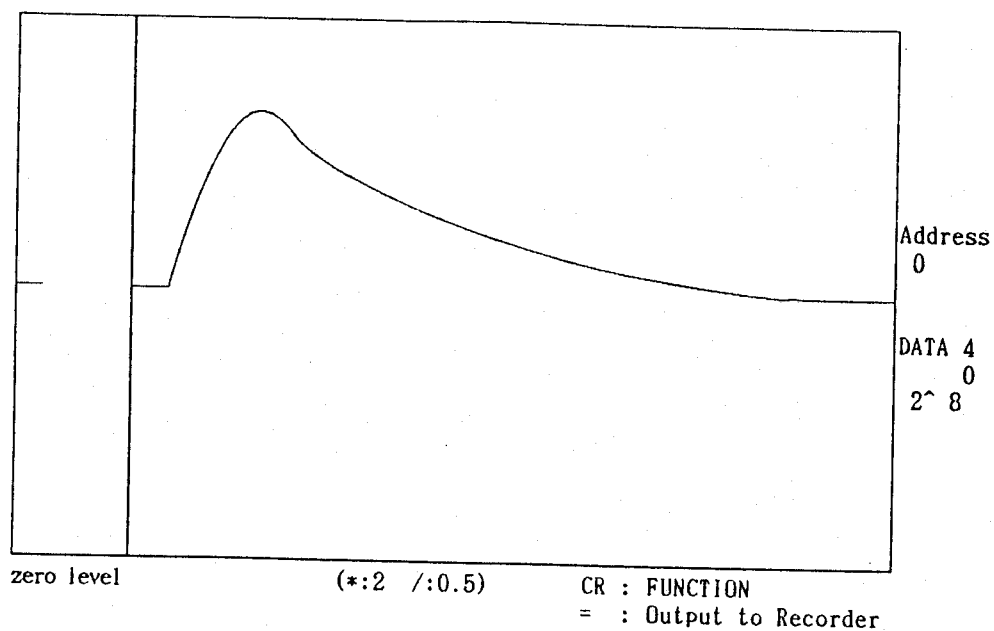


Fig. A-4. Example of the data processing.

(IV) Magnetic field and the corresponding magnetization by the M-t display.

M(H₀) display is given in the text.

REFERENCES

- 1) P. L. Kapitza: Proc. Roy. Soc. A105 (1924) 691.
- 2) T. Wall: J. Inst. Elect. Engrs. 64 (1926) 745.
- 3) F. Bitter: Rev. Sci. Instrum. 10 (1939) 373.
- 4) Y. Muto, Y. Nakagawa, K. Noto, S. Miura, A. Hoshi, K. Watanabe, G. Kido, I. Ichikawa, T. Fujioka, Y. Sato, O. Osaki and H. Takano: Sci. Rep. RITU 33 (1986) 221
- 5) H. Knoepfel: Pulsed High Magnetic fields (North Holland, Amsterdam 1970).
- 6) M. Date: J. Phys. Soc. Jpn. 39 (1975) 892.
- 7) M. Date, M. Motokawa, A. Seki, S. Kuroda, K. Matsui and H. Nakazato: J. Phys. Soc. Jpn. 39 (1975) 898. See also A. Seki: Dr. Thesis (1974) Osaka University.
- 8) M. Date: IEEE Trans. Magnetics, MAG-12 (1976) 1024.
- 9) A. Yamagishi and M. Date: High Field Magnetism, ed. by M. Date (North Holland, Amsterdam 1983) 289.
- 10) T. Kasuya, O. Sakai, T. Takegahara and M. Takeshige: J. Magn. & Magn. Mat. 52 (1982) 1.
- 11) M. K. Wu, J. R. Ashkurn, C. J. Torng, P. H. Hor, R. L. Merg, L. Gao, Z. J. Huang, Y. Q. Wang and C. W. Chu: Phys. Rev. Lett. 58 (1987) 908.
- 12) R. Gersdorf, F. R. de Boer, J. C. Wolfrast, F. A. Muller and L. W. Roeland: High Field Magnetism, ed. M. Date (North Holland, Amsterdam 1983) p.277.
- 13) H. Mollimoto: Dr. Thesis (1980) Osaka University.
- 14) T. Sakakibara: Dr. Thesis (1980) Osaka University.
- 15) H. Mollimoto, M. Motokawa and M. Date: J. Phys. Soc. Jpn 49

- (1980) 108. See also T. Sakakibara, H. Mollmotto, M. Motokawa and M. Date: High Field Magnetism, ed. M. Date (North-Holland, Amsterdam, 1982) p.299.
- 16) Y. Shapira and J. Zak: Phys. Rev. 170 (1968) 503.
- 17) T. Shigeoka, N. Iwata, H. Fujii, T. Okamoto and Y. Hashimoto: J. Magn. & Magn. Mat. 70 (1986) 239.
- 18) K. N. Yang, M. S. Torikachrili, M. B. Maple and H. C. Ku: J. Low. Temp. Phys. 56 (1984) 601.

PART II

HIGH FIELD STUDIES OF
SOME INTERMETALLIC COMPOUNDS

PART II - A -

HIGH FIELD MAGNETIZATION OF GdB_6

ABSTRACT

High field magnetization of GdB_6 is investigated up to 550kOe. The saturation magnetization of $7 \pm 0.5 \mu_B$ is obtained around 490kOe at 1.3K and the system can be regarded as a typical cubic antiferromagnet with the nearest neighbor exchange energy J_0/k of $-0.78 \pm 0.02\text{K}$. Beside the standard antiferromagnetic magnetization, two small anomalous step-magnetizations are found near the saturation field H_c . They are explained by the local spin flip of the disordered Gd located at the B_6 cluster site. Two kinds of the disordered states, Type-I and Type-II, are proposed corresponding to two steps. The disordered Gd spin couples with the surrounding host spins with the antiferromagnetic exchange energy J'/k of -1.2K and -1.3K for Type-I and Type-II, respectively.

§1 INTRODUCTION

Rare-earth hexaborides with a simple cubic CaB_6 type crystal structure¹⁾ have been investigated extensively with special interests in the valence fluctuations and dense Kondo states. For example, CeB_6 is considered to form a typical dense kondo system with the anomalous magnetic structure below 3.1K²⁾ while SmB_6 shows valence fluctuation with a semiconductive band gap at the Fermi level.³⁾

On the other hand, GdB_6 is considered as a simple Heisenberg antiferromagnet of Gd^{3+} ions with the ground state of $^8\text{S}_{7/2}$. The Néel temperature T_N is 16 K and the Curie-Weiss constant Θ is about -60 K.⁴⁾ The magnetic susceptibility,⁴⁾ electrical resistivity,⁵⁾ magnetic torque,⁶⁾ paramagnetic resonance⁷⁾ and specific heat experiments⁸⁾ have been reported. These data support the simple antiferromagnetic model except some anomalies. An anomalous peak of the resistivity⁵⁾ is found around 10K and the peak strongly depends on magnetic field. Moreover, the resistivity above about 130 kOe decreases widely and no explanation has been reported for these phenomena.

The first aim of the present study was to find the corresponding anomalies in the magnetization curve. However, no anomalies were found for these phenomena. On the other hand, two small but anomalous step-magnetizations are observed as is preliminary reported previously.⁹⁾ The present report gives the details of the high field magnetization in GdB_6 with the quantitative analysis of the step-magnetizations.

§ 2 CRYSTAL STRUCTURE AND MAGNETIC PROPERTIES OF GdB_6

The crystal structure of GdB_6 is isomorphous to CaB_6 with the lattice parameter of 4.111 \AA ¹⁾ and it can substantially be regarded as the CsCl type if a B_6 octahedron is replaced by a simple anion. The crystal structure is illustrated in Fig.31. The B_6 octahedron is surrounded by eight nearest neighbor Gd ions which form a simple cubic structure. The crystal is metallic in all temperature regions. The temperature dependence of magnetic susceptibility shows the Curie-Weiss law above 70 K with spin of $7/2$ and $g=2$.^{4),7)} Below 70 K, the magnetic susceptibility deviates from the Curie-Weiss law and the Schottky type anomaly of specific heat is observed around 30 K.⁸⁾ T_N of 16 K is determined by the magnetic susceptibility, electrical resistivity and specific heat measurements. It is noted that the ratio of Θ/T_N is about -4 which is considerably large compared to that of usual antiferromagnets. This fact will be discussed later.

Since GdB_6 contains boron atoms which absorb neutron, neutron scattering experiment is difficult and no datum has been reported. Three equivalent magnetic domains with collinear antiferromagnetic spins along the $\langle 100 \rangle$ axes are inferred by torque experiment at low temperatures.⁶⁾ The magnetic domains can easily be modified by applying a magnetic field up to 6.5 kOe along the spin axes. This means that a very small magnetic anisotropy exists in the crystal. As will be seen in Section 4, the antiferromagnetic spin structure of the G-type as in CaMnO_3 ¹⁰⁾ is proposed in the present paper.

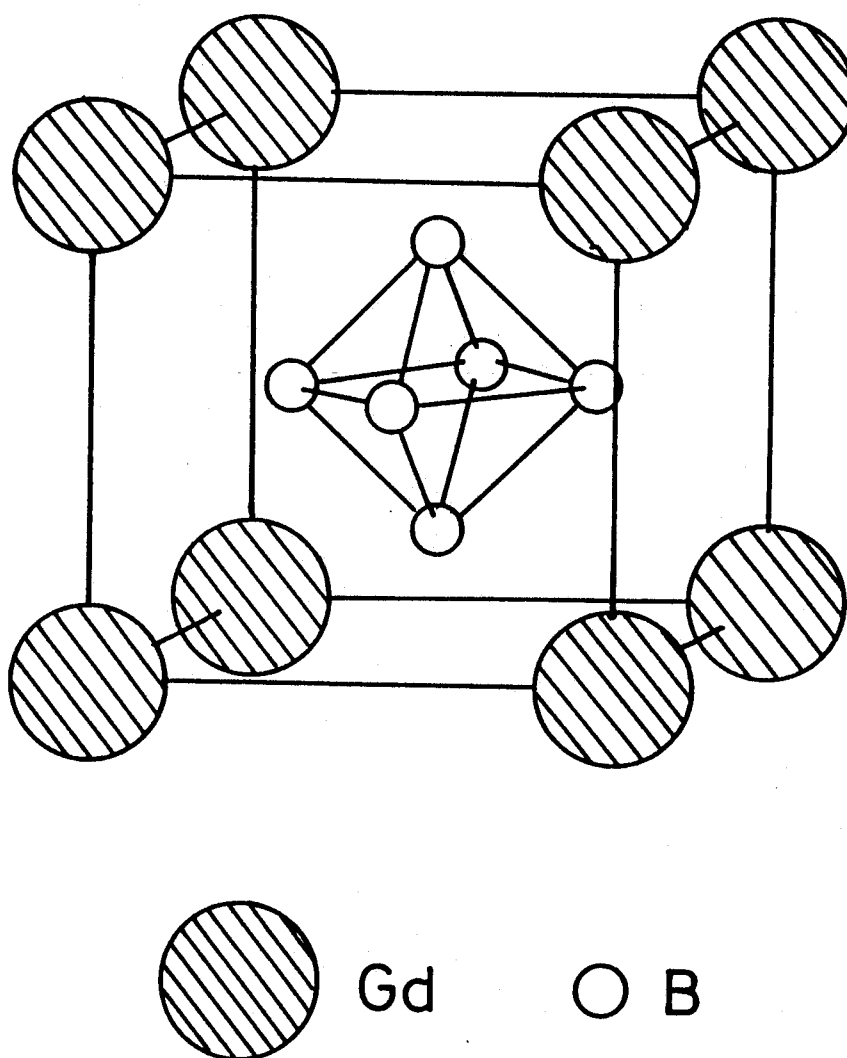


Fig.31 Crystal structure of GdB_6 . B_6 octahedron is located at the center of the cube.

§ 3 EXPERIMENTAL PROCEDURES AND THE RESULTS

A good single crystal with the residual electrical resistance of about $3\mu\Omega\text{cm}$ was kindly supplied the Kasuya group, Tohoku University. They obtained the sample by floating zone method under pressurized high-purity argon gas.⁵⁾ For the pulsed field magnetization measurement, however, the conductivity is too high and the eddy current effect is inevitable if a single crystal were used. Therefore, the crystal is grinded to have a powder sample of about 180 mgr and it is capsuled with ethyl alcohol to prevent the eddy current. The capsule has 2.4 mm in diameter with 1.4 cm in length.

The high field magnetization measurements were done at High Magnetic Field Laboratory, Osaka University.¹¹⁾ Two types of the magnets 150(1L)60 and 150(2L)20 are used with the D-2 capacitor bank ($3600\mu\text{F}$, 26.6 kV) of 1.25 MJ. The pulse width of these magnets is 0.4 msec. The former one is the large bore magnet with the maximum magnetic field of 500 kOe in a diameter of 60 mm. It is possible to regulate the sample temperature with the accuracy of $\pm 0.5\text{ K}$ by the standard automatic control unit¹²⁾. The latter magnet 150(2L)20 is the two-layer magnet which can produce the magnetic field up to 700 kOe in a diameter of 20 mm. The automatic temperature control unit can not be used in this case, because the inner bore of the magnet is too small. Therefore, the measurements are carried out by catching the suitable temperature under a natural temperature increase in the cryostat. The temperature accuracy is about $\pm 1\text{ K}$.

The magnetization measurements are carried out with the

standard pick-up-coil system. The details are shown elsewhere.¹³⁾

Figure 32 shows the block diagram of the magnetization measurement system. The obtained datum is stored in the digital recorder (8 bit, 1024 words, Iwatsu DM-901) and processed in the micro-computer. The output signal from the bridge balance circuit is proportional to dM/dt but still contains residual back-ground flux noise. It is reduced by subtracting the datum without specimen and the magnetization curves are obtained by a digital integration of dM/dt in the micro-computer. The external magnetic field H_0 is picked up by a single loop pick-up-coil and the output signal is integrated by a high speed operational amplifier.

The magnetization curve at 1.3 K linearly increases with increasing external magnetic field H_0 and saturates around the critical magnetic field H_c of 490 ± 10 kOe as is shown in Fig.33. The saturation magnetization is $7.0 \pm 0.5 \mu_B$ in good agreement with the moment of the ground state of Gd^{3+} . The magnetization curve at H_c broadens as temperature increases. The observed linear magnetization below about 400 kOe gives the magnetic susceptibility χ of 3.6×10^{-4} emu/g which shows a good agreement with the static datum of 3.5×10^{-4} emu/g.⁴⁾

The detailed feature of the magnetization curve is found by looking at the dM/dH_0 curve, as is illustrated in Fig.34. At 1.3 K, dM/dH_0 is nearly constant up to H_c reflecting a linear magnetization as is shown in Fig.33. Near H_c , however, anomalous peaks in the dM/dH_0 curve are found at 445 and 490 kOe. These

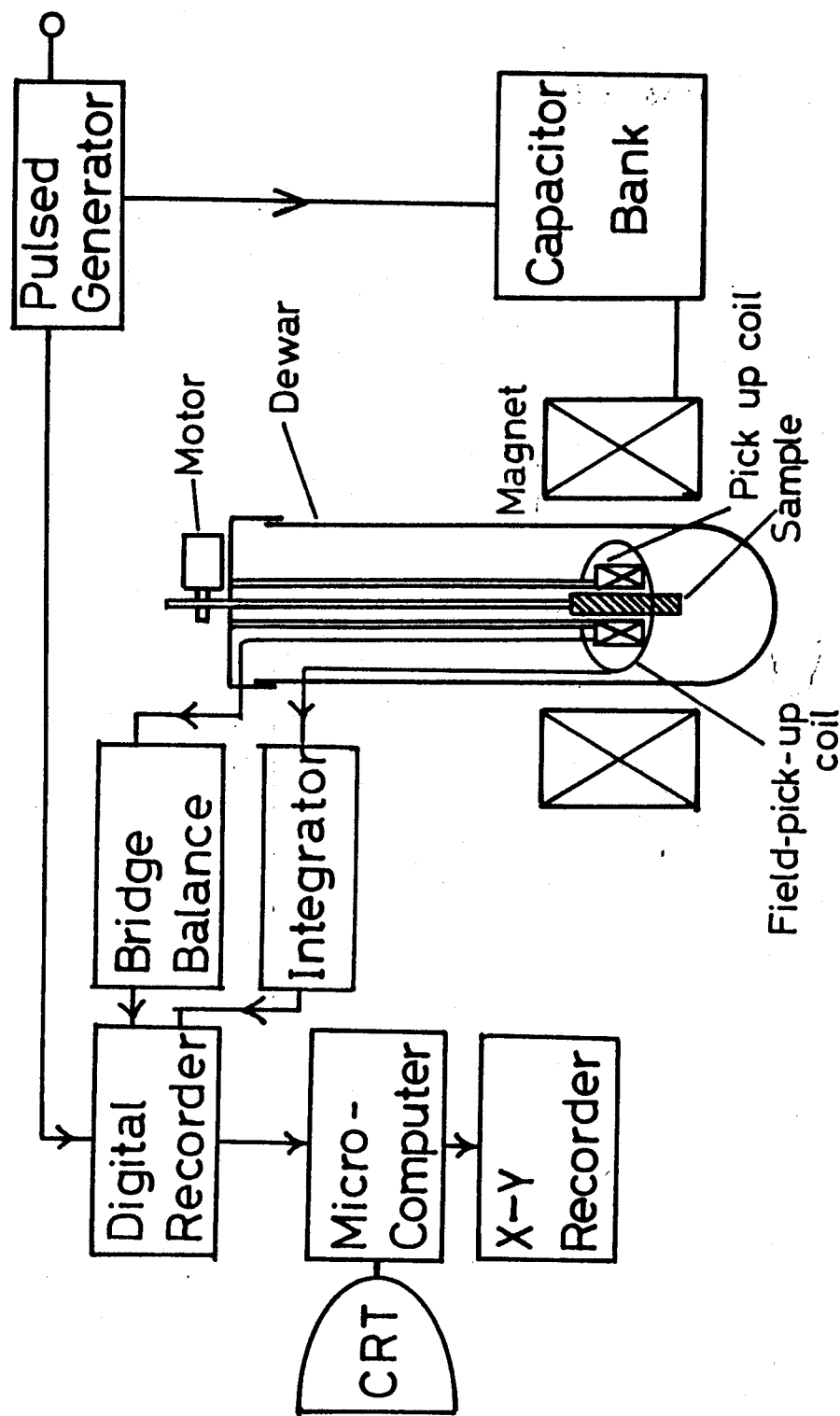


Fig.32 Block diagram of the experimental system used for pulsed magnetization measurement.

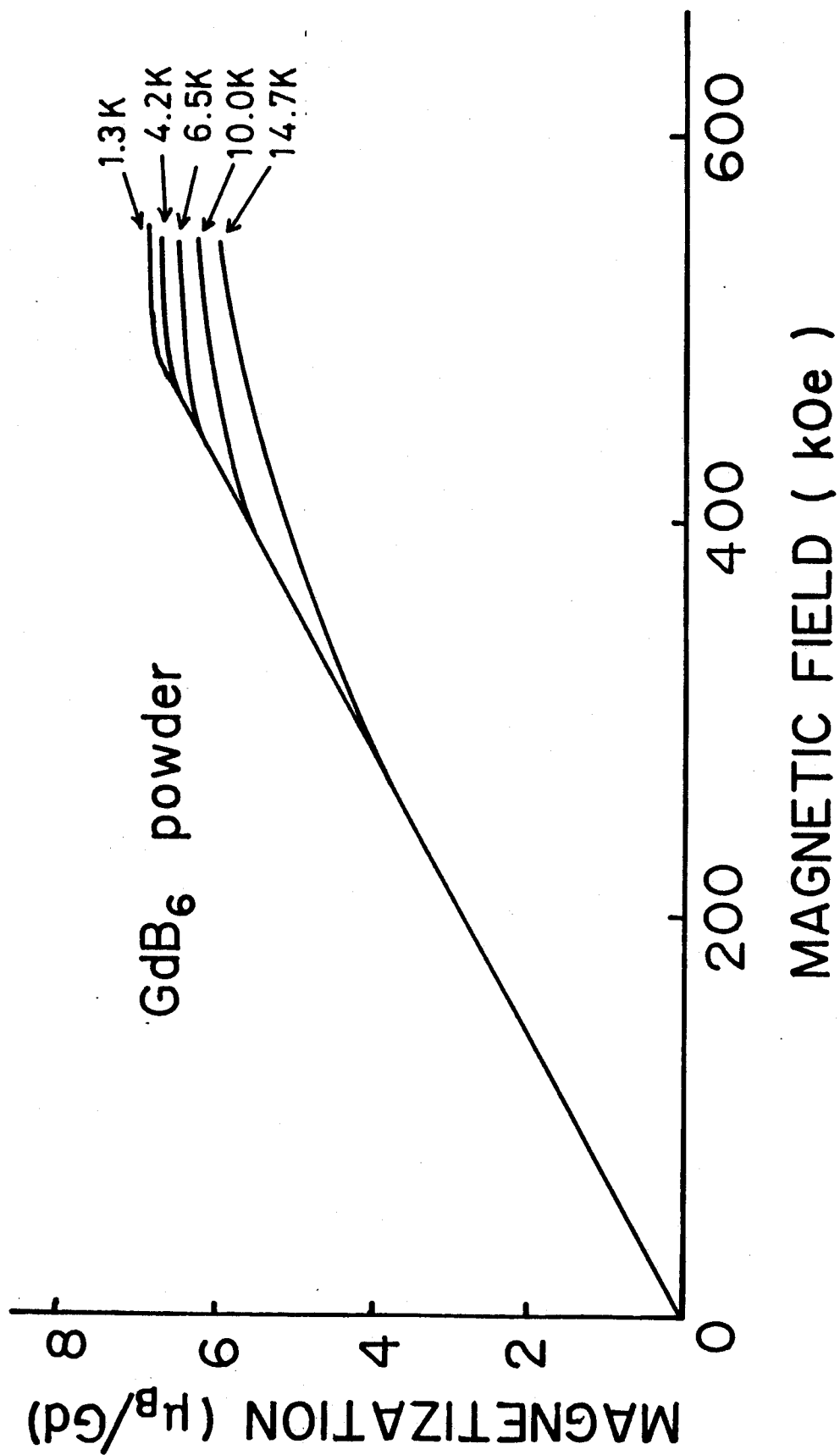


Fig.33 Magnetization curves of GdB₆ at various temperatures.

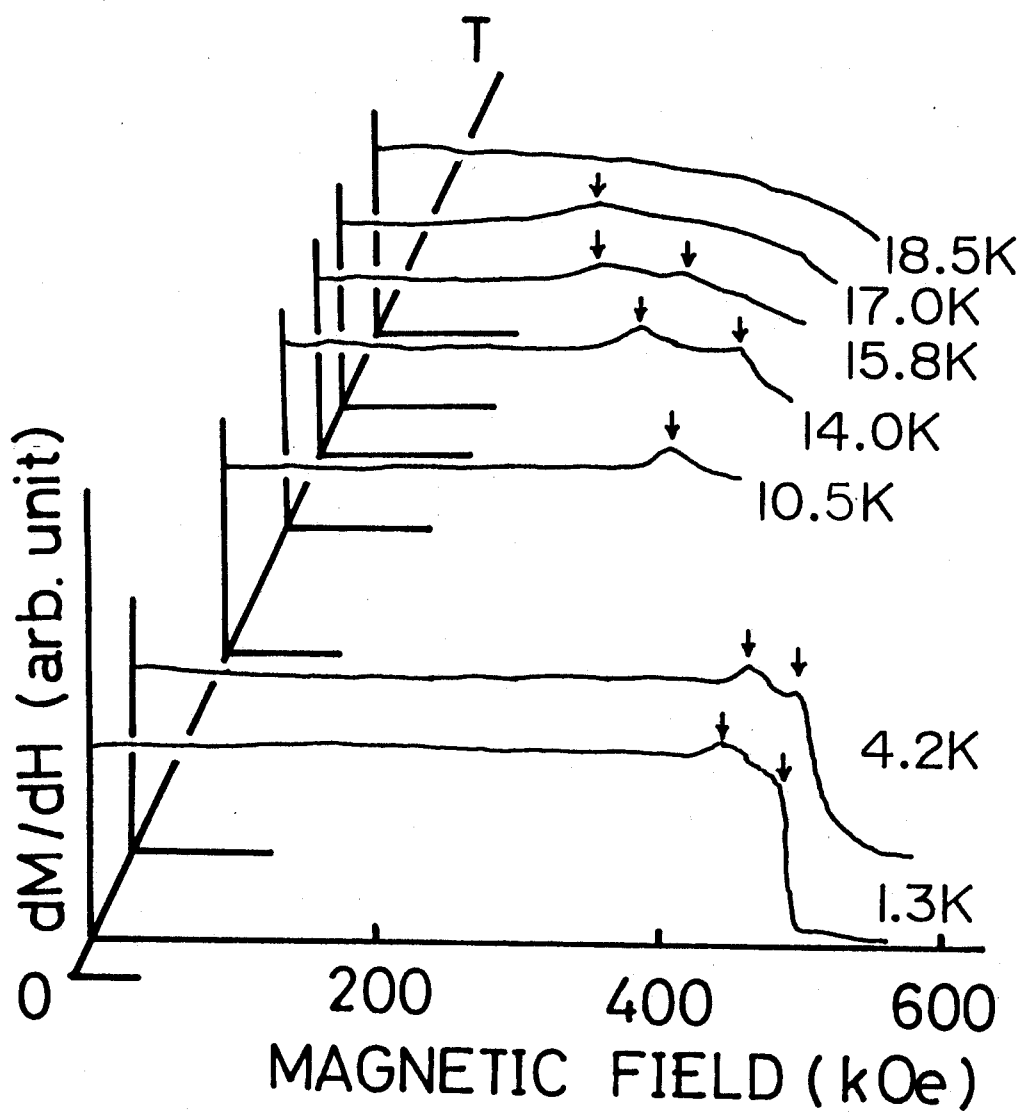


Fig.34 Temperature dependence of dM/dH_0 . Arrows show two critical fields where the small step-magnetizations are found.

two peaks are shown by arrows. These peaks indicate two small and sharp step-magnetizations at the corresponding fields. Amount of the step-magnetizations corresponds to about 1 % of the saturation moment. The peaks broaden and shift to the low magnetic field as temperature increases and the temperature dependences are shown in Fig.35. The higher field peak is called I at H_{c1} and the other is called II at H_{c2} .

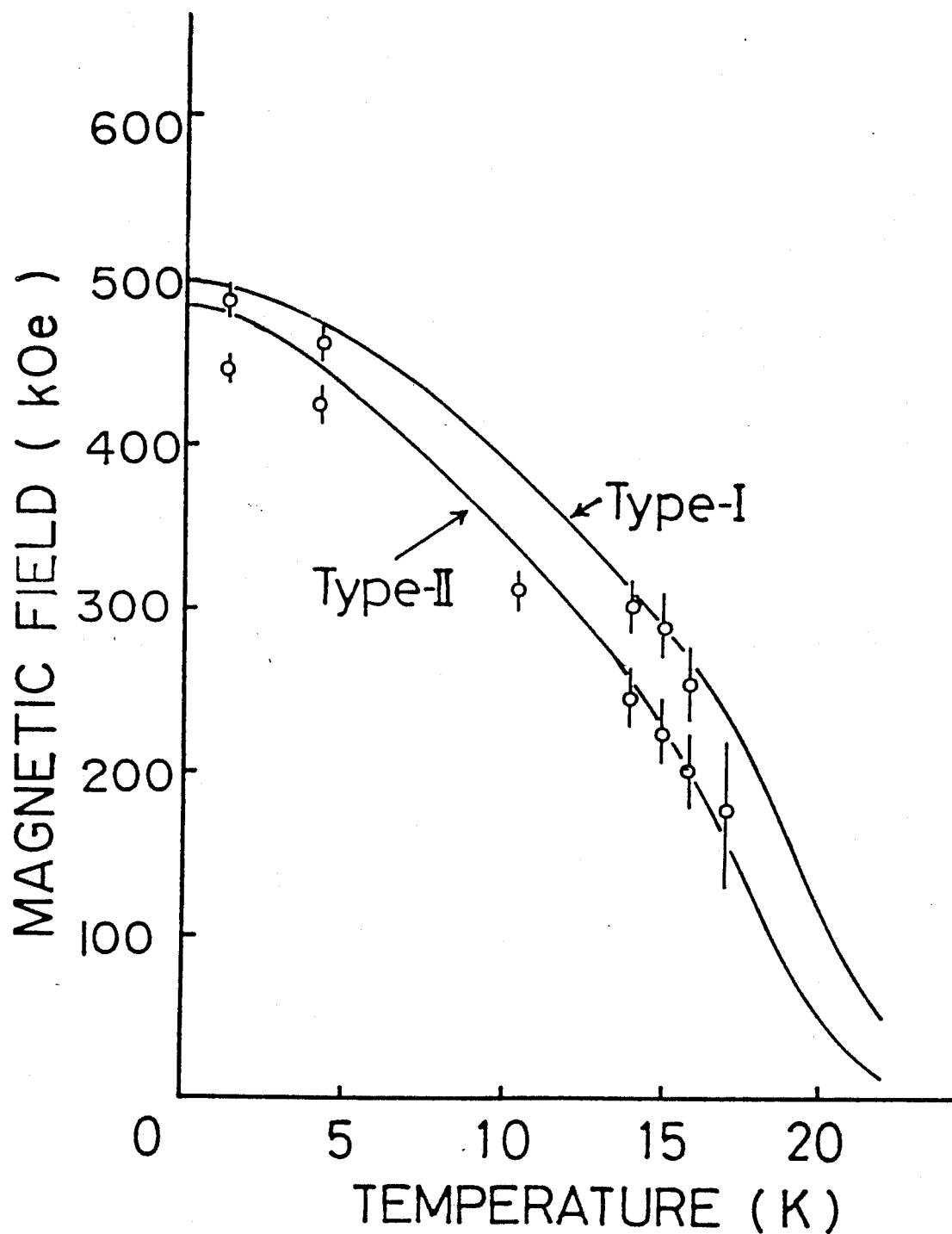


Fig.35 Temperature dependence of the step-magnetization fields H_{c1} and H_{c2} . Solid lines show the theoretical curves of H_{c1} and H_{c2} given in the text. Bars at the measuring points show the half width in dM/dH_0 .

§ 4 MAGNETIC STRUCTURE OF GdB_6

Neglecting the magnetic anisotropy energy, the critical field H_c is written by

$$H_c = 2H_E . \quad (4.1)$$

where H_E is the exchange field acting on each sublattice. Using value of 490 kOe for H_c , H_E is obtained as

$$H_E = 245 \pm 5 \text{ kOe} . \quad (4.2)$$

The single crystal data⁶⁾ show the spin flop field $\sqrt{2H_A H_E}$ of 6.5 kOe. Then the anisotropy field H_A is calculated to be

$$H_A = 86 \text{ Oe} . \quad (4.3)$$

Therefore, the anisotropy field is negligible as is expected.

Although the magnetic structure of GdB_6 is not known because of the lack of neutron diffraction study, the structure can be inferred to some extent by considering the measured value of H_E , Θ and T_N in the following way. Magnetic structures of a simple cubic antiferromagnet have been discussed for CaMnO_3 ¹⁰⁾ where A-, B-, C- and G-types are taken into account and these structures are shown in Fig.36. The A-type shows an antiferromagnetic stacking of ferromagnetic planes and the B-type is a simple ferromagnet. The C-type can be regarded as an antiferromagnetic bundle of ferromagnetic chains and the G-type is a simple

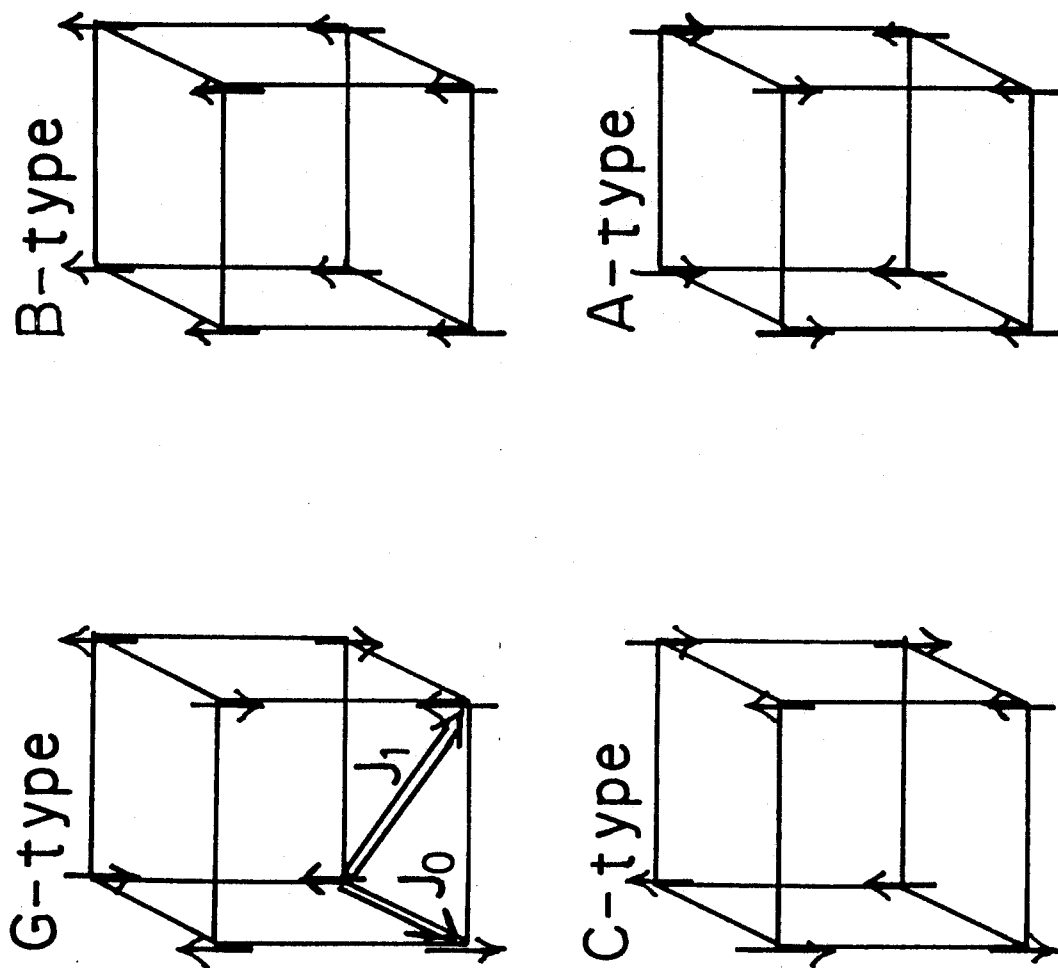


Fig.36 Four possible spin structures in a simple cubic magnet. Arrows show spins. J_0 and J_1 are defined in the figure.

antiferromagnet where all nearest neighbor pairs are antiferromagnetic.

The main exchange interaction in GdB_6 may be the RKKY interaction where the coupling between distant spins is not negligible. However, the exact evaluation of the exchange parameters with long distance is difficult because it is not a dilute system. Therefore, two exchange parameters J_0 and J_1 as are conventionally defined in Fig.36 are introduced to discuss the spin structure. Then the free energies per spin for A-, B-, C- and G-types are given by counting the neighboring spin number z in the same and different sublattices as

$$U_A = (-2J_0 + 4J_1) S^2, \quad (4.4)$$

$$U_B = - (6J_0 + 12J_1) S^2, \quad (4.5)$$

$$U_C = (2J_0 + 4J_1) S^2, \quad (4.6)$$

$$U_G = (6J_0 - 12J_1) S^2, \quad (4.7)$$

where the exchange parameters are defined by the Hamiltonian

$\mathcal{H}_{ij} = -2JS_i S_j$. The phase diagram based on eqs. (4.4) (4.7) are given in Fig.37. The phase boundary is obtained by comparing the corresponding free energies. For example, the $U_G - U_C$ boundary is obtained by putting $U_G = U_C$ and the boundary line, $J_1 = (1/4) J_0$ is given. The determination of the GdB_6 position on this diagram is done by considering the observed values of H_E , Θ and T_N . These values based on the mean field theory are given by well known formulae as

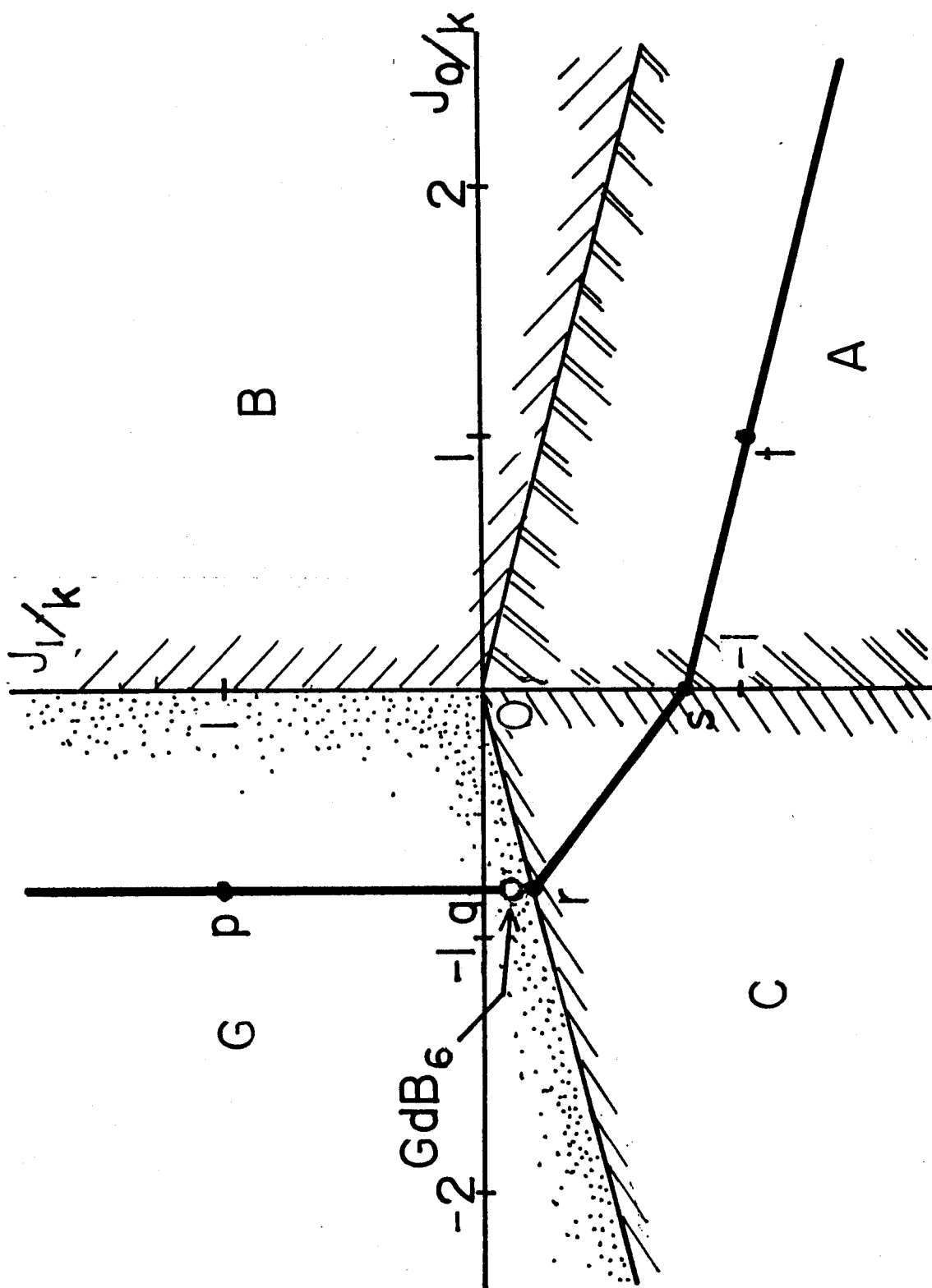


Fig.37 Phase diagram of simple cubic magnet with J_0 and J_1 .

Thick lines show the condition of $H_E = 245$ kOe.

$$H_E = \frac{2S}{g\mu_B} |\alpha|, \quad (4.8)$$

$$\Theta = \frac{2S(S+1)}{3k} (\alpha + \beta), \quad (4.9)$$

$$T_N = \frac{2S(S+1)}{3k} (\beta - \alpha), \quad (4.10)$$

where α and β are given by $\sum z_i J_i$, sum of the exchange parameters for the different and same sublattice spins, respectively. For example, $\alpha = 6J_0$ and $\beta = 12J_1$ for the G-type and $\alpha = 4J_0 + 8J_1$ and $\beta = 2J_0 + 4J_1$ for the C-type structure.

It is noted that experimentally obtained H_E of 245 kOe has high accuracy while Θ of -60 K has considerable errors. Experimentally speaking, the value scattered from about -50 K to -70 K.^{4),14)} Moreover, the observed value necessarily includes the effect of conduction electrons. The measured value of $T_N = 16$ K has high accuracy but the corresponding formula of eq.(4.10) is not so exact especially when the observed ratio of Θ/T_N is considerably larger than unity. It is 3.75 in GdB_6 so that the frustration effect might be expected in this spin system.

Considering these facts, the experimental result of H_E given by eq.(4.2) is adopted first and the exchange parameter α is determined by using eq.(4.8). The result is shown by thick lines in Fig.37. For example, α of the G-type is obtained as 4.7K so that J_0 is evaluated as 0.8 K in the G-region. Θ , T_N and Θ/T_N are evaluated along these lines with the formulae given by

eqs.(4.9) and (4.10) and the results for the point p (Θ , T_N , Θ/T_N) is shown as p (-77, 175, -0.44). Similarly, q (-49, 49, -1), r (-74, 25, -3), s (-74, 25, -3) and t (-43, 56, -0.76) are obtained. Θ , T_N and Θ/T_N are constant on the line in the C-type region. It is found that GdB_6 may be in the C-type region or in the A- or G- type near the boundary to the C-type structure. The possible spin structure is inferred by considering the radial dependence of the RKKY interaction. Although the r-dependence of RKKY interaction in GdB_6 does not follow the exact curve of $(1/x^4)(-x \cos x + \sin x)$ with $x = 2k_F r$ where k_F is the wave number at the Fermi surface, the qualitative r-dependence may be acceptable. Figure 38 shows the RKKY exchange energy as a function of $2k_F r$. As r of $J_0(r_0)$ and $J_1(r_1)$ is a and $\sqrt{2}a$ with $a=4.111$ A respectively, the ratio of r_0/r_1 is $1/\sqrt{2}$. Looking at the observed Θ and T_N with the possible J-values of J_0 and J_1 in Fig.38, the probable J-values are estimated as

$$\left. \begin{array}{l} J_0 = -0.78 \text{ K} , \\ J_1 = -0.17 \text{ K} , \end{array} \right\} \quad (4.11)$$

with $\Theta = -71$ K, $T_N = 28$ K and $\Theta/T_N = -2.5$. The corresponding point on the phase diagram is in the G-type region as is shown in Fig.37. Therefore, the G-type spin structure is most acceptable in GdB_6 but the possibility of the C-type still remains because the determination of J_0 and J_1 in eq.(4.11) is not so exact and the coincidences of Θ and T_N in the theory and experiment is not so satisfactory. Moreover, the estimated point is very close to

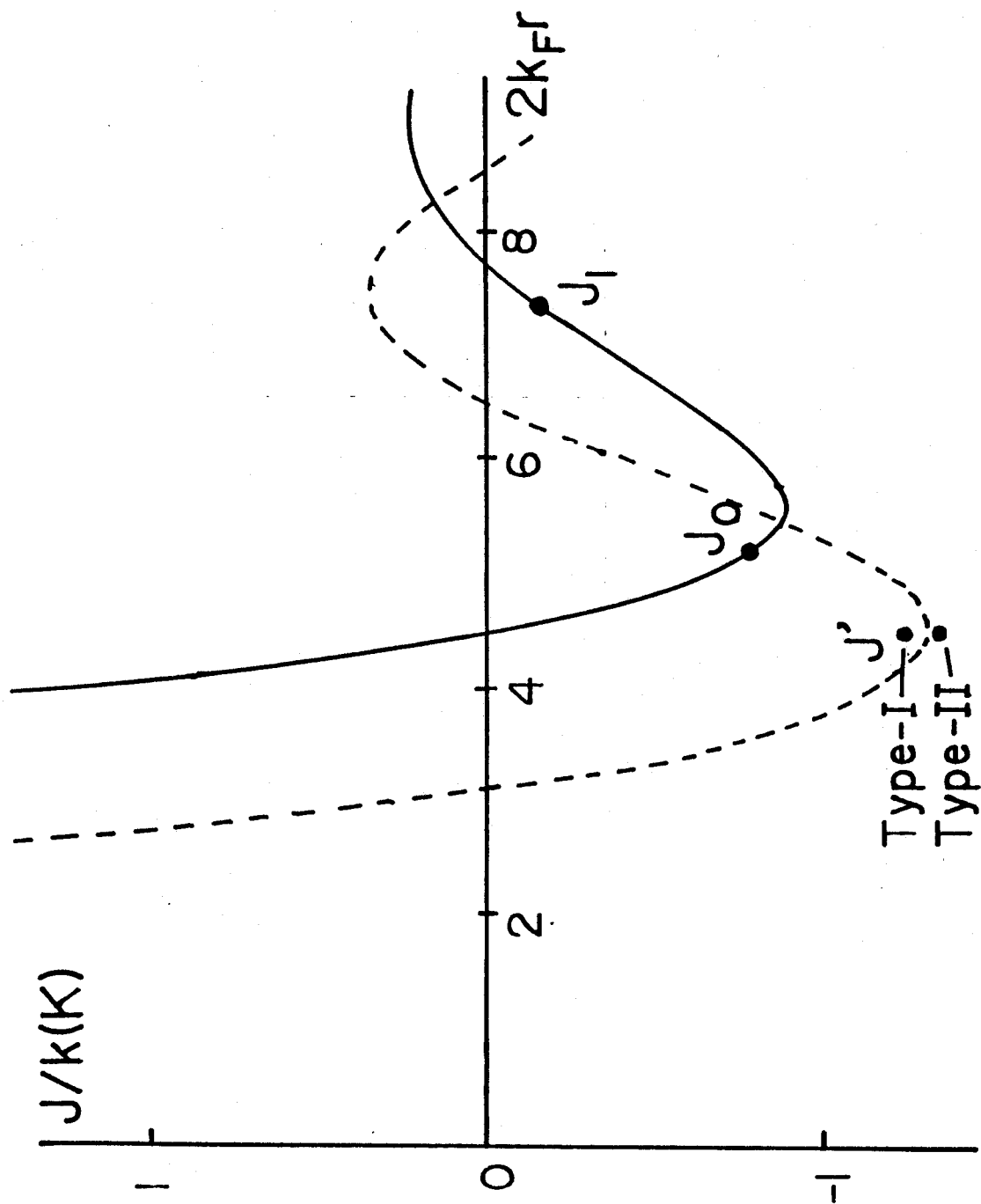


Fig.38 RKKY exchange energy vs. $2k_F r$ between two localized spins. The point J' will be given in Section 5.

the C-region. The helical spin model should also be considered but it is complex and no experimental evidence to expect the helical structure has been reported. Therefore, the possibility is not discussed in the present paper.

§ 5 DISORDERED MODEL

A possible model of the anomalous step-magnetizations is presented in this section. The observed two peaks in Fig.34 is difficult to attribute to the phase transition boundary because the signals are very small. For example, the typical changes in the magnetization due to spin-flop transition, antiferromagnetic-helical transition and antiferromagnetic-paramagnetic transition has been reported in NiBr_2 ¹⁵⁾ where these peaks show very large dM/dH_0 anomalies. The observed dM/dH_0 peaks in GdB_6 are sharp and the width is about 10 kOe. Therefore, no angular dependence in the single crystal is expected. This means that the Ising-like impurity spin flop is eliminated. The Heisenberg-like impurity spins will follow the motion of host spins so that the step-magnetization is not expected. Moreover, the observed steps have about 1 % of the host magnetization while the net magnetic moment from the expected amount of the impurities are about one tenth of the observed steps. Therefore, the impurity spin effect may be out of the question.

The experimental results can be explained by introducing the following disordered model. Consider a substitutional Gd atom on the B_6 site as is given by hatched circles in Fig.39-(a). It is surrounded by eight Gd atoms in the Type-I and seven Gd atoms in the Type-II where one Gd atom in the regular position is replaced by a B_6 cluster. In other words, the Type-II is produced by exchanging a pair of the neighboring Gd and B_6 atoms. In Type-I, however, the substituted B_6 cluster is considered to be far from the substituted Gd atom so that the disordered Gd is located in a

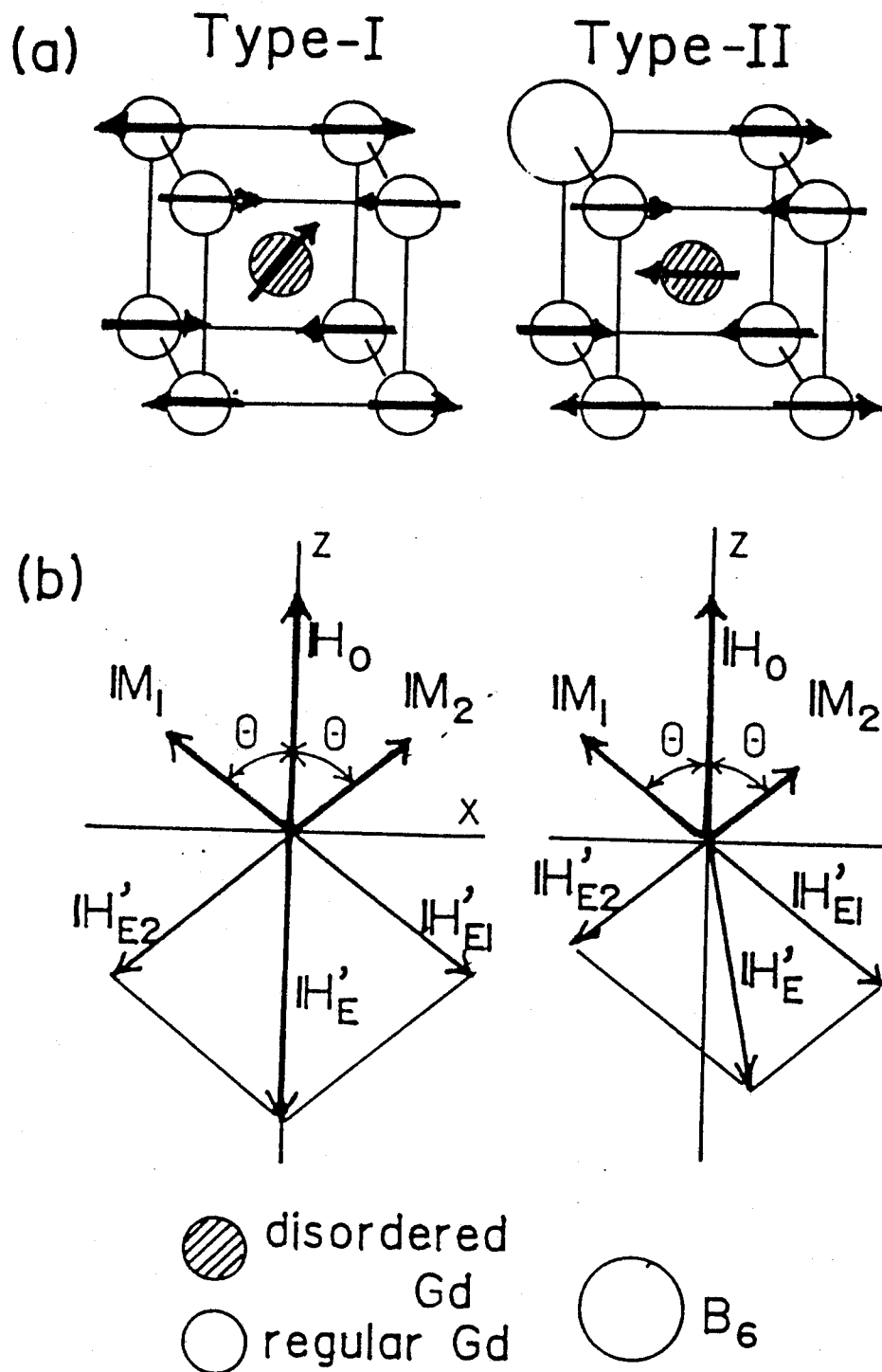


Fig.39 a) shows two kinds of disordered model at zero magnetic field. Antiferromagnetic nearest neighbor Gd spins are also shown. b) shows the sublattice moments and the local exchange field H'_E on the disordered Gd spin under an external magnetic field H_0 .

field of cubic symmetry.

Consider a disordered Gd spin of the Type-I in the G-type antiferromagnet. The nearest neighbor antiferromagnetic exchange interaction J' is assumed between the regular and disordered spins. Under zero external magnetic field, the net field on the disordered spin is zero because the surrounding eight host spins are antiferromagnetically ordered. The local field under an external field H_0 is shown in Fig.39-(b) where the net exchange field $\vec{H}_{E1} + \vec{H}_{E2}$ coming from two sublattice moments \vec{M}_1 and \vec{M}_2 is exactly antiparallel to H_0 . It is assumed that the surrounding Gd spins point in the same direction of the host majority spins.

The total effective field H_{eff} acting on the disordered Gd under an external field H_0 is then given by

$$\left. \begin{aligned} \vec{H}_{\text{eff}} &= \vec{H}_0 + \vec{H}_{E1} + \vec{H}_{E2} , \\ H_{\text{eff}z} &= H_0 - (H'_{E1} + H'_{E2}) \cos \theta . \end{aligned} \right\} \quad (5.1)$$

H'_{E1} and H'_{E2} are obtained by counting the number of neighboring spins as

$$H'_{E1} = H'_{E2} = 4J'(2S/g\mu_B) . \quad (5.2)$$

$\cos \theta$ is given by the standard formula of antiferromagnetism as

$$\cos \theta = \frac{H_0}{H_c} = \frac{H_0}{2H_E} = \frac{H_0}{12J_0(2S/g\mu_B)} . \quad (5.3)$$

Then the effective field is written by

$$H_{\text{eff}} = H_0 (1 - 2J'/3J_0) , \quad H_0 < H_c . \quad (5.4)$$

Eq.(5.4) means that the effective field on the disordered spin is proportional to H_0 with the parallel or antiparallel direction to H_0 depending on the magnitude of J'/J_0 . Consider a case where $2J'/3J_0 > 1$. Then the effective field is negative and the disordered magnetic moment points in the opposite direction of H_0 . $H'_{E1} + H'_{E2}$ become constant above H_c because of the saturation of $M_1 + M_2$ so that the effective field is given by

$$H_{\text{eff}} = H_0 - 8 |J'| (2S/g\mu_B) , \quad H_0 > H_c . \quad (5.5)$$

Consequently, the effective field is zero when the external field is given by H_{c1} written as

$$H_{c1} = 8 |J'| (2S/g\mu_B) . \quad (5.6)$$

Therefore, the disordered Gd spin will flip at this field with a small metamagnetic transition at low temperatures. The magnetic field dependence of H_{eff} is illustrated in Fig.40.

The disordered spin in the Type-II can be treated in a similar manner except the fact that one of Gd atom at the nearest neighbor regular site is replaced by a nonmagnetic B_6 cluster. As is seen in Fig.39-(b), x component of the effective field is taken into account and $H_{\text{eff}z}$ and $H_{\text{eff}x}$ are given by

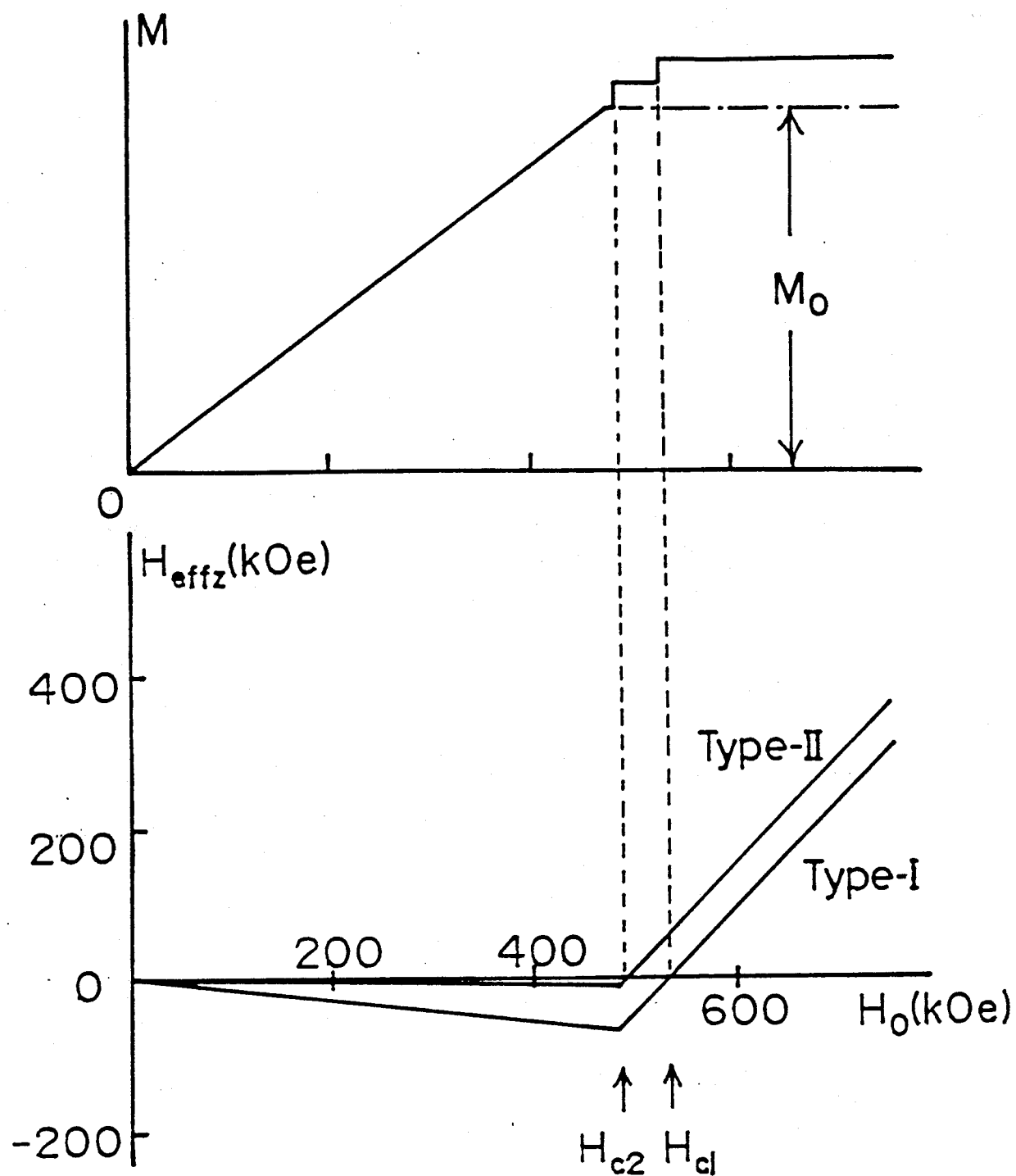


Fig.40 Z components of effective magnetic field H_{effz} acting on the disordered Gd sites and resultant magnetization at 0K. M_0 is regular Gd spin magnetization and two steps above M_0 come from the disordered Gd spins.

$$\left. \begin{aligned} H_{\text{eff}z} &= H_0 - (H'_{E1} + H'_{E2}) \cos \theta , \\ H_{\text{eff}x} &= (H'_{E1} - H'_{E2}) \sin \theta , \end{aligned} \right\} \quad (5.7)$$

with

$$H'_{E1} = 4J'(2S/g\mu_B) , \quad H'_{E2} = 3J'(2S/g\mu_B) . \quad (5.8)$$

The same formula eq.(5.3) is used for $\cos \theta$. Under $H_0 < H_c$ the effective field components are given by

$$\left. \begin{aligned} H_{\text{eff}z} &= H_0 (1 - 7J'/12J_0) , \\ H_{\text{eff}x} &= J'(2S/g\mu_B) \sqrt{1 - \left\{ \frac{H_0}{12J_0(2S/g\mu_B)} \right\}^2} , \end{aligned} \right\} \quad H_0 < H_c , \quad (5.9)$$

where the spin axis at zero field is assumed to point in the x-direction. The effective field above H_c is given by

$$\left. \begin{aligned} H_{\text{eff}z} &= H_0 - 7|J'| (2S/g\mu_B) , \\ H_{\text{eff}x} &= 0 , \end{aligned} \right\} \quad H_0 > H_c . \quad (5.10)$$

Consequently, the metamagnetic transition can be expected at the critical field given by

$$H_{c2} = - 7 |J'| (2S/g\mu_B) . \quad (5.11)$$

The effective field and the corresponding magnetization are shown in Fig.40.

It should be noticed that the disordered model is also applicable to the C-type antiferromagnet because the net field on the disordered spin is exactly same for both types.

The temperature dependence of the critical fields H_{c1} and H_{c2} can empirically be evaluated in the following way. Spin S in eqs.(5.2), (5.3) and (5.8) under a magnetic field H_0 should be written by the thermal average value $\langle S(H_0) \rangle$ at finite temperatures. This value can be estimated from the temperature dependent magnetization curves given in Fig.33. The obtained H_{effz} are shown in Fig.41 for the Type-I and II spins and the corresponding H_{c1} and H_{c2} are shown by solid lines in Fig.35. The result shows satisfactory agreement with the experimental results.

It is noted that the metamagnetic steps at H_{c1} or H_{c2} are regarded as a paramagnetic spin flip under the field of H_{eff} . Therefore, the peak height $\Delta\chi$ defined in the insert of Fig.42 corresponds to the zero effective field susceptibility so that it should follow the Curie law. Figure 42 shows the inverse of $\Delta\chi$ where a clear linear dependence is found. This means that the disordered spin can be considered as paramagnetic. The Curie constant C of the $\Delta\chi$ peak is also investigated and it is found that about 1 % of the host spin is regarded as the population number of the disordered spins.

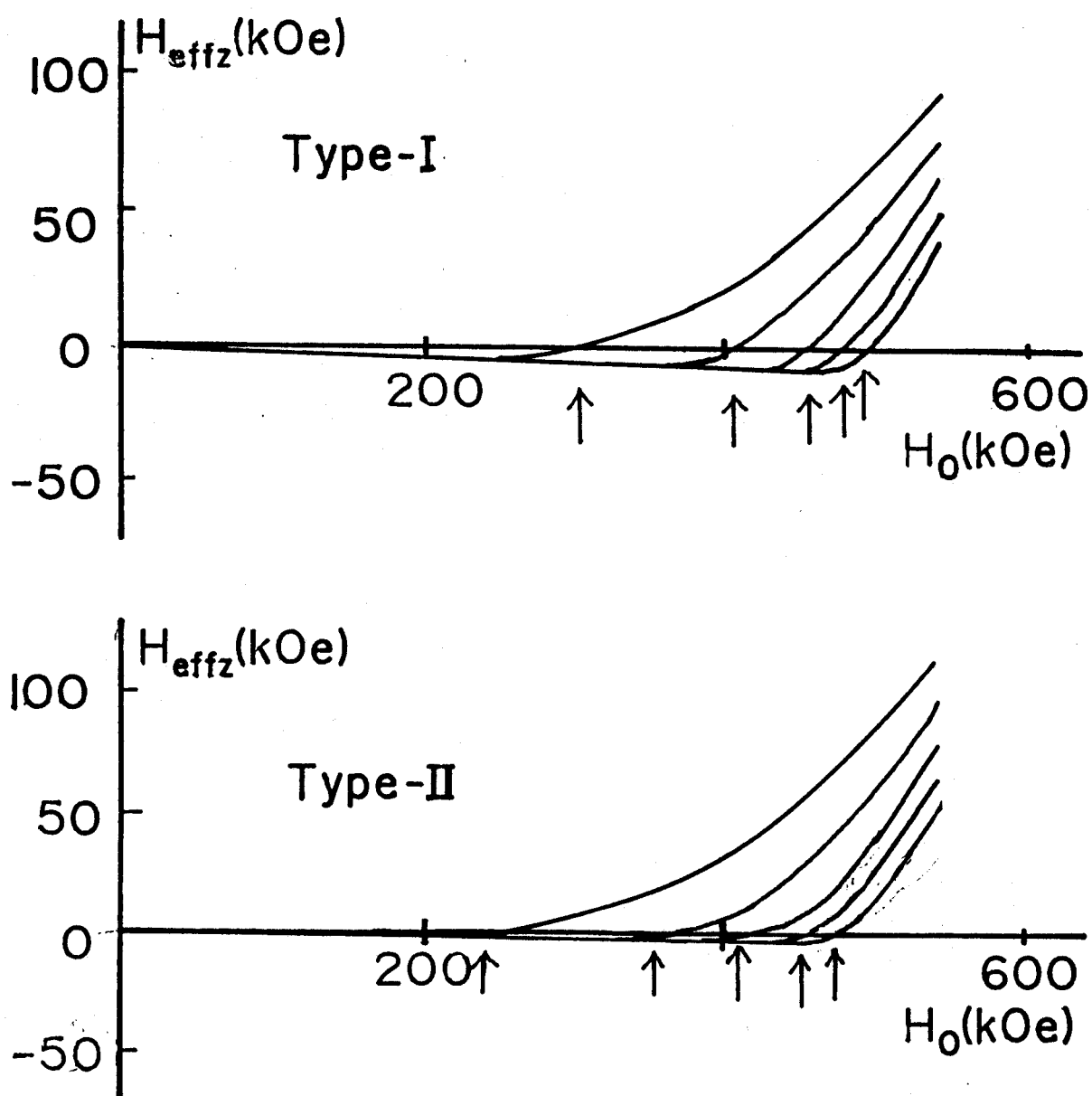
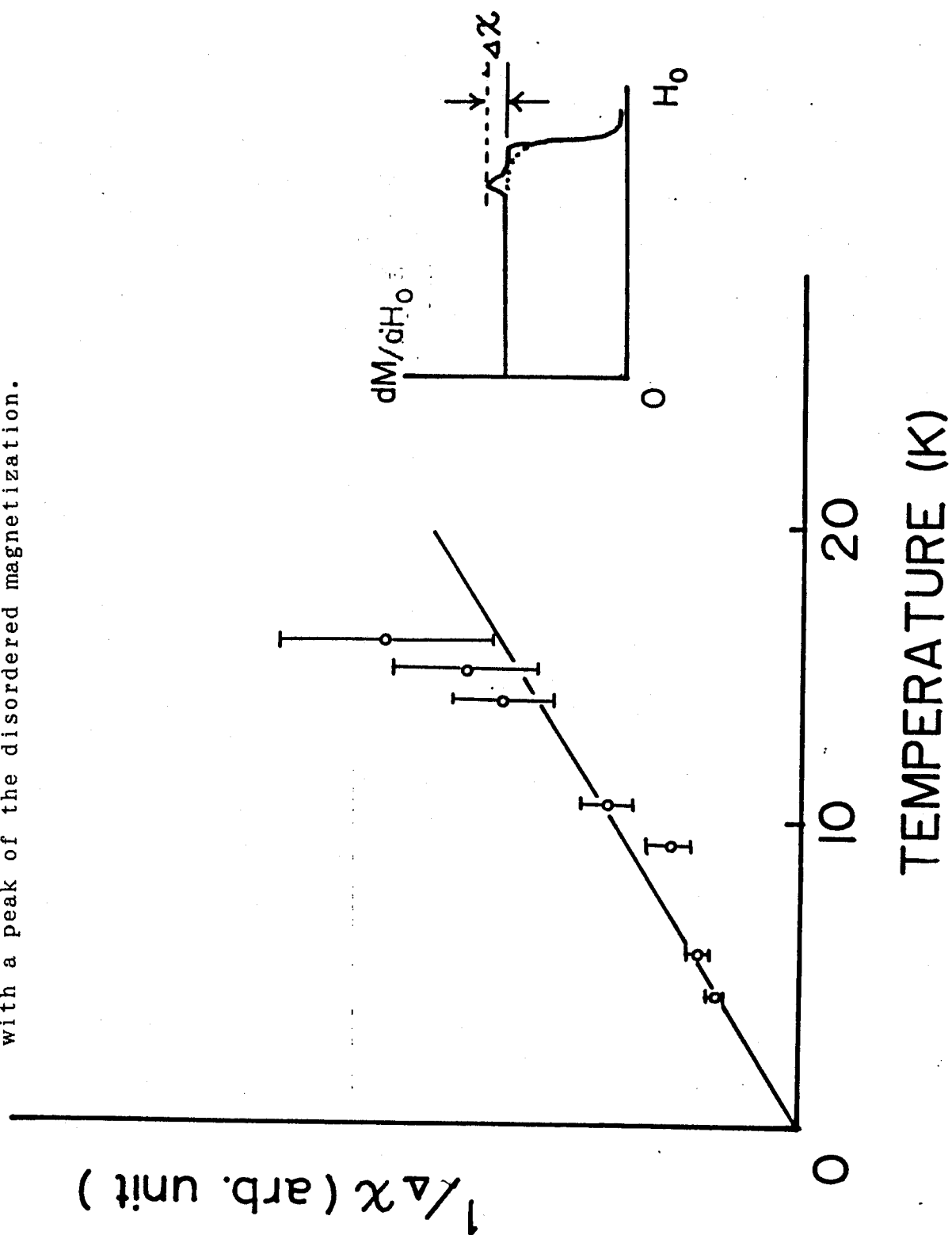


Fig.41 Temperature dependence of H_{effz} . Arrows show the H_{c1} in Type-I and H_{c2} in Type-II.

Fig.42 Temperature dependence of inverse magnetic susceptibility of the magnetization of Type-II spin. Bars show an experimental errors. The insert shows a schematic dM/dH_0 curve with a peak of the disordered magnetization.



The exchange parameter J' for the Type-I and II spins are estimated by using eqs.(5.6) and (5.11) and the results at 0 K are given by

$$J'/k = -1.2 \text{ K} , \quad \text{Type-I} , \quad (5.12)$$

$$J'/k = -1.3 \text{ K} , \quad \text{Type-II} . \quad (5.13)$$

These values are plotted in Fig.38. It is clear that these points deviate a little from the original RKKY curve estimated by J_0 and J_1 in the host spin system. This may qualitatively explained in the following way. The local electron density near the disordered Gd increases because the charge neutrality is broken by introducing the interstitial Gd^{3+} at the B_6 site. Accordingly, the RKKY interaction may be enhanced with increasing k_F and the effect will modify the curve as is schematically drawn by dotted curve in Fig.38. The quantitative treatment are of course difficult so that it is not discussed further.

The disordered model proposed in the present paper is familiar in usual metallic alloys. However, it is not so easy to realize in rare earth hexaborides because the network of rare earth atom and B_6 cluster is tight and compact. The ionic contribution of the coupling bond may also be important. Of these hexaborides, SmB_6 is well known as a stable compound while GdB_6 single crystal is usually not so high in quality. This may be one of the reasons why the disordered Gd of about 1 % is found in GdB_6 . After the discovery of the disordered Gd in GdB_6 , the similar defect was investigated in SmB_6 by ESR techniques¹⁶⁾ and

about 10~100 ppm of the disordered Sm centers are found in the semiconductive SmB_6 . Many valence states of the disordered Sm appears in SmB_6 reflecting various ways of satisfying the charge neutrality condition.

REFERENCES

- 1) R. W. G. Wychoff : Crystal Structure (Interscience, New York, 1967) vol.2 p.202.
- 2) T. Kasuya, K. Takegahara, Y. Aoki, K. Hanzawa, S. Kunii, T. Fujita, N. Sato, H. Kimura, T. Komatsubara, T. Furuno and J. Rossat-Mignod: Valence Fluctuation in Solid, ed. L. M. Falicov, W. Hanke and M. P. Maple (North Holland 1981) p.215.
- 3) T. Kasuya, K. Kojima and M. Kasaya: Valence Instabilities and Related Narrow-Band Phenomena ed. R. D. Parks (Plenum Press New York 1977) p.137.
- 4) H. Hacker, Jr., Y. Shimada and K. S. Chung: Phys. Status Solidi (a) 4 (1971) 459.
- 5) S. Kunii, K. Takeuchi, I. Oguro, K. Sugiyama, A. Ohya, M. Yamada, Y. Koyoshi, M. Date and T. Kasuya: J. Magn. & Magn. Mat. 52 (1985) 275.
- 6) H. Nozaki, T. Tanaka and Y. Ishizawa: J. Phys. C (Solid State Phys.) 13 (1980) 2751.
- 7) D. E. Miller and H. Hacker, Jr.: Solid State Commun. 9 (1971) 881.
- 8) E. F. Westrum, Jr.: Progress in the Science and Technology of the Rare-earths (Pergamon, Oxford, 1968) vol.3 p.459.
- 9) K. Sugiyama, Y. Koyoshi, S. Kunii, T. Kasuya and M. Date: J. Phys. Soc. Jpn. 55 (1986) 37.
- 10) E. O. Wollan and W. C. Koehler: Phys. Rev. 100 (1955) 545.
- 11) A. Yamagishi and M. Date: High Field Magnetism ed. M. Date (North-Holland, Amsterdam, 1983) p.289.
- 12) K. Okuda and M. Date: J. Phys. Soc. Jpn. 27 (1969) 839.

- 13) T. Sakakibara, H. Mollimoto, M. Motokawa and M. Date: High Field Magnetism ed. M. Date (North-Holland, Amsterdam, 1983) p.299.
- 14) Z. Fisk, R. H. Taylor and B. R. Coles: J. Phys. C4 (1971) L292.
- 15) K. Katsumata, K. Sugiyama and M. Date: J. Phys. Soc. Jpn. 52 (1983) 3312.
- 16) T. Uemura, Y. Chiba, M. Hagiwara and M. Date: J. Phys. Soc. Jpn. 55 (1986) 3737.

PART II - B -

FIELD-INDUCED METALLIC STATE IN YbB_{12} UNDER HIGH MAGNETIC FIELD

ABSTRACT

High field magnetization and magnetoresistance of YbB_{12} are investigated up to 550 kOe at low temperatures with special interest in the semiconductive band gap energy under the field. Very large negative magnetoresistance is found and the system undergoes perfect metallic phase around 500 kOe with anomalous increase in the magnetization. The experimental results are explained by introducing the model that the band gap produced by the mixing of the f- and conduction electrons is destroyed by applying the field and the released f-electron gives an anomalous magnetization. The gJ-value is estimated as 1.9 for the f-level and this means that Γ_8 may be most favourable for the responsible f-electron at the Fermi energy.

§ 1 INTRODUCTION

Ytterbium dodecaboride, YbB_{12} with a UB_{12} type crystal structure¹⁾ has been investigated extensively with special interests in the band gap on the Fermi energy. The first detailed study of this material has been done by Kasaya et al. in 1983.²⁾ They found that the system is semiconductive with the forbidden band gaps above the Fermi level. The semiconductive nature is rather exceptional in these compounds because most rare earth borides are metallic and similar exception is known only in SmB_6 . The magnetic susceptibility shows a broad maximum at about 70 K below which the value decreases and becomes constant at liquid helium temperatures. The magnetic susceptibility,³⁾ electrical resistivity,³⁾ Hall effect,³⁾ NMR,³⁾ specific heat,³⁾ XPS⁴⁾ and point-contact spectroscopy⁵⁾ experiments have been reported. These data support that YbB_{12} is a mixed-valence compound accompanied with the energy gaps on the Fermi energy. The magnetic susceptibility at enough low temperature is attributed to the Van Vleck term except a small Curie-Weiss contribution due to impurities. The origin of the band gaps is not clear but may be attributed to either the hybridization effect⁶⁾ or the formation of the Wigner lattice by heavy polarons.⁷⁾

Recently, it is found that the observed band gap of 60 K is quenched by applying a magnetic field of about 500 kOe at liquid helium temperatures and the preliminary report is presented by our group.⁸⁾ Around 500 kOe, the system is perfectly metallic with a sharp increase in the magnetization. The observed

phenomena were explained by the model that the f-level lying close to the Fermi level splits by the magnetic field and the band gap is quenched. However, the model is too simple and the quantitative discussion was not done.

The detailed experimental results and the band gap quenching are quantitatively analyzed in Part II-B. The mixing of the f- and conduction electrons is treated semiempirically and the anomalous magnetization is explained by the f-electron polarization under high magnetic field.

§ 2 ELECTRIC AND MAGNETIC PROPERTIES

The crystal structure of YbB_{12} is isomorphous to UB_{12} with the lattice parameter of 7.469 \AA ^{1),9)} and it can substantially be regarded as the NaCl type if a B_{12} dodecahedron is replaced by a simple anion. The crystal structure is illustrated in Fig.43.

The Yb atom in YbB_{12} has a mixed valence of $+2.9$.²⁾⁻⁴⁾ i.e., it is close to trivalent ion. The rare earth dodecaborides RB_{12} are usually metallic as is expected from the electronic energy band calculation of LuB_{12} ¹⁰⁾ However, the electrical resistivity given in Fig.44 shows two semiconductive energy gaps 2Δ and Δ' of about 60 K and 120 K respectively, for main energy gaps. The electrical resistivity below 5 K may be explained by the impurity conduction. The Hall coefficient measurement³⁾ supports the two-activation model.

The magnetic susceptibility data are shown in Fig.45. Full line is taken from the static measurement.³⁾ The Curie-Weiss constant Θ is estimated as -79 K above 200 K and the susceptibility χ shows a broad maximum around 70 K below which χ decreases as temperature decreases. Below 20 K, the magnetic susceptibility increases again with decreasing temperature. This may be due to the impurity effect and the intrinsic magnetic susceptibility evaluated from the ^{11}B Knight shift is constant below 20 K which is shown by a dotted line in Fig.44. No magnetic order effect is found in the NMR study³⁾ so that the system can be regarded as a nonmagnetic semiconductor. The constant value of the susceptibility at low temperature may be due to the Van Vleck susceptibility of f-electrons.

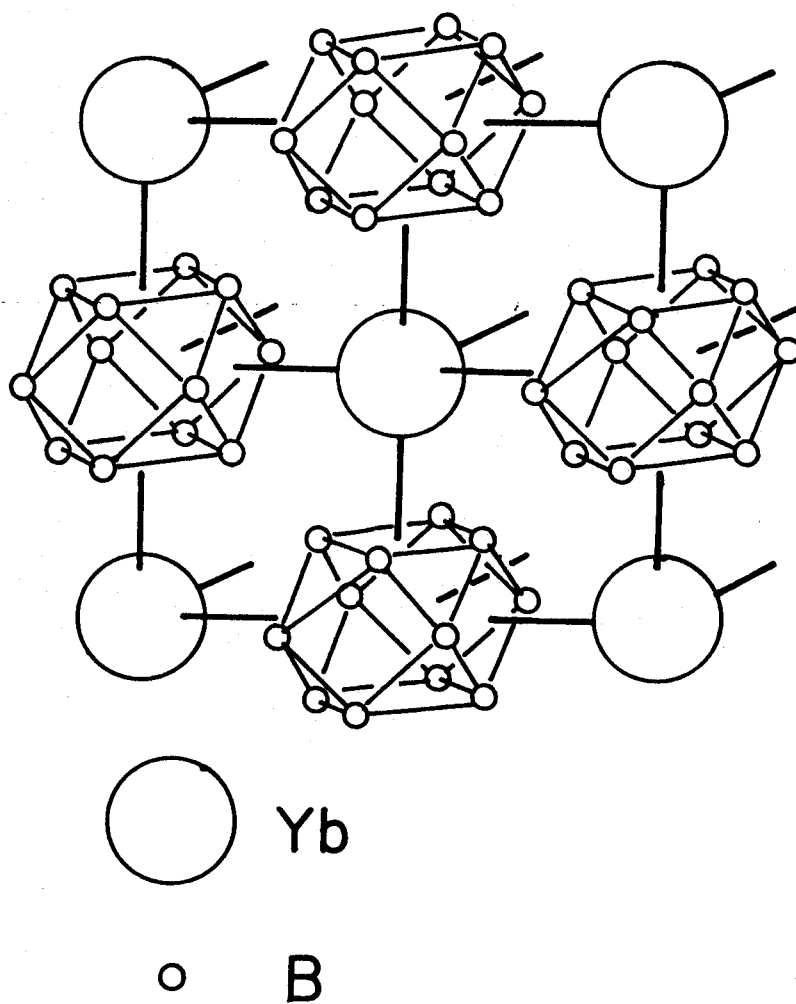


Fig.43 Crystal structure of YbB_{12} .

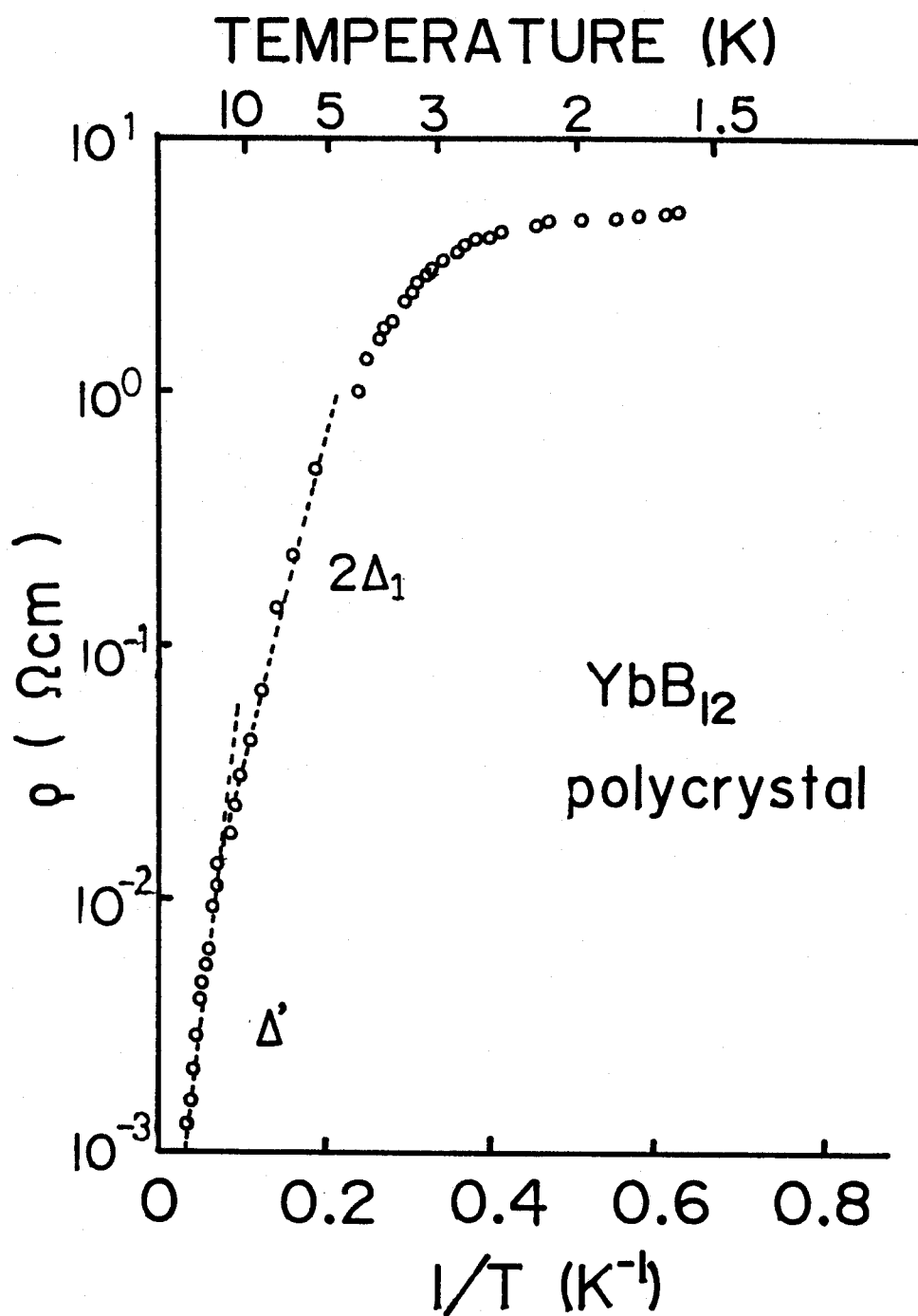


Fig.44 Temperature dependence of electrical resistivity of YbB₁₂. $2\Delta_1$ and Δ' mean the energy gaps on the Fermi energy.

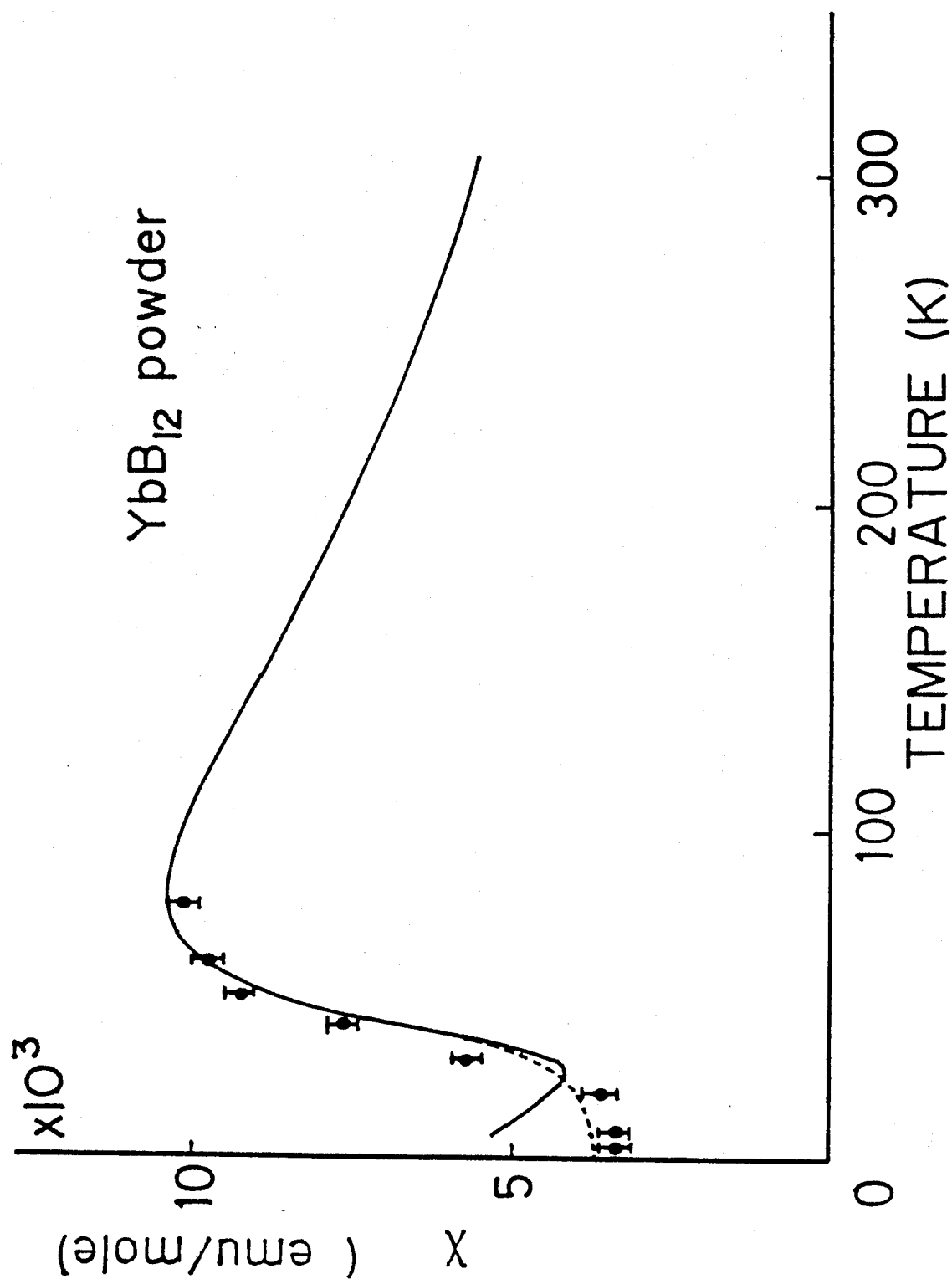


Fig.45 Magnetic susceptibility vs temperature. The solid line is taken from reference 3 and the dotted line is obtained from NMR measurement. Plotted points show the intrinsic susceptibilities given in section 4.

§ 3 EXPERIMENTAL PROCEDURES

The samples used in the present experiments are kindly supplied by the Kasuya group, Tohoku University. They prepared the samples by borothermal reduction $\text{Yb}_2\text{O}_3 + 27\text{B} \rightarrow 2\text{YbB}_{12} + 3\text{BO}$ under vacuum at 2200 °C which is just below the melting point.^{3),4)} The product usually contains a slight amount of YbB_6 and YbB_{66} depending on the temperature used in the heat treatment. These ingredients are reactive to diluted nitric acid so that they can be washed out by the acid in the powder stage. The single phase YbB_{12} is checked carefully by X-ray analysis.

The high field magnetization measurements are done at High Magnetic Field Laboratory, Osaka University.¹¹⁾ The details are shown in Part II-A and so it is neglected here.

The magnetization measurements are carried out for the powder sample with the standard pick-up-coil system. The details are shown elsewhere.^{13),14)}

The longitudinal magnetoresistance $\rho(H_0)$ was measured by the standard four-probe method with a square pulsed current that was synchronized with the field generation. The block diagram is shown in Fig.46. Unbalanced signals produced in the four-probe circuit was compensated with a small coil wound close to the sample. The signal was also stored in the digital recorder, Iwatsu DM-901, and the residual noise was eliminated by subtraction of the reversed current data.

There are some heating mechanisms of magnetic metal in a pulsed field, and in some cases the temperature change during the measurement can not be neglected. The experimental tests of the

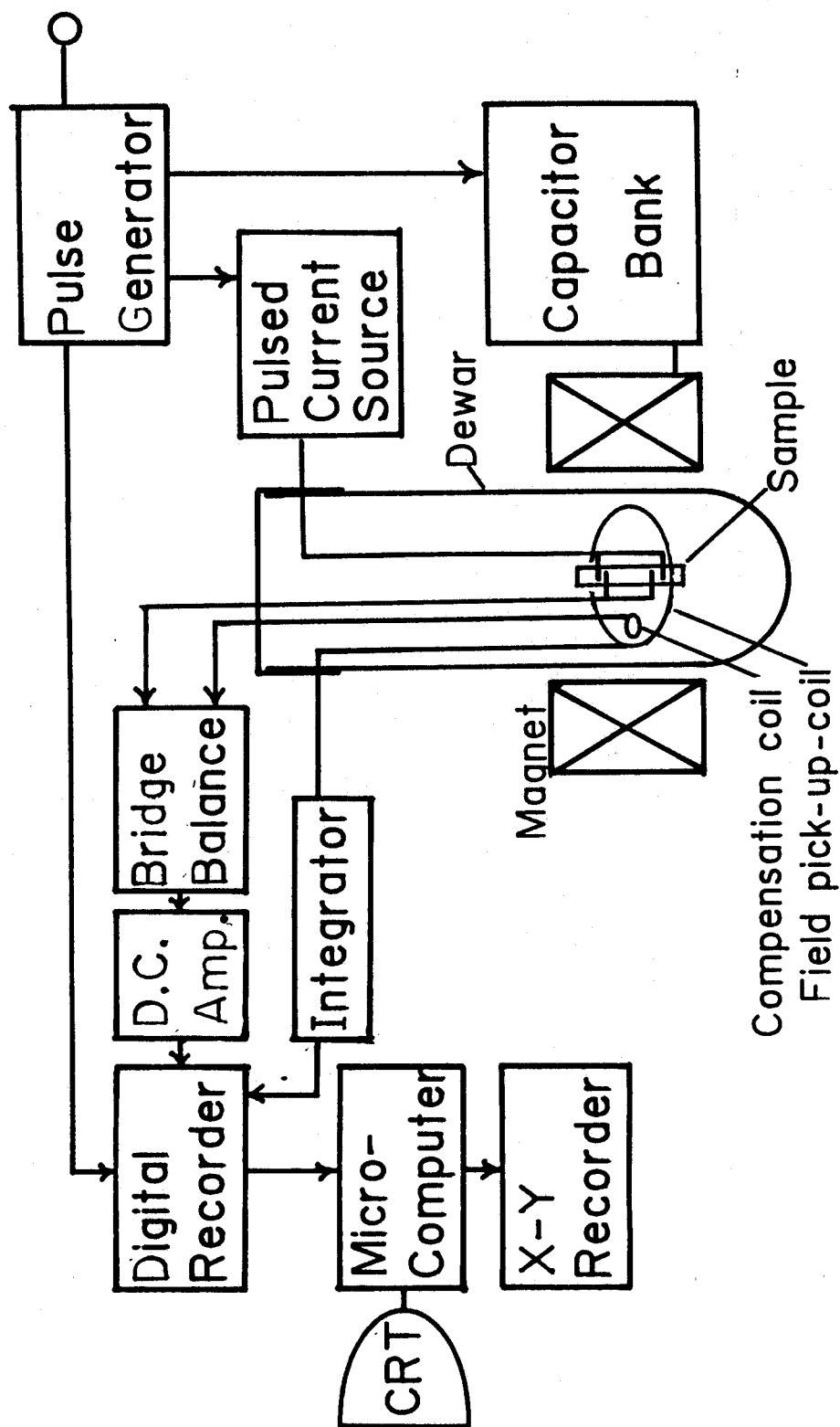


Fig. 46 Block diagram of the magnetoresistance measurement system.

heating and cooling processes are investigated and corrections for obtaining isothermal magnetoresistance are considered.

The size of the sample is $2 \times 1 \times 0.3 \text{ mm}^3$ and the Joule heating was not serious in the present experiment. However, care should be taken for the magnetocaloric effect due to paramagnetic impurities especially at low temperatures. For example, several degrees in the temperature increase is expected at 1.3 K. The thermal relaxation time for the powder material is of the order of 10^{-7} sec so that the effect is negligible in the magnetization measurement for powder but it is about 10^{-3} sec for the magnetoresistance sample. The standard way of obtaining isothermal magnetoresistance data in such a case has been developed by our group¹⁵⁾ and the details are not shown here. The central idea of the procedure is the selfconsistent replotting of the magnetoresistance curves constructed from an ensemble of non-isothermal measured curves.

§ 4 EXPERIMENTAL RESULTS

The magnetization curve at 4.2 K is shown in Fig.47 where the magnetization is given by the Bohr magneton (μ_B) unit per Yb atom. The solid curve is the measured magnetization which consists of three parts. Non-linear part below 100 kOe may come from paramagnetic impurities and the linear intrinsic magnetization curve, which is obtained by subtracting the impurity paramagnetic magnetization from the measured line, is illustrated by a dotted line. An anomalous magnetization appears above 450 kOe. The impurity magnetization is shown in the insert of Fig.47. It shows a satisfactory agreement to the Brillouin function of $gJ = 6$ with the spin number of 0.3 % per Yb atom.

Figure 48 shows the intrinsic magnetizations at various temperatures. The slope in the low field region agrees with the intrinsic magnetic susceptibility data given in Fig.45.

Figure 49 shows the isothermal magnetoresistance $\rho(H_0)$. A very large negative magnetoresistance is found at low temperatures. For example, the magnetoresistance at 1.3 K under 500 kOe is about one percent of the zero field value. This means that YbB_{12} undergoes a perfect metallic phase in high magnetic field. The observed phenomenon is quite unusual and it is interesting to see also in SmB_6 whether such a large magnetoresistance appears or not. We performed the similar magnetoresistance study on SmB_6 which is believed to have the semiconducting band gap of about 100 K. Figure 50 shows the magnetoresistance curve of SmB_6 polycrystalline sample. The observed magnetoresistance is very small compared with that of

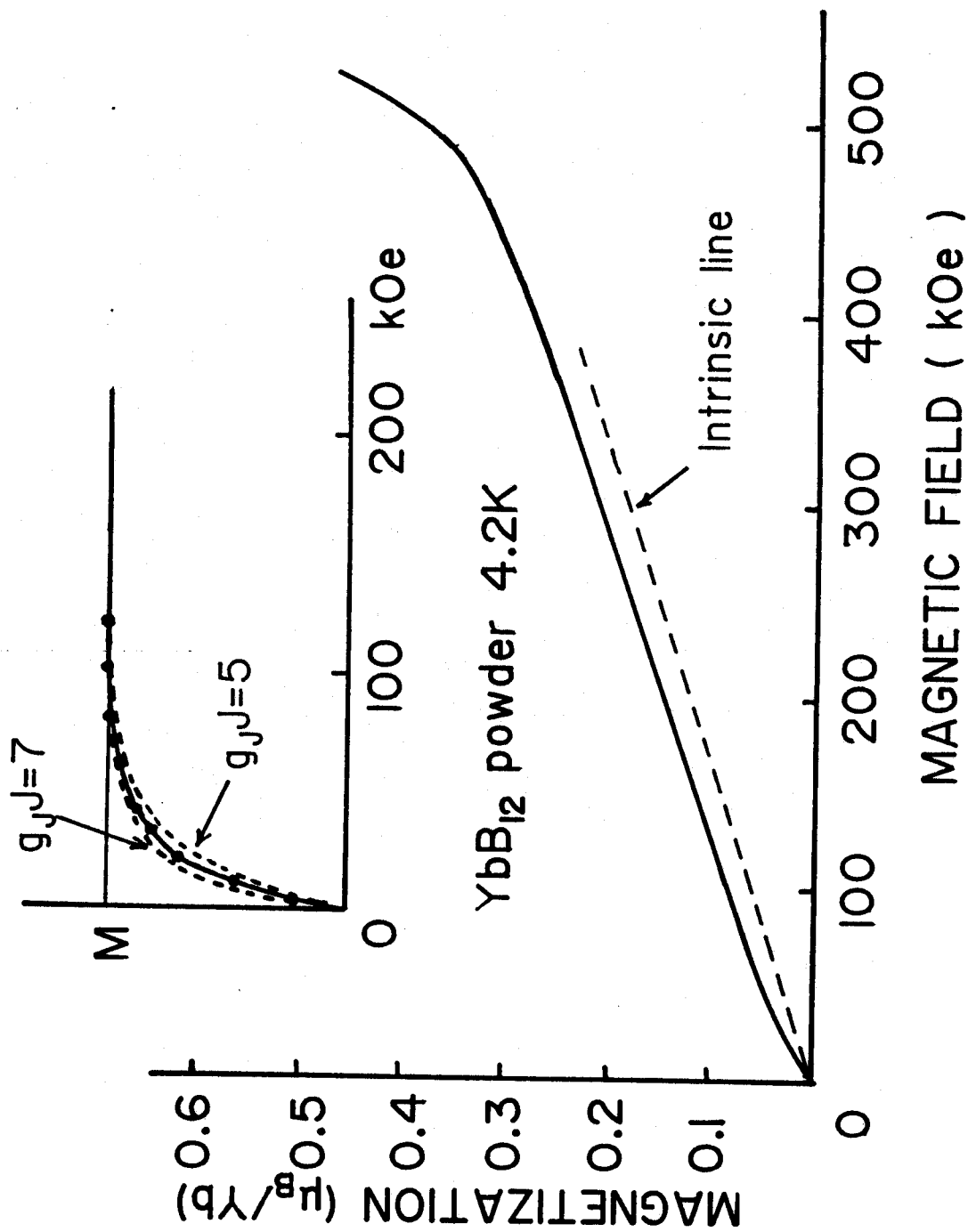


Fig. 47 Measured magnetization curve at 4.2 K. Insert shows the impurity magnetization. The calculated curves are shown by dotted lines with $gJ=7$ and $gJ=5$.

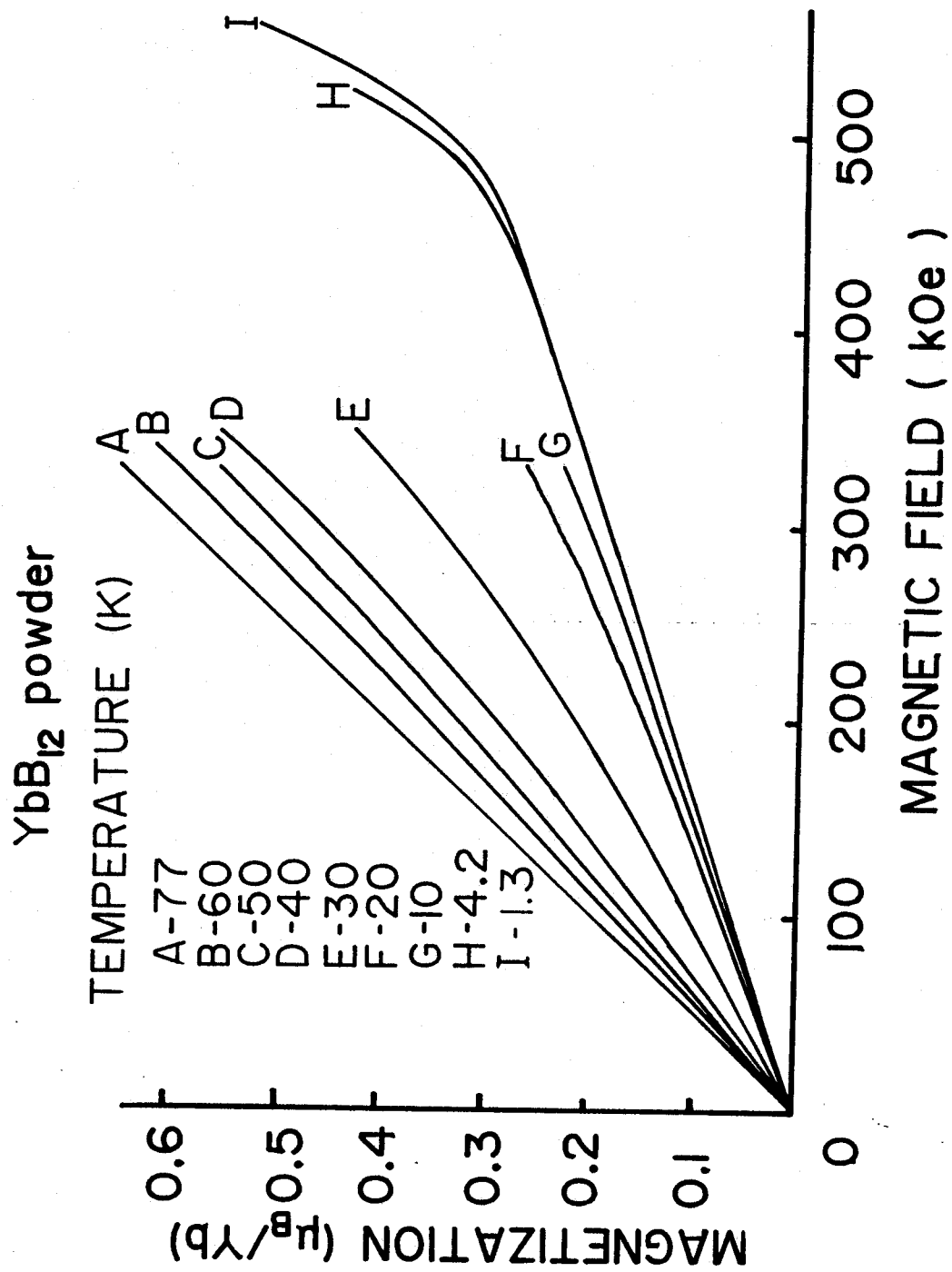


Fig.48 Obtained intrinsic magnetization curves at various temperatures.

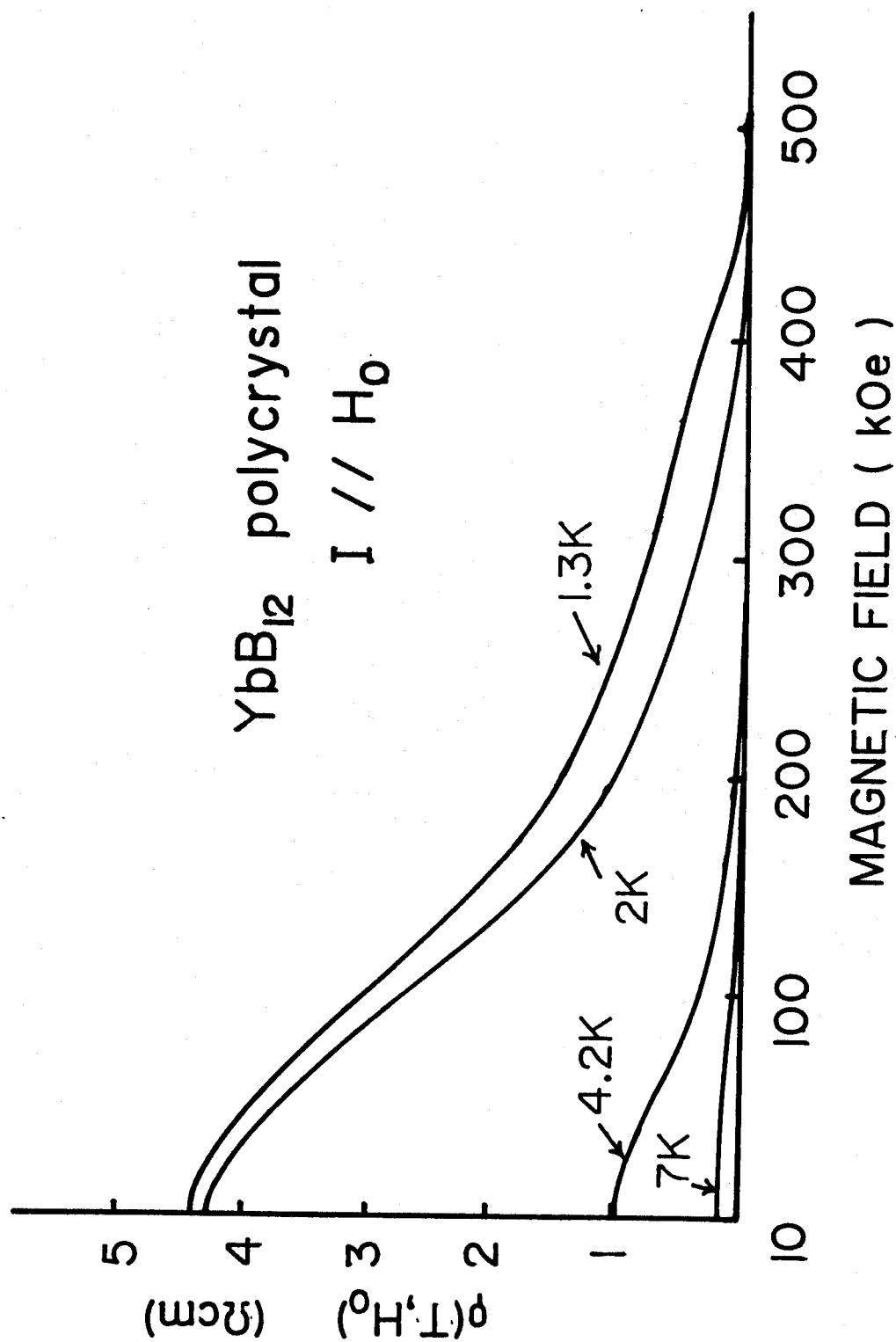


Fig. 49 magnetoresistance curves at various temperatures.

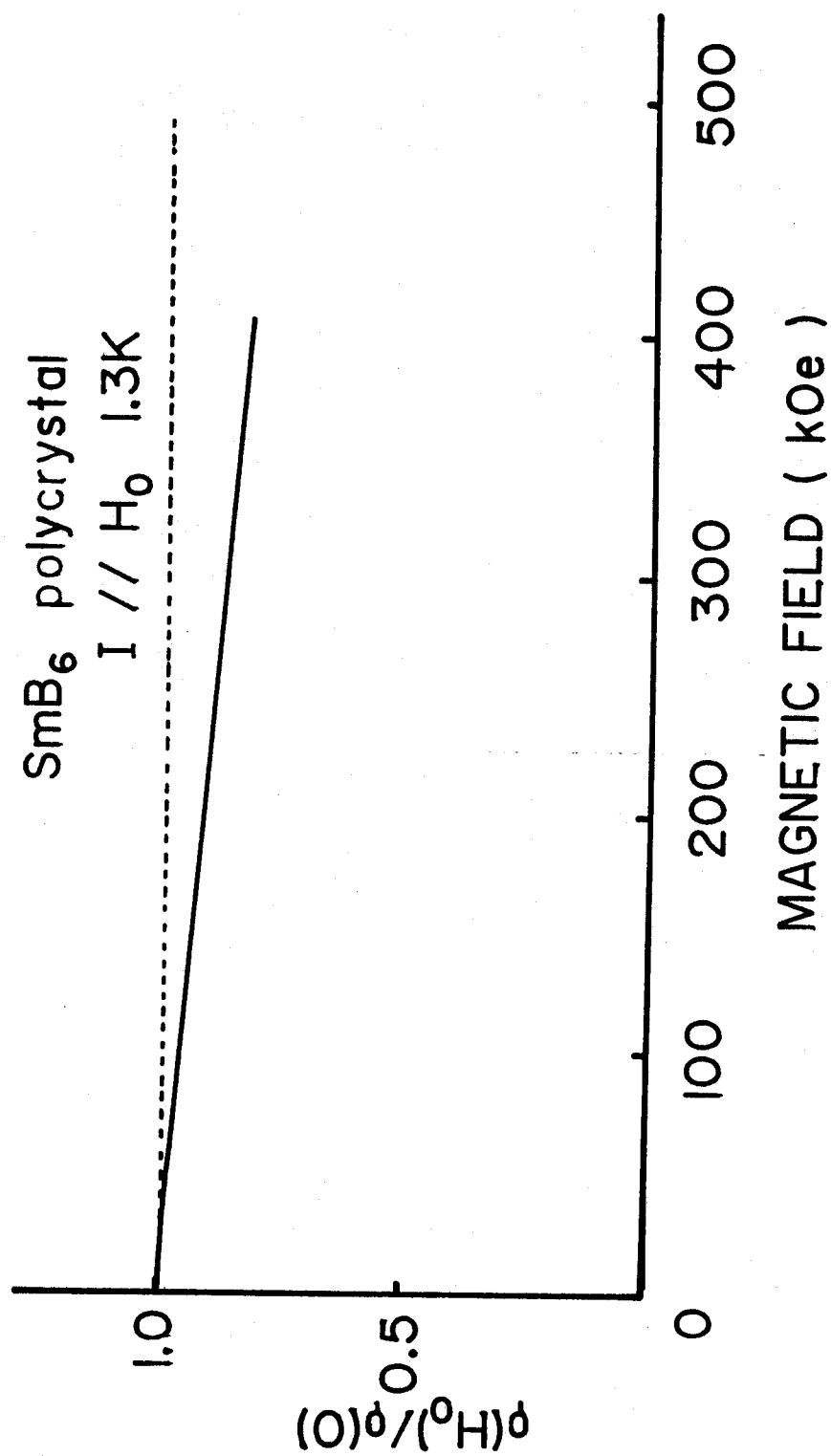


Fig. 5.0 Magnetoresistance of SmB₆ at 1.3 K.

YbB_{12} . The reason is discussed in the next section.

Magnetic field dependence of the observed ρ -T curve in YbB_{12} with the logarithmic plot is shown in Fig.51. It is clearly shown that the band gap energy of $2\Delta_1$ decreases with increasing magnetic field and the magnetic field dependence is given in Fig.52. The field dependence of Δ' is not clear because the pulse field measurement in the metallic region is not so precise.

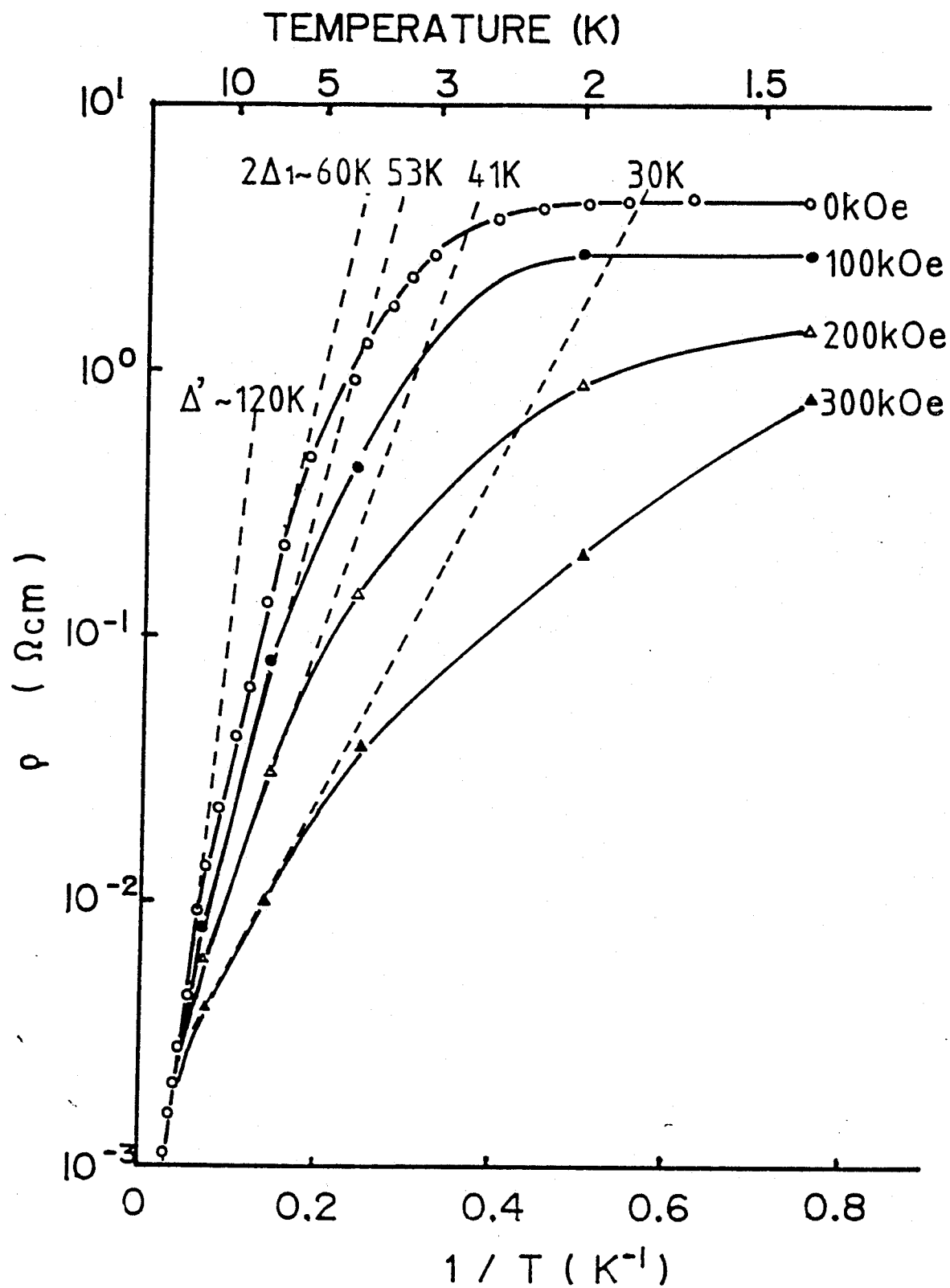


Fig.51 Magnetic field dependence of magnetoresistance ρ (T).

Dotted lines show the activation energy.

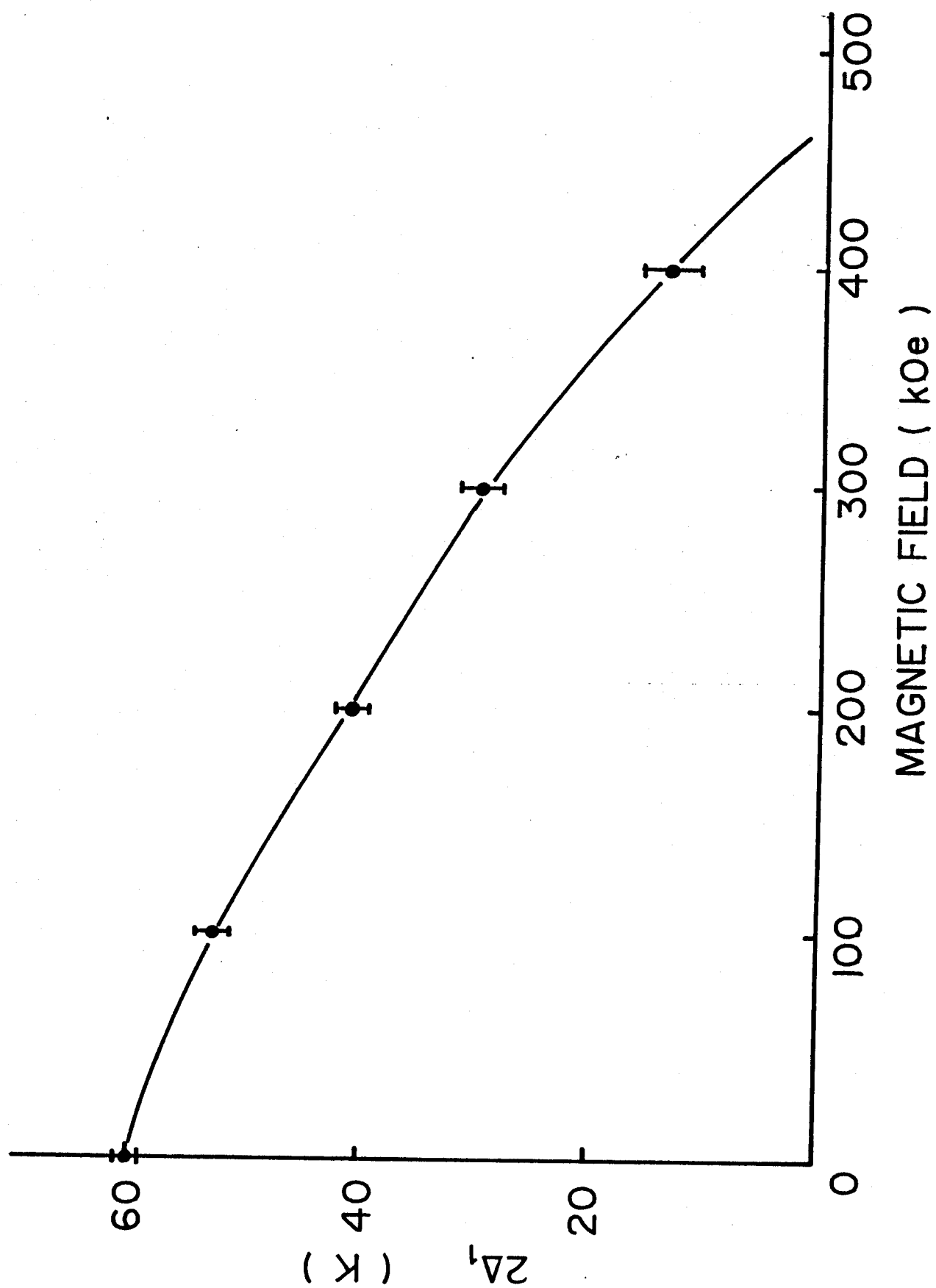


Fig.52 Magnetic field dependence of the energy gap $2\Delta_1$.

§ 5 FIELD-INDUCED METALLIC STATE AND THE MAGNETIZATION

Experimentally obtained metallic state and the related magnetization under high magnetic field is not explained by a simple hybridization model. One of the important experimental results is the presence of two activation energies as is shown in Fig.44. If the f- and conduction bands crosses as is schematically shown in Fig.53-(a), the hybridization effect mixes two bands and the band gap 2Δ appears. Accordingly, the expected density of state illustrated in Fig.53-(b) gives only one band gap or the activation energy. Experimentally speaking, however, two gaps $2\Delta_1$ and $2\Delta_2$ are necessary and one of the possible band scheme is shown in Fig.53-(c). Under zero magnetic field, the semiconductive electrical conductivity is expected by the gaps of $2\Delta_1$ and Δ' corresponding to the observed value of 60 K and 120 K, respectively. $2\Delta_2$ is obtained by the relation, $\Delta' = \Delta_1 + \Delta_2$ and it is 180 K. Although no information of the density of state above the Fermi energy E_F is given, it may be natural to consider a symmetric form with a mirror plane at E_F . Roughly speaking, the proposed band structure given in Fig.53-(c) means the mixing model of the f- and conduction electrons but the structure is not so simple as is seen in the standard hybridization model. Two large peaks corresponding to $2\Delta_2$ are considered to come mainly from the f-electron and gaps Δ_1 and Δ_2 would be zero if the level mixing interaction were absent. In other words, non-split f-level is assumed at E_F when no mixing interaction between the f- and conduction electrons exists.

When an external magnetic field is applied, the band gap Δ_1

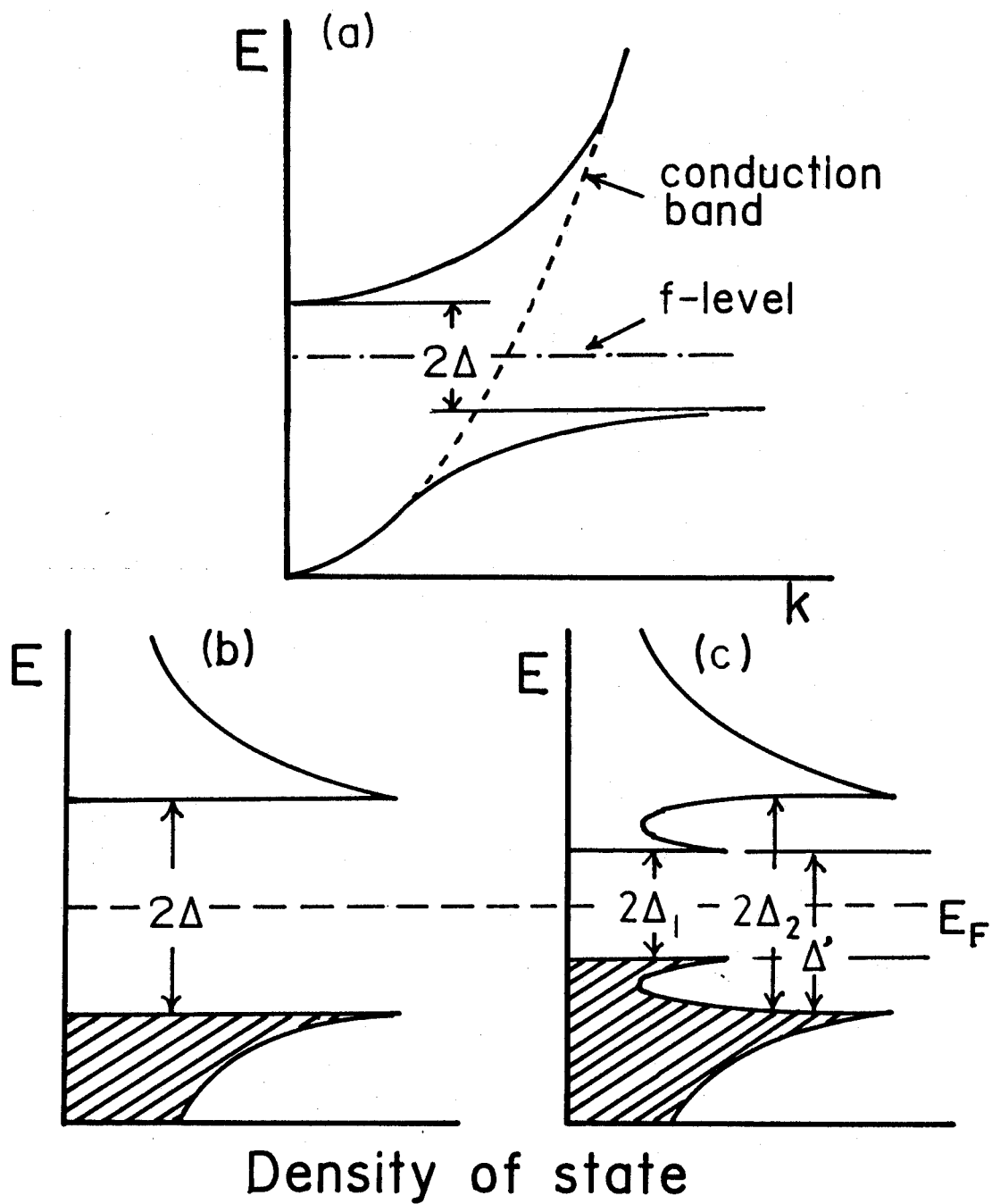


Fig.53 Schematic model of the band gap near E_F . (a) shows a simple mixing model with the band gap 2Δ and (b) is the corresponding density of state. (c) is the proposed model for YbB_{12} .

will be squeezed because the level mixing is broken by the field. This may correspond to the experimentally obtained band gap change as a function of magnetic field and it is empirically obtained as is shown by black points in Fig.54. The gap $2\Delta_1$ decreases nearly linearly with increasing magnetic field and the perfect quenching of the band gap is expected around 450 kOe. The observed increase in the magnetization around this field is explained as follows. Two peaks in the density of state with the gap of $2\Delta_2$ are field independent below about 400 kOe because the gap is determined by the mixing strength of the f- and conduction electrons. When the mixing energy becomes comparable to the Zeeman energy of the f-electron under high magnetic field, the f-level becomes field dependent as is shown in Fig.54 and the linear Zeeman effect may be expected at enough high magnetic fields.

The expected whole magnetization curve is drawn in Fig.55 where the magnetic moment consists of two parts. One of them is the Van Vleck term which is evaluated by the low field magnetization. The main magnetization comes from the f-electron polarization between H_{c1} and H_{c2} . The increasing ratio of the magnetization can be evaluated from the curve-I in Fig.48 using value of the tangent χ around 550 kOe. If the linear magnetization is assumed between H_{c1} and H_{c2} , H_{c1} is estimated to be 520 kOe and H_{c2} and the gJ-value of the f-electron can be determined in the following way. Magnetization M is given by differentiating the free energy U by magnetic field so that the linear magnetization between H_{c1} and H_{c2} is expressed by the relation,

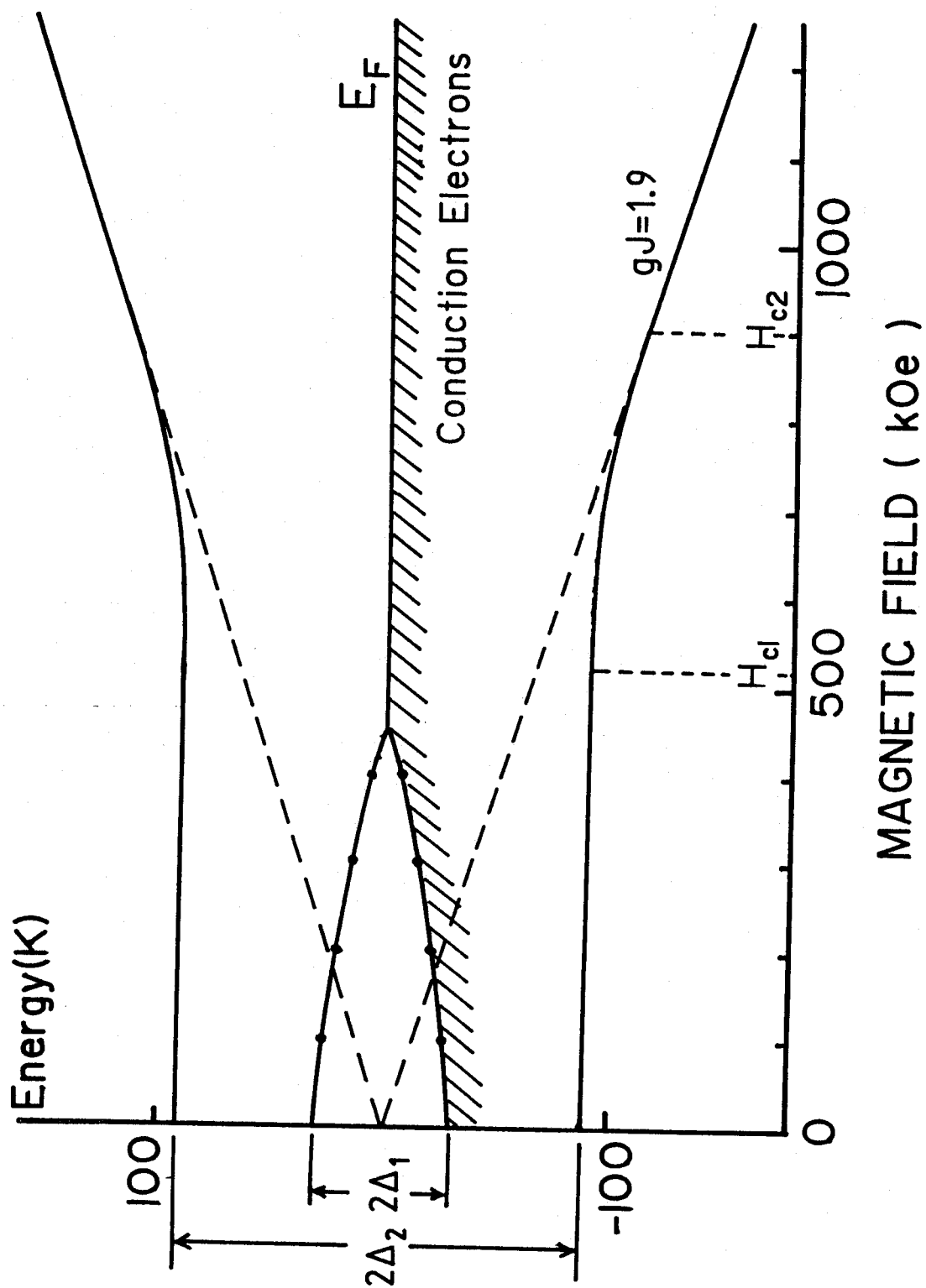


Fig.54 Semiempirical band model of YbB_{12} under magnetic field.

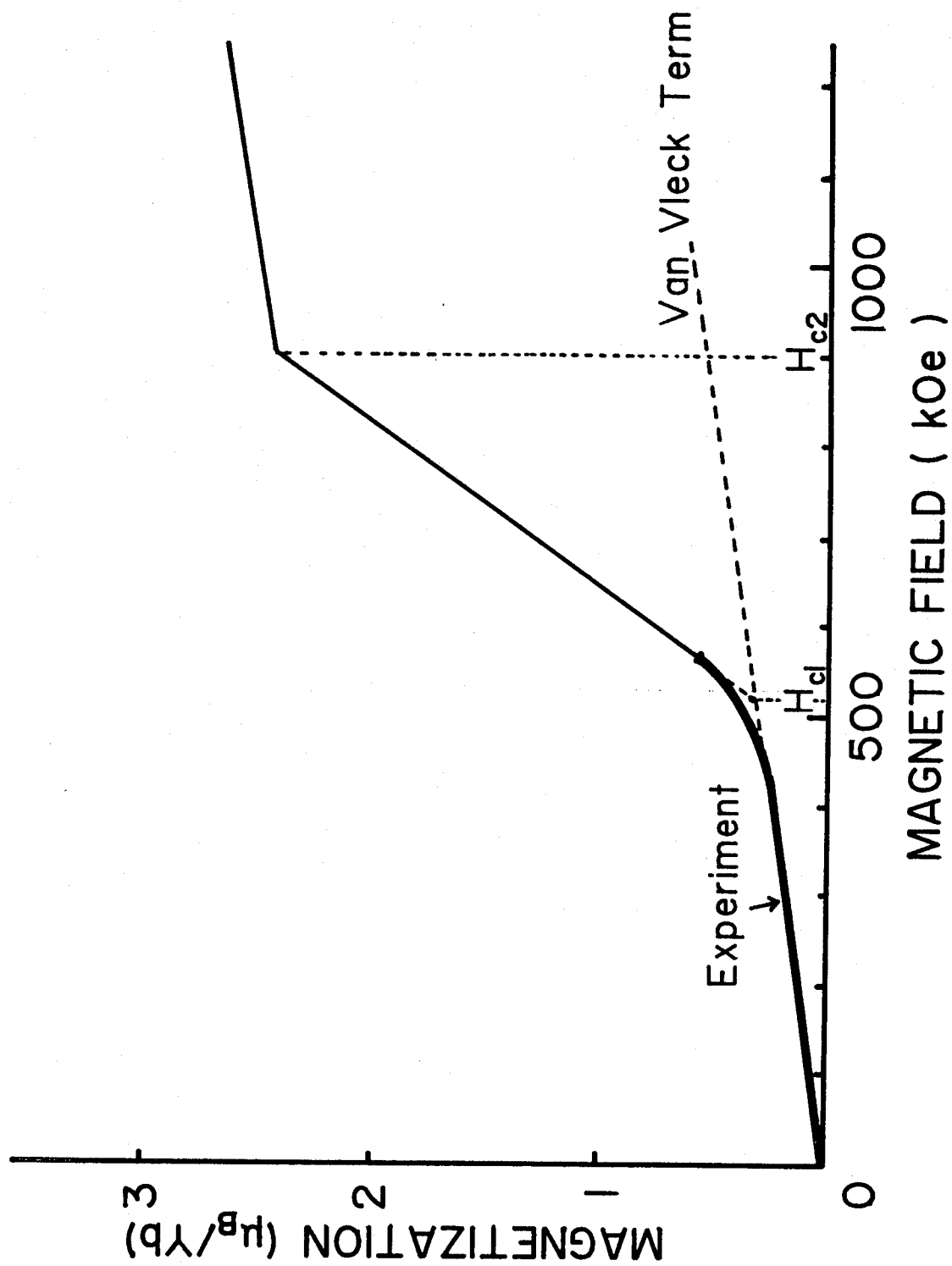


Fig.55 Magnetization curve of YbB_{12} . Thick line shows the experimental datum.

$$M = -\partial U / \partial H_0 = \chi (H_0 - H_{c1}), \quad (5.1)$$

where χ is the magnetic susceptibility in this region. The free energy is obtained as

$$U = -\Delta_2 - (\chi/2)(H_0 - H_{c1})^2, \quad (5.2)$$

where the free energy at H_{c1} is $-\Delta_2$ as is seen in Fig.54. The free energy above H_{c2} is given by

$$U = -g\mu_B J H_0. \quad (5.3)$$

It is noted that (5.2) and (5.3) should be equal at H_{c2} and $\partial U / \partial H_0$ should also be equal because of the continuity condition in the magnetization. Therefore, the following two equations are obtained as

$$gJ\mu_B H_{c2} = \Delta_2 + (\chi/2)(H_{c2} - H_{c1})^2, \quad (5.4)$$

$$gJ\mu_B = \chi(H_{c2} - H_{c1}). \quad (5.5)$$

gJ and H_{c2} are obtained from eqs.(5.4) and (5.5) as

$$H_{c2} = \sqrt{2\Delta_2/\chi + H_{c1}^2}, \quad (5.6)$$

$$gJ = \chi/\mu_B \{ \sqrt{2\Delta_2/\chi + H_{c1}^2} - H_{c1} \}, \quad (5.7)$$

The experimentally obtained values of Δ_2 , χ and H_{c1} are

$$\left. \begin{aligned} \Delta_2 &= 90 \text{ K} , \\ \chi &= 0.5\mu_B \times 10^{-5} / \text{Oe} , \\ H_{c1} &= 520 \text{ kOe} . \end{aligned} \right\} \quad (5.8)$$

Inserting these values into eqs.(5.6) and (5.7), H_{c2} and gJ are obtained as

$$H_{c2} = 900 \text{ kOe} , \quad (5.9)$$

$$gJ = 1.9 . \quad (5.10)$$

The magnetic saturation of the f-electron moment is expected above about 900 kOe although the accuracy of H_{c2} is not so high because it is an extrapolated value assuming the linear magnetization.

Thus, the electric and magnetic properties of YbB_{12} is semiempirically explained by the proposed band model. The responsible f-level near E_F may be the Γ_8 -level because the gJ -value is close to 2. However, the possibility of the Γ_7 state is not eliminated because the gJ -value is 1.7 which is not so far from our datum.

The similar band model may be applicable to SmB_6 but the field effect on the resistivity is very small as is shown in Fig.50. This may be due to the fact that the gJ -value of 0.476 for the ground state of SmB_6 ¹⁵⁾ is small compared with that in YbB_{12} . As is seen from Fig.50, the resistivity of SmB_6 in 1.3 K at 400 kOe is about 85 % of the zero field value and the corresponding decrease is found at about 70 kOe in YbB_{12} as is seen in Fig.49. Assuming the similar band gap, ratio of gJ -value may be about $70/400 \approx 0.18$ which is nearly equal to the expected value of $0.476/1.9 \approx 0.25$. Therefore, the difference between SmB_6 and YbB_{12} may come from the difference of the gJ -value.

REFERENCES

- 1) F. Bertaut and P. Blum: CR Acad. Sci. 34 (1949) 666.
- 2) M. Kasaya, F. Iga, K. Negishi, S. Nakai and T. Kasuya: J. Magn. & Magn. Mat. 31-34 (1983) 437.
- 3) M. Kasaya, F. Iga, M. Takigawa and T. Kasuya: J. Magn. & Magn. Mat. 47-48 (1985) 429.
- 4) F. Iga, Y. Takakuwa, T. Takajashi, M. Kasaya and T. Kasuya: Solid state Commun. 50 (1984) 903.
- 5) M. Moser, P. Wachter, F. Hulliger and J. R. Etourneau: Solid state Commun 54 (1985) 241.
- 6) N. F. Mott: Phil. Mag. 30 (1973) 403.
- 7) T. Kasuya, K. Takegahara, T. Fujita, T. Tanaka and E. Bannai: J. Physique 40 (1979) C5-308.
- 8) K. Sugiyama, A. Ohya, M. Date, F. Iga, M. Kasaya and T. Kasuya: J. Magn. & Magn. Mat. 52 (1985) 283.
- 9) B. Post: in Boron, Metallo-Boron Compounds, Boranes, eds. R. M. Adame (Interscience, New York, 1964) p.301.
- 10) H. Harima, A. Yanase and T. Kasuya: J. Magn. & Magn. Mat. 47-48 (1985) 567.
- 11) A. Yamagishi and M. Date: High Field Magnetism, ed. M. Date (North-Holland, Amsterdam, 1982) p.289.
- 12) K. Okuda and M. Date: J. Phys. Soc. Jpn. 27 (1969) 839.
- 13) H. Mollmotto, M. Motokawa and M. Date: J. Phys. Soc. Jpn 49 (1980) 108.
- 14) T. Sakakibara, H. Mollmotto, M. Motokawa and M. Date: High Field Magnetism, ed. M. Date (North-Holland, Amsterdam, 1982) p.299.

- 15) T. Uemura, Y. Chiba, M. Hagiwara and M. Date: J. Phys. Soc.
Jpn. 55 (1986) 3737.

PART II - C -

HIGH FIELD PROPERTIES OF HIGH- T_C SUPERCONDUCTORS

ABSTRACT

The first report on the whole profile of the H_{c2} - T curve in the superconducting 123-compound is presented. The data have been obtained from $\text{EuBa}_2\text{Cu}_3\text{O}_y$ single crystal under a pulsed magnetic field up to 500 kOe along the c -axis. H_{c2} at 4.2 K is 275 ± 25 kOe for the onset of the resistivity and is about 350 kOe when the mid-point of the resistivity is plotted. The residual resistivity is estimated to be $55 \mu\Omega\text{cm}$. The magnetoresistance is positive and the general features of the superconducting properties except T_C are well sketched by the BCS dirty limit model. The anisotropy in H_{c2} is also measured with several 123-compounds. It is found that the H_{c2} anisotropy is nearly equal to the reciprocal of the H_{c1} anisotropy in accord with the anisotropic GL-theory.

§ 1 INTRODUCTION

It is generally accepted that high magnetic field study in high- T_c superconductors^{1),2)} will give much information about the intrinsic properties of the transport phenomena. In practice, however, the study has been considered to be difficult because the expected $H_{c2}(T)$ near 0 K is very high and much work has been done without looking at the whole profile of the H_{c2} - T curve. The experimental studies for single crystals³⁾⁻⁹⁾ and sintered powder samples¹⁰⁾⁻¹²⁾ show only the extrapolated H_{c2} and resistivity curves based on data near T_c . As the present status of electronic band calculations^{13),14)} and various theories¹⁵⁾ do not give a sufficient explanation of the intrinsic mechanism of high- T_c superconductivity, it is highly desirable to have complete information about the electrical and magnetic responses of high T_c superconducting materials.

The present paper gives the first report on the whole profile of the H_{c2} - T curve and the residual resistivity of 123-compound. The experiment has been performed using $\text{EuBa}_2\text{Cu}_3\text{O}_y$ single crystal under a pulsed magnetic field up to 500 kOe down to liquid helium temperature. A clear change from the superconducting state is found even at 4.2 K when the magnetic field is applied along the c-axis. The on-set of resistivity appears at 275 kOe and approaches saturation at around 500 kOe. Then, the coherent length ξ is determined with high accuracy and one can also check the validity of the WHH theory and the anisotropic GL-theory in the 123-compounds.

§ 2 CRYSTAL STRUCTURE OF 123-COMPOUNDS AND THE SUPERCONDUCTING PROPERTIES

Since the superconductivity near 30 K was found by Bednorz and Muller,¹⁾ extensive studies have concentrated on the search of new high T_c superconducting metal oxide materials. The first superconducting material with T_c above liquid-nitrogen temperature was discovered in mixed-phase Y-Ba-Cu-O system by Wu et al.,²⁾ and Hikami et al.,¹⁶⁾ and the high T_c phase was identified with $\text{YBa}_2\text{Cu}_3\text{O}_y$ by several groups independently.¹⁷⁾⁻¹⁹⁾ Furthermore, high T_c above 90 K was also observed in a series of Re-Ba-Cu-O compounds where Y in $\text{YBa}_2\text{Cu}_3\text{O}_y$ is replaced by Rare-earth elements Re.²⁰⁾

The compounds are recently called as 123-compounds and y is usually between 6.5 and 7. The 123-compounds have an orthorhombic layered perovskite structure²¹⁾ as is shown in Fig.56. The lattice parameters are determined to be $a = 3.88 \text{ \AA}$, $b = 3.82 \text{ \AA}$ and $c = 11.69 \text{ \AA}$ for $\text{YBa}_2\text{Cu}_3\text{O}_y$.²¹⁾ The structure indicates that the transport properties of the 123-compounds may be anisotropic and upper critical fields H_{c2} with a large anisotropy between a- and c- axes are found by several single crystal experiment. The single crystal has the twin boundaries in the c-plane which is found by the black and white lines at 45° to the a- and b- axes in the polarized optical microscope photograph.⁸⁾

It is well known that the superconducting properties of these metal oxides strongly depend on the oxygen content. The variation of the oxygen content determines the electrical properties, ranging from insulating, semiconducting, metallic to

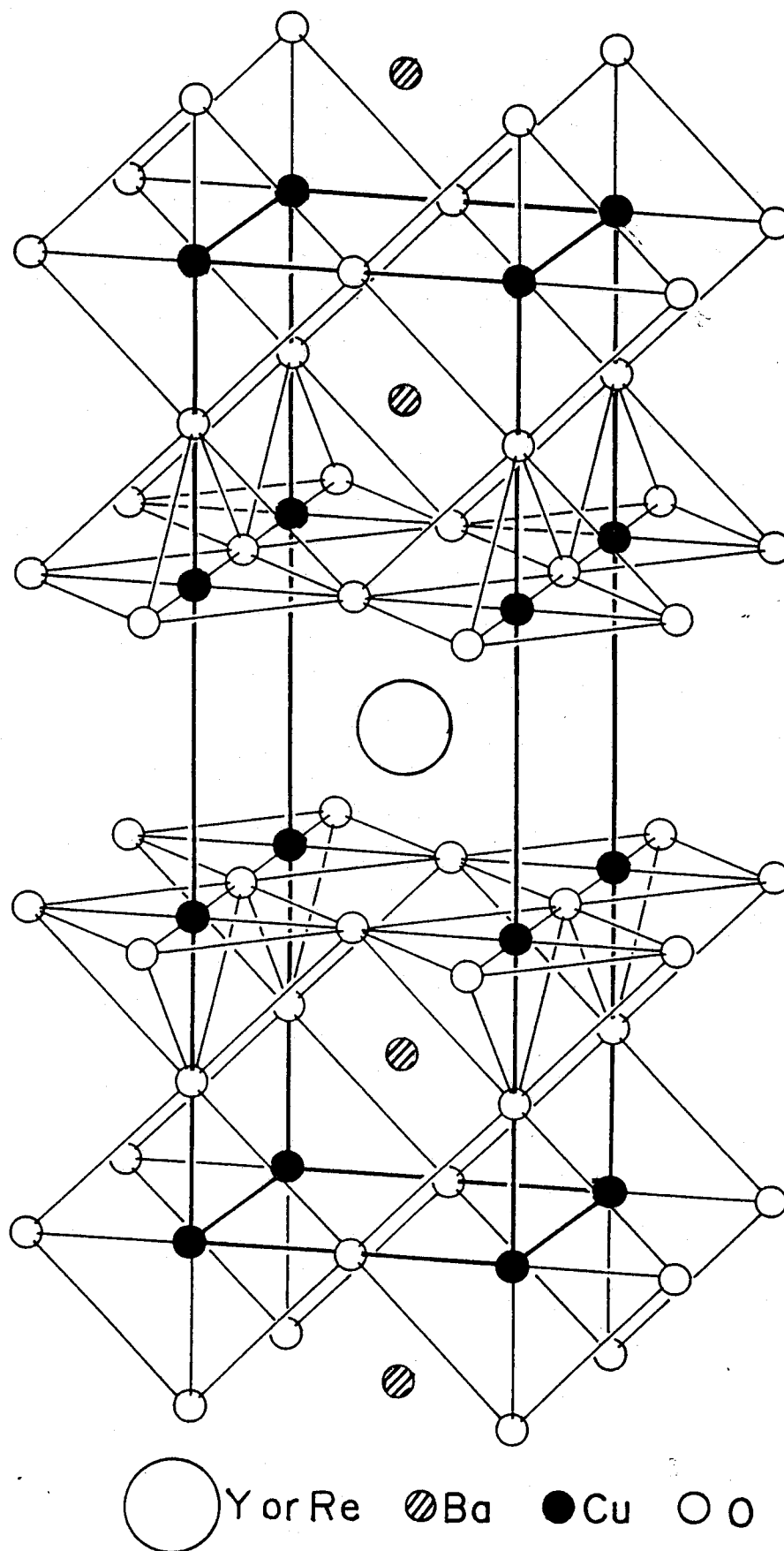


Fig. 56. Crystal structure of 123-compound.

superconducting state. The insulating and semiconducting materials have tetragonal layered perovskite structure and they are out of present interest.

§ 3 EXPERIMENTAL PROCEDURE

$\text{EuBa}_2\text{Cu}_3\text{O}_y$ single crystal with a mean size of $1100 \times 560 \times 22 \mu\text{m}^3$ were prepared by Hikita group, NTT, Opto-electronic Laboratory. The specimens were grown from molten Eu-Ba-Cu-O compounds.^{22),23)} As-grown crystals were annealed in an oxygen atmosphere at $900\sim 950^\circ\text{C}$ for $5\sim 10$ hours and then cooled down slowly to room temperature. Annealed crystals show a twinning structure as is mentioned in section 2. The largest facet is the c-plane which is perpendicular to the c-axis. Sample resistivity was measured using the usual four-terminal method. The good electrical contact was obtained by the NTT group, using gold wires of $25 \mu\text{m}$ in diameter with silver paste on the gold films evaporated on the largest facet of the crystal. Contact resistances were between 10^{-2} and $10^{-1} \Omega\text{mm}^2$ for the area of $560 \times 170 \mu\text{m}^2$. Method of I- and V- terminal connections is shown in Fig.57. The measured temperature dependence of the electrical resistivity in the c-plane is shown in Fig.58. A highly qualified single crystal of $\text{EuBa}_2\text{Cu}_3\text{O}_y$ with a superconducting transition temperature of 94 K was obtained and the transition width was within 1 K.

The magnetoresistance was measured by using the DC four-terminal method in a temperature range from 4.2 K to room temperature under a pulsed magnetic field up to 500 kOe at the Research Center for Extreme Materials in Osaka University where the sample temperature was measured with a calibrated thermocouple of Au-Fe/Ag. The pulsed width of the magnetic field was 0.4 msec. The details of the magnetoresistance measurement

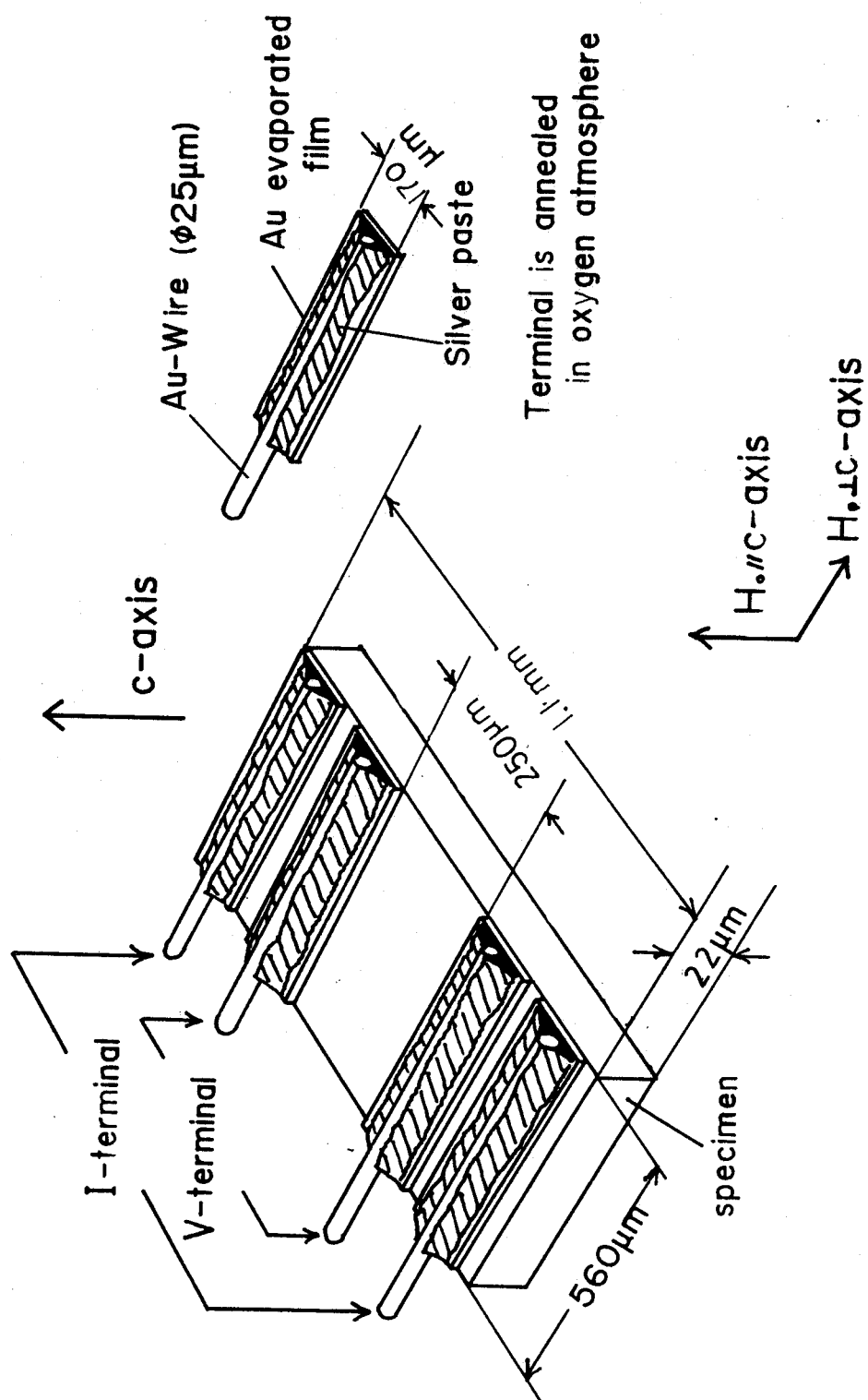


Fig. 57. Electrical junction of I- and V-terminals on single crystal of $\text{EuBa}_2\text{Cu}_3\text{O}_y$.

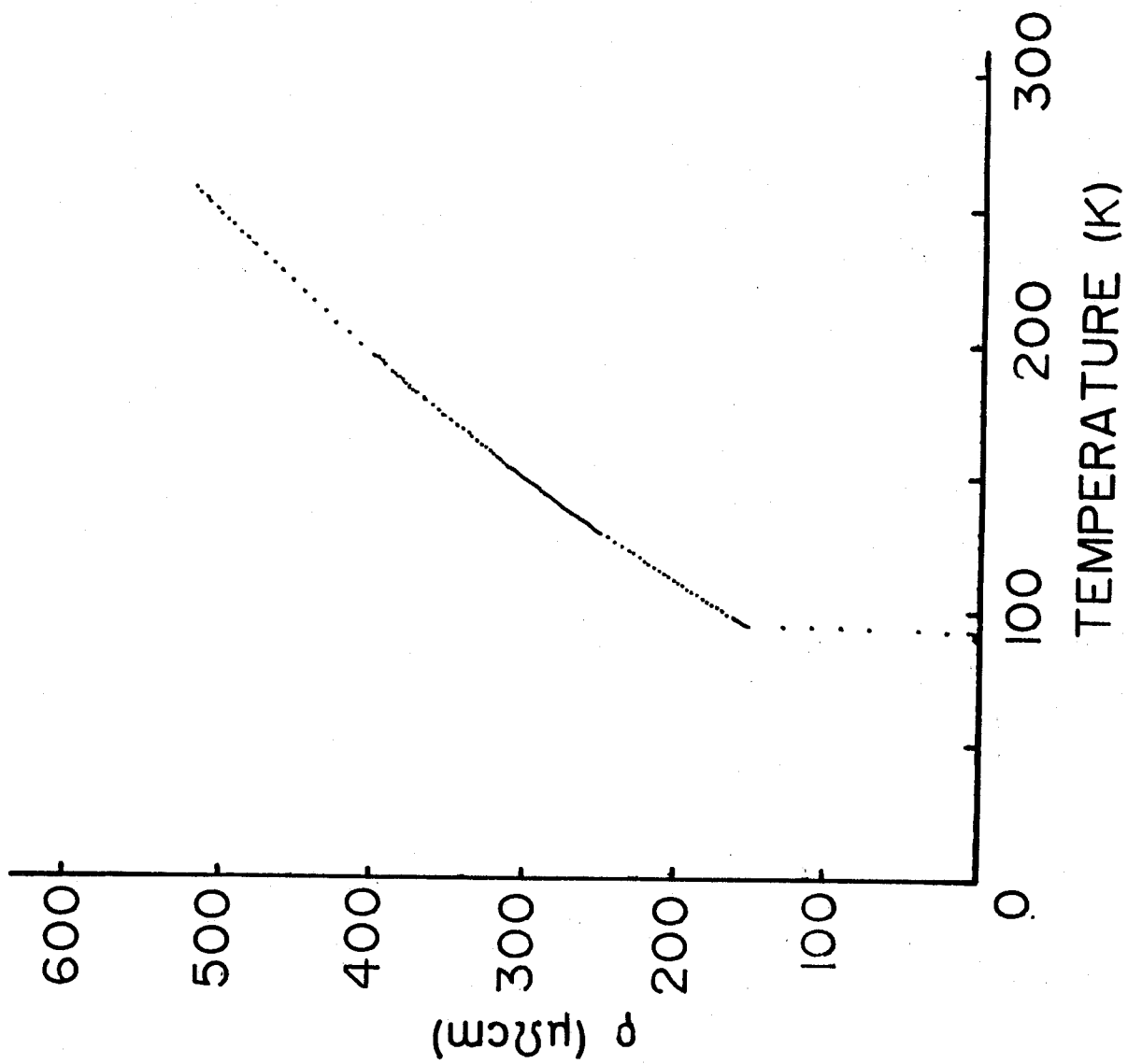


Fig. 58. Temperature dependence of the electrical resistivity in the c-plane of $\text{EuBa}_2\text{Cu}_3\text{O}_{7-x}$.

under pulsed magnetic field are similar to that of part II -B-.
Therefore, it is not shown here.

§ 4 UPPER CRITICAL FIELD H_{c2} AND NORMAL RESISTIVITY

Magnetic field dependence of the parallel resistance in the c-plane with the magnetic field H_0 along the c-axis from 310 K to 4.2 K is shown in Fig.59. The magnetoresistance MR_{\perp} defined by $\rho_{\parallel}(T, H_0) - \rho_{\parallel}(T, 0)$ is positive and is approximately linear up to 500 kOe in the temperature range above T_c . Figure 60 shows the corresponding ρ_{\parallel} when H_0 is parallel to the c-plane. The magnetoresistance in this case, MR_{\parallel} , is slightly smaller than MR_{\perp} . However, the negative magnetoresistance observed by Oussena et al. in sintered powder $YBa_2Cu_3O_{y^{12)}}$ sample was not found in this experiment.

Figure 61 shows the temperature dependence of $H_{c2\perp}(T)$ and $H_{c2\parallel}(T)$ obtained from Figs.59 and 60 where \perp and \parallel represent the magnetic field direction referred to the c-plane. The $H_{c2}(\rho = 0)$ and $H_{c2}(\rho = 1/2)$ are defined as magnetic field at the on-set point of the resistance and at half of the normal resistivity ρ_n shown by notations A and B, respectively in Fig.60. The $H_{c2\perp}(T)$ curve exhibits a slightly upward curvature near T_c which is very often observed in layered superconductors.^{24),25)} The value of $H_{c2\perp}(0)$ is estimated to be 275 ± 25 kOe. This value is close to 265 kOe which is evaluated by the WHH theory, i.e. the dirty-limit BCS relation of $H_{c2}(0) = 0.69T_c(dH_{c2}/dT)^{26)}$ with the observed $dH_{c2\perp}/dT$ of 4.1 kOe/K. This means that the WHH theory is effective in the case of this 123-compound. On the other hand, $H_{c2\parallel}(T)$ drastically increases with decreasing temperature and is measured only above 79 K. The extrapolated $H_{c2\parallel}(0)$ using the same relation is 2450 ± 200 kOe where $dH_{c2\parallel}/dT$ is 38 kOe/K

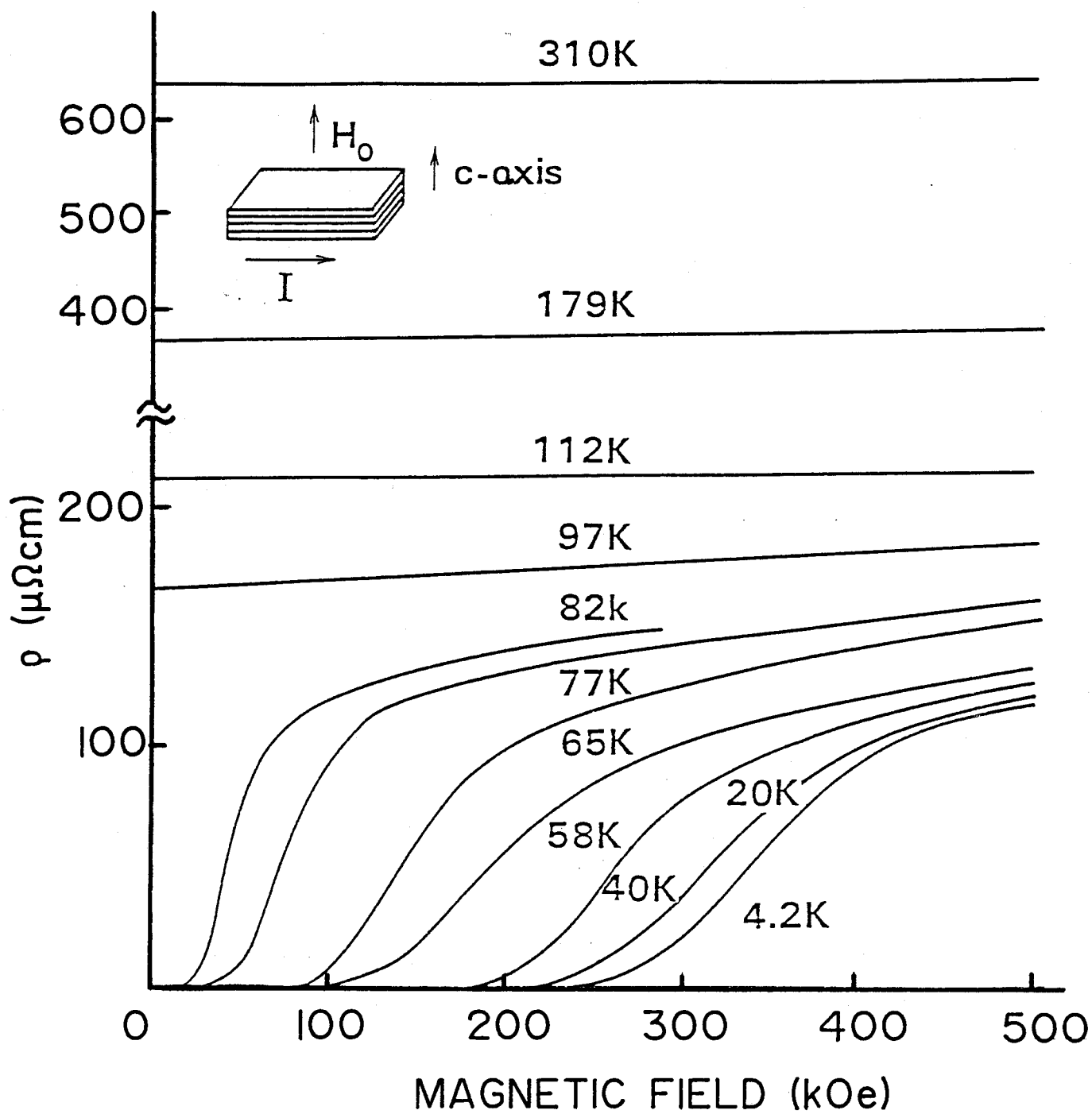


Fig. 59. Temperature dependence of the magnetoresistance
in $\text{EuBa}_2\text{Cu}_3\text{O}_y$ ($H_0 \perp c\text{-plane}$).

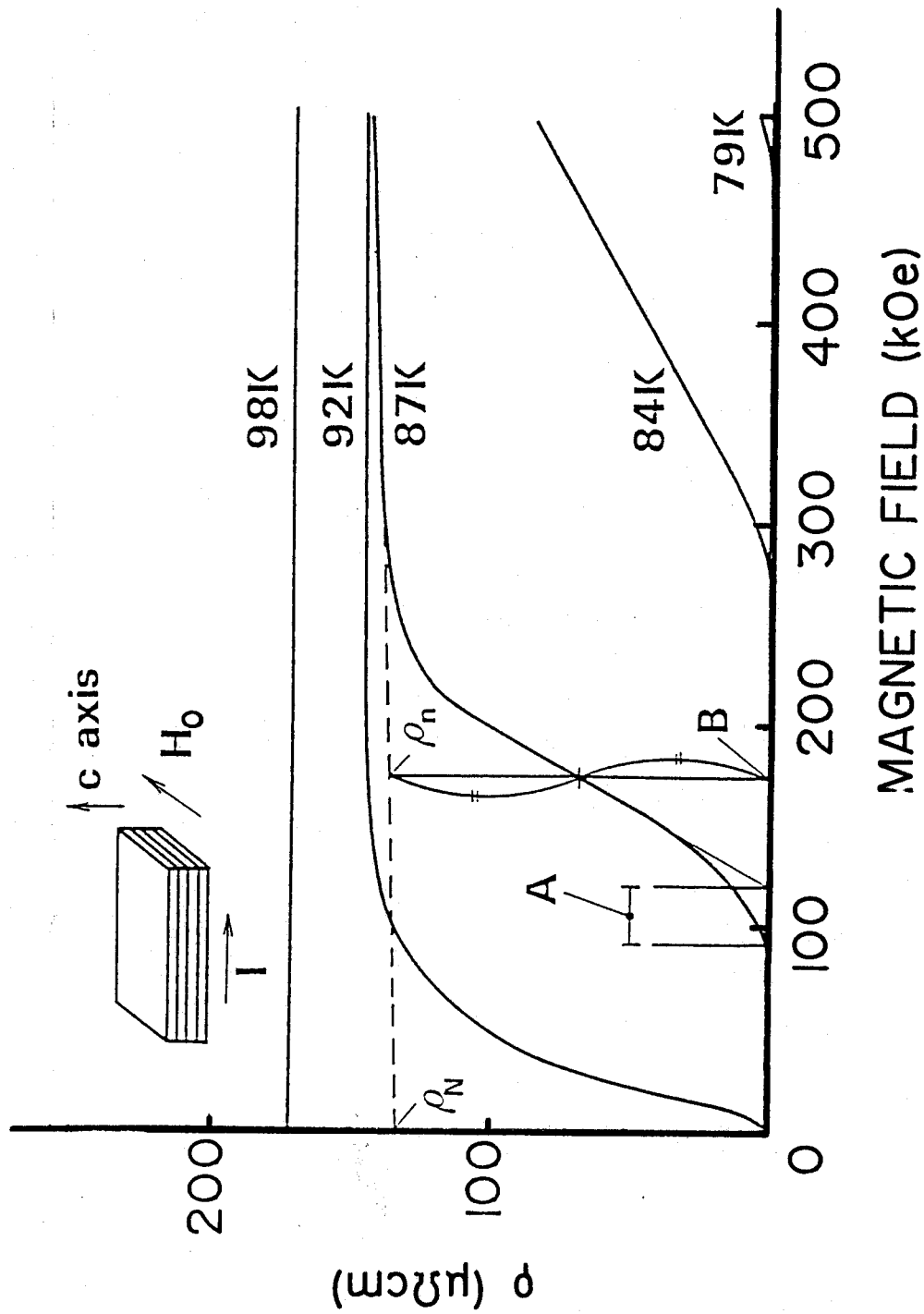


Fig. 60. Temperature dependence of the magnetoresistance in $\text{EuBa}_2\text{Cu}_3\text{O}_y$ ($H_0 \parallel c$ -plane). Definitions of the on-set point A and mid-point B are schematically shown. ρ_N is the extrapolated point.

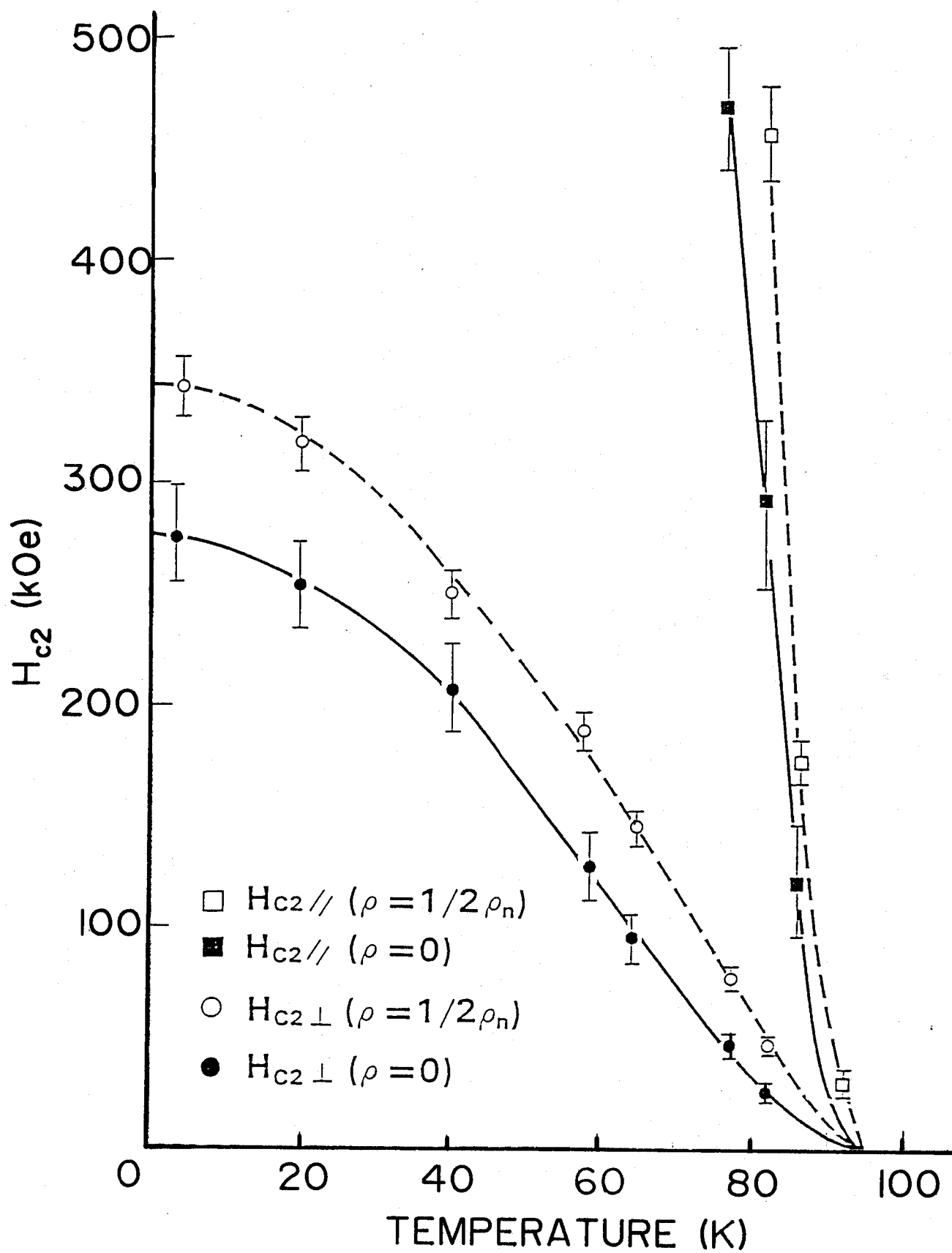


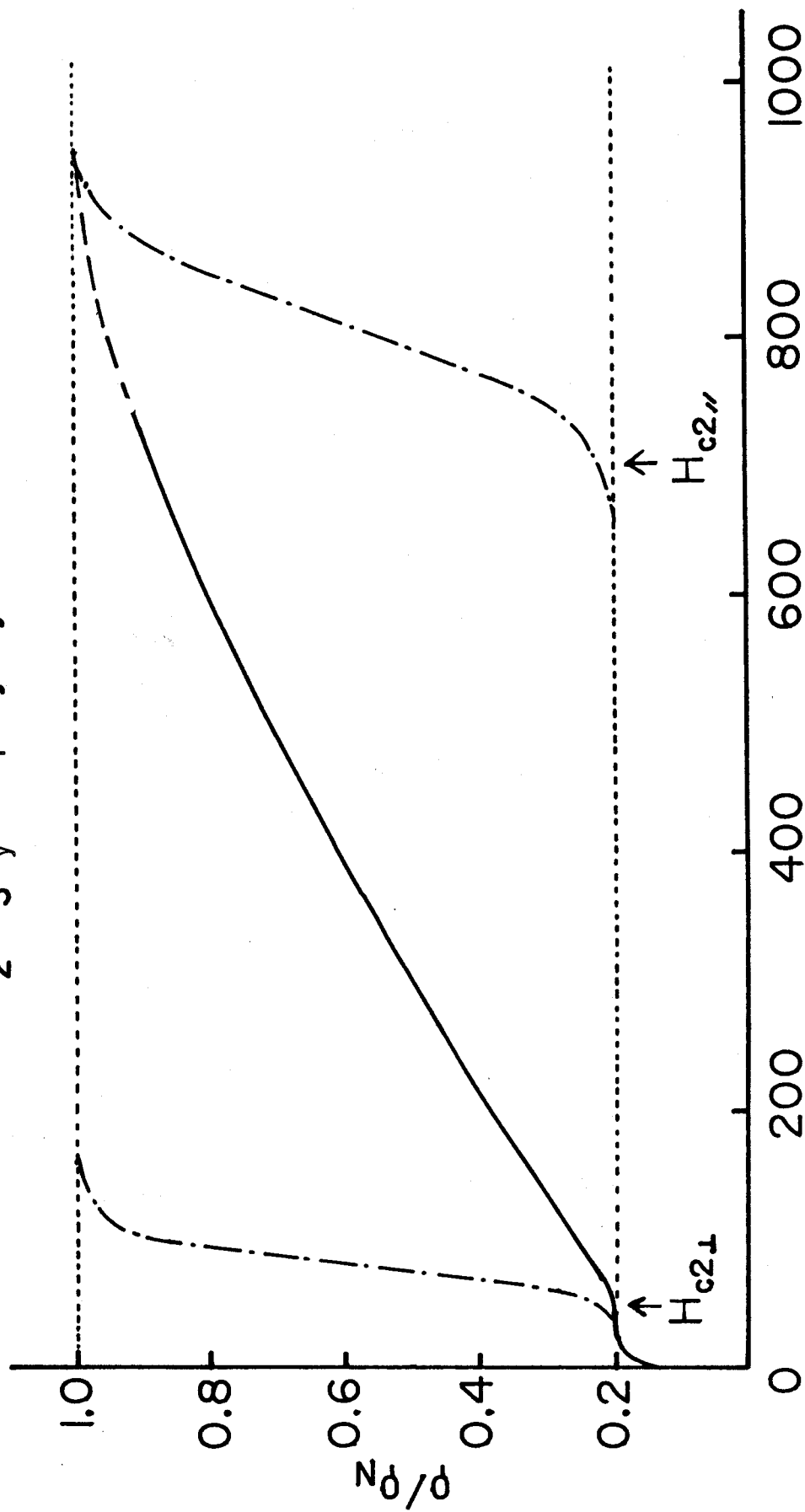
Fig. 61. Temperature dependence of H_{c2} in $\text{EuBa}_2\text{Cu}_3\text{O}_y$.

around $T/T_c = 0.8 \approx 0.9$. The $H_{c2} \parallel (T)$ also exhibits upward curvature near T_c .

$H_{c2 \perp}$ and $H_{c2 \parallel}$ are obtained not only from single crystal measurement but also from sintered polycrystalline measurement. Fig.62 shows the magnetoresistance of sintered $YBa_2Cu_3O_y$ at 77 K up to 750 kOe obtained by 3-layer magnet where ρ_N is given by extrapolation of the ρ -T curve. Consider the magnetoresistance curve of polycrystalline material. This curve shows the superconducting state below $H_{c2 \perp}$ because this field is the lowest transition field for all directions. The resistivity between $H_{c2 \perp}$ and $H_{c2 \parallel}$ changes gradually and the normal value is obtained at $H_{c2 \parallel}$ where all parts of the polycrystalline material are in the normal state. Accordingly, $H_{c2 \perp}$ is obtained from the onset point of the polycrystalline curve and $H_{c2 \parallel}$ can be estimated from the onset point of the perfectly normal state. This method is shown in Fig.62 where the transition width is treated in the following way. The transition width between the normal state and superconducting states becomes large as the transition field H_{c2} increases as is shown in Fig.63. These data are used to determine $H_{c2 \parallel}$ in Fig.62. The resistivity below 0.2 comes from the breaking of Josephson bridge between the crystal grains in the powdered material.

Figures 64 and 65 show the obtained $H_{c2 \parallel}$ and $H_{c2 \perp}$ for various 123-compounds. In Fig.64, a good agreement is obtained for $YBa_2Cu_3O_y$ compound data of ISSP but the IBM-data are lower than our data. This may be explained by the assumption that the purity of IBM sample is better than ours and also ISSP's sample because good sample usually shows low H_{c2} value. The obtained

YBa₂Cu₃O_y polycrystal 77K



MAGNETIC FIELD (kOe)

Fig. 62. Magnetoreistance of polycrystalline YBa₂Cu₃O_y at 77K.

Dash-dotted lines show the estimated magnetoresistances of H_0 and H_0 plane assuming the similar transition width of EuBa₂Cu₄O_v.

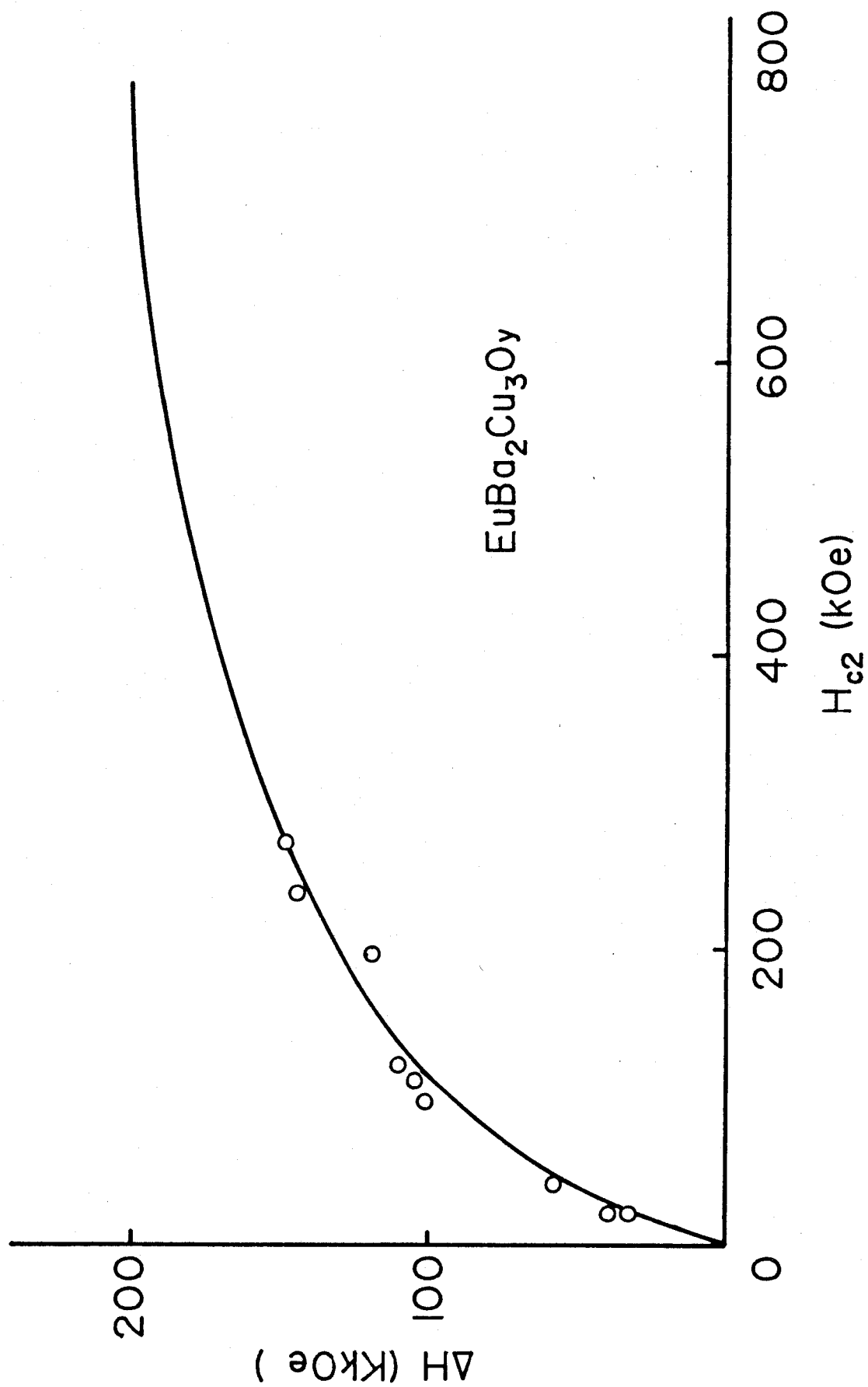


Fig. 63. Empirical field dependence of transition width ΔH of H_{c2} in $\text{EuBa}_2\text{Cu}_3\text{O}_y$.

Fig. 63

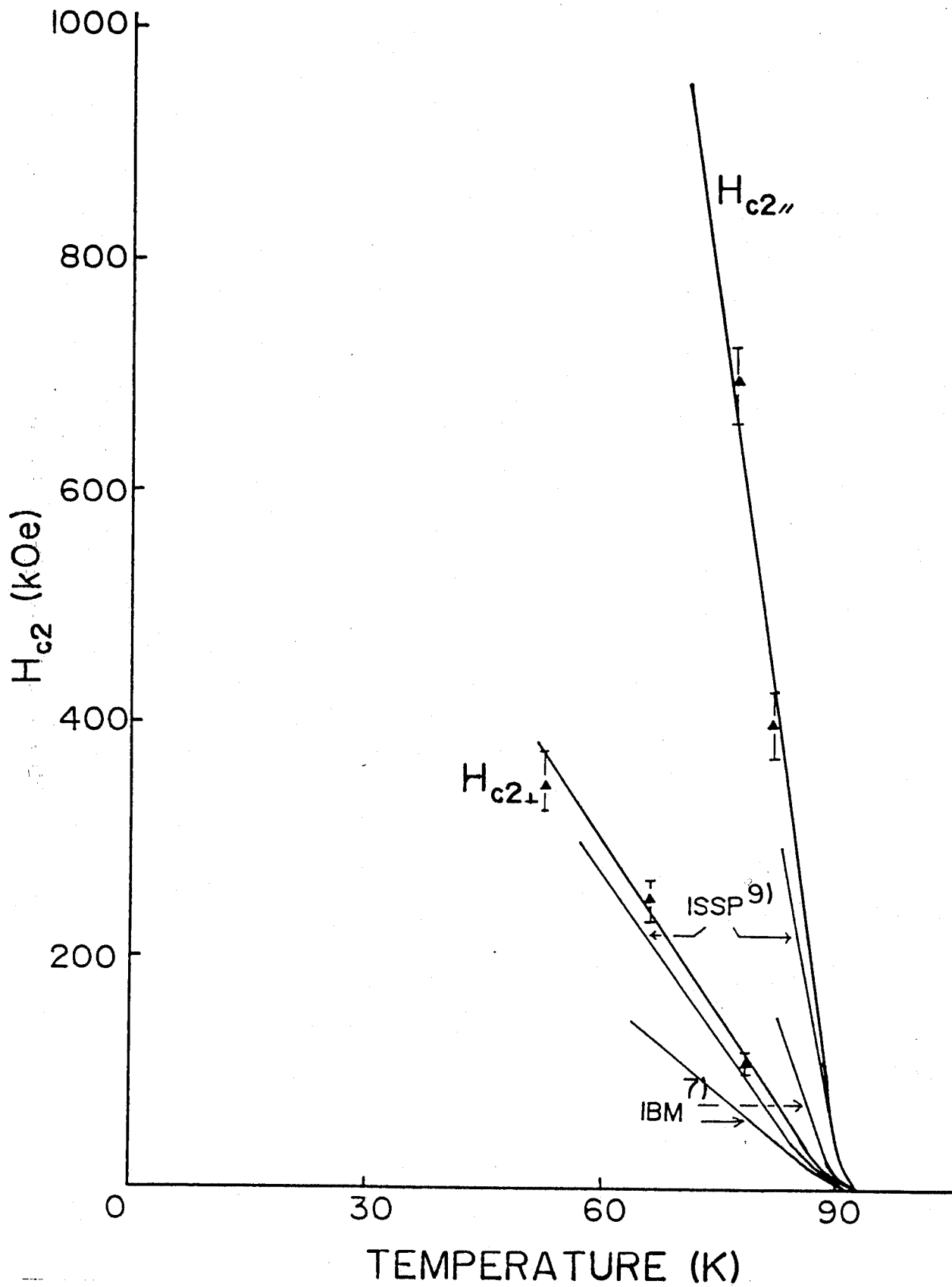


Fig. 64. Temperature dependence of $H_{c2\parallel}$ and $H_{c2\perp}$ in $\text{YBa}_2\text{Cu}_3\text{O}_y$ obtained from the polycrystalline datum. The corresponding single crystal data are also shown.

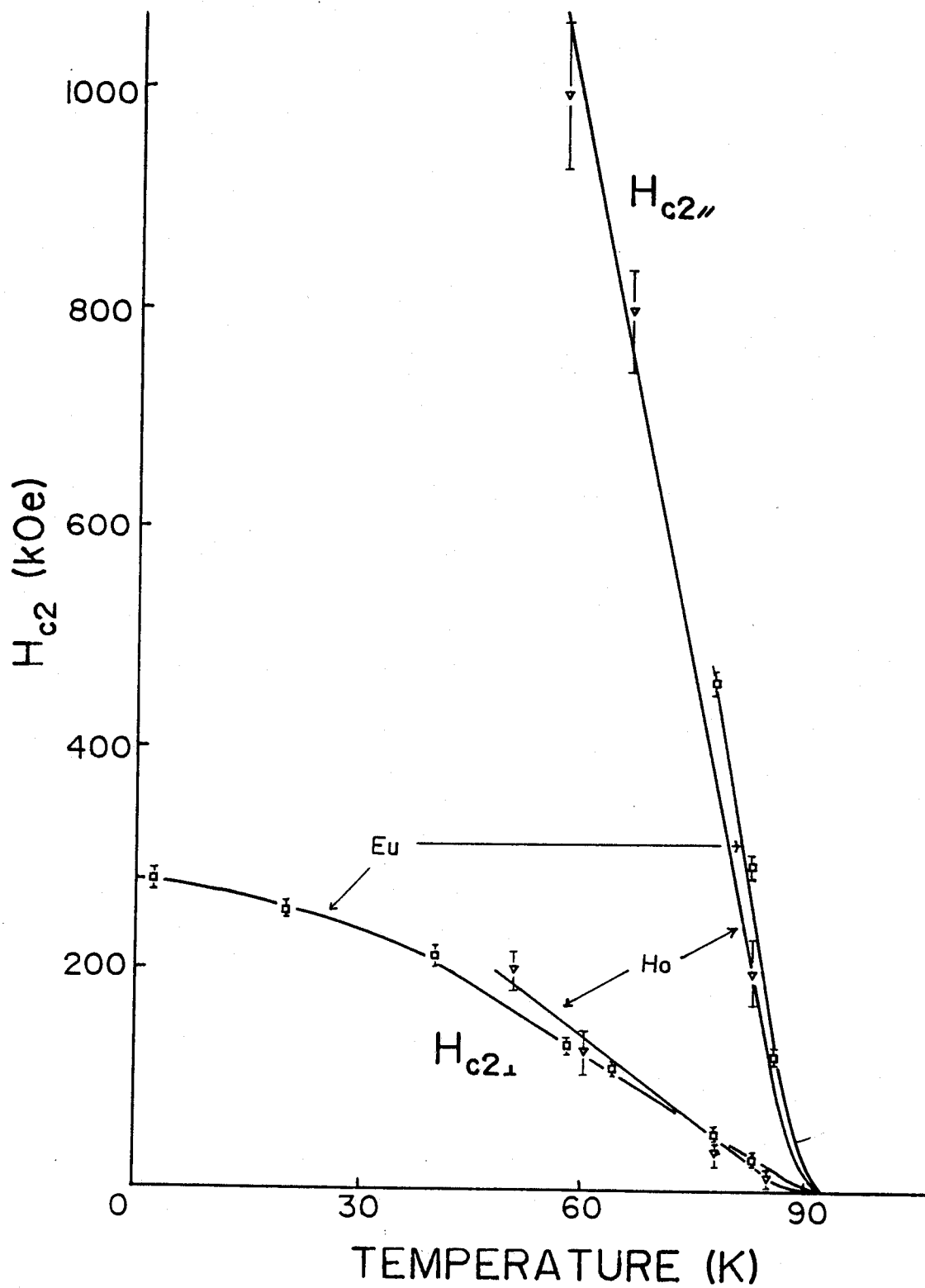


Fig. 65. Temperature dependence of $H_{c2\parallel}$ and $H_{c2\perp}$ in $\text{HoBa}_2\text{Cu}_3\text{O}_y$ and $\text{EuBa}_2\text{Cu}_3\text{O}_y$.

$H_{c2\parallel}$ and $H_{c2\perp}$ are listed in the Table V with the calculated coherent length ξ_{\parallel} and ξ_{\perp} .

The $dH_{c2\parallel}/dT$ value of 38 kOe/K in the present $\text{EuBa}_2\text{Cu}_3\text{O}_y$ crystal is almost the same as the previously reported values of 38 kOe/K⁷⁾ and 33 kOe/K⁶⁾ and 39 kOe/K⁹⁾ for single crystal $\text{YBa}_2\text{Cu}_3\text{O}_y$ measurements while $dH_{c2\perp}/dT$ obtained in the present study is 4.1 kOe/K which differs from the previous values of 5.4 kOe/K⁷⁾, 5.6 kOe/K⁶⁾ and 11 kOe/K.⁹⁾ According to the WHH theory, dH_{c2}/dT is strongly dependent on resistivity. Orlando et al. investigated the relation between ρ and dH_{c2}/dT by using sintered powder samples and concluded that dH_{c2}/dT does not depend on ρ .¹⁰⁾ However, it is difficult to measure the intrinsic value of ρ in the sintered powder samples because the powder samples consist of micro-crystal with various crystal orientations and void. The difference of $dH_{c2\perp}/dT$ in various single crystal seems to depend on ρ . The observed ρ in the present study near T_c is $170 \mu\Omega\text{cm}$ (-4.1 kOe/K) which is lower than the previously reported value of $800 \mu\Omega\text{cm}$ (-11 kOe/K) for $\text{YBa}_2\text{Cu}_3\text{O}_y$ ⁹⁾ and of $410 \mu\Omega\text{cm}$ (-7 kOe/K) for $\text{EuBa}_2\text{Cu}_3\text{O}_y$.⁸⁾ It may be said that highly qualified material shows a low $dH_{c2\perp}/dT$ value.

The coherent length tensor is calculated from the estimated $H_{c2\perp}(0)$ and $H_{c2\parallel}(0)$ data using the relations given by

$$H_{c2\perp} = \Phi_0 / 2\pi \xi_{\parallel}^2, \quad H_{c2\parallel} = \Phi_0 / 2\pi \xi_{\perp} \xi_{\parallel}, \quad (4.1)$$

where Φ_0 is the flux quantum. The obtained values are

Table V Parameters of $\text{RBa}_2\text{Cu}_3\text{O}_{7-\delta}$

R	Eu		Ho	Y			
Research group	NTT-OU (single)	NTT ⁸⁾ (single)	NTT-OU (poly)	NTT-OU (poly)	ISSP ⁹⁾ (single)	IBM ⁷⁾ (single)	NTT ⁶⁾ (single)
T _c (mld) (K)	94	94.8	91	91	92	88.8	92
ρ(100K) (μΩcm)	170	410			800		200
$\frac{dH_{C2}^{\perp}}{dT}(\frac{kOe}{K})$	4.1	7	6	11	11	46	56
$\frac{dH_{C2}^{\parallel}}{dT}(\frac{kOe}{K})$	38	30	32	56	39	23	33
H _{C2} [⊥] (kOe)	275	450	380	690	630	290	350
H _{C2} [∥] (kOe)	2450	1900	2000	3500	2400	1400	2100
ξ [⊥] (Å)	3.8	6.0	5.4	4.4	6.0	7.0	5.0
ξ [∥] (Å)	35	27	31	21	22	34	30

OU means our group. The data are given in the references.

$$\xi_{//}(0) = 35 \text{ \AA} , \quad \xi_{\perp}(0) = 3.8 \text{ \AA} . \quad (4.2)$$

It is noted that the two-dimensional behavior is not denied because ξ_{\perp} is much smaller than the unit cell length along the c-axis.²⁷⁾ The observed ξ_{\perp} value is critical²⁸⁾ even if the Cu-O chain were responsible for the superconductivity. Although three-dimensional behavior is reported by Freitas et al.,²⁹⁾ the possibility of two-dimensional character and dimensional crossover should be investigated in future. The observed anisotropic ratio of $H_{c2//}/H_{c2\perp}$ is 9.3 at 80 K in accord with previously reported data³⁰⁾ of the reciprocal ratio, $H_{c1\perp}/H_{c1//} = 10$. This fact means that the anisotropic GL-theory can be applicable to the 123-compounds.

Figure 66 shows the temperature dependence of the magnetoresistance. It is found that the T_c decrease with increasing magnetic field and no superconducting transition is found above 400 kOe. The zero field normal resistivity curve in the c-plane can be drawn by combining the high field results with the data above T_c as is shown in Fig.67 where the observed linear and positive magnetoresistance is subtracted from the high field data and the residual resistivity is estimated as 55 $\mu\Omega\text{cm}$. With the exception of magnetoresistance the outline of $\rho(T)$ can be understood by the normal model. The linear magnetoresistance is a little unusual but is sometimes found in magnetic materials.³¹⁾ The spin fluctuation effect, i.e. negative magnetoresistance³²⁾ is not found. The obtained normal state magnetoresistance is shown in Fig.68.

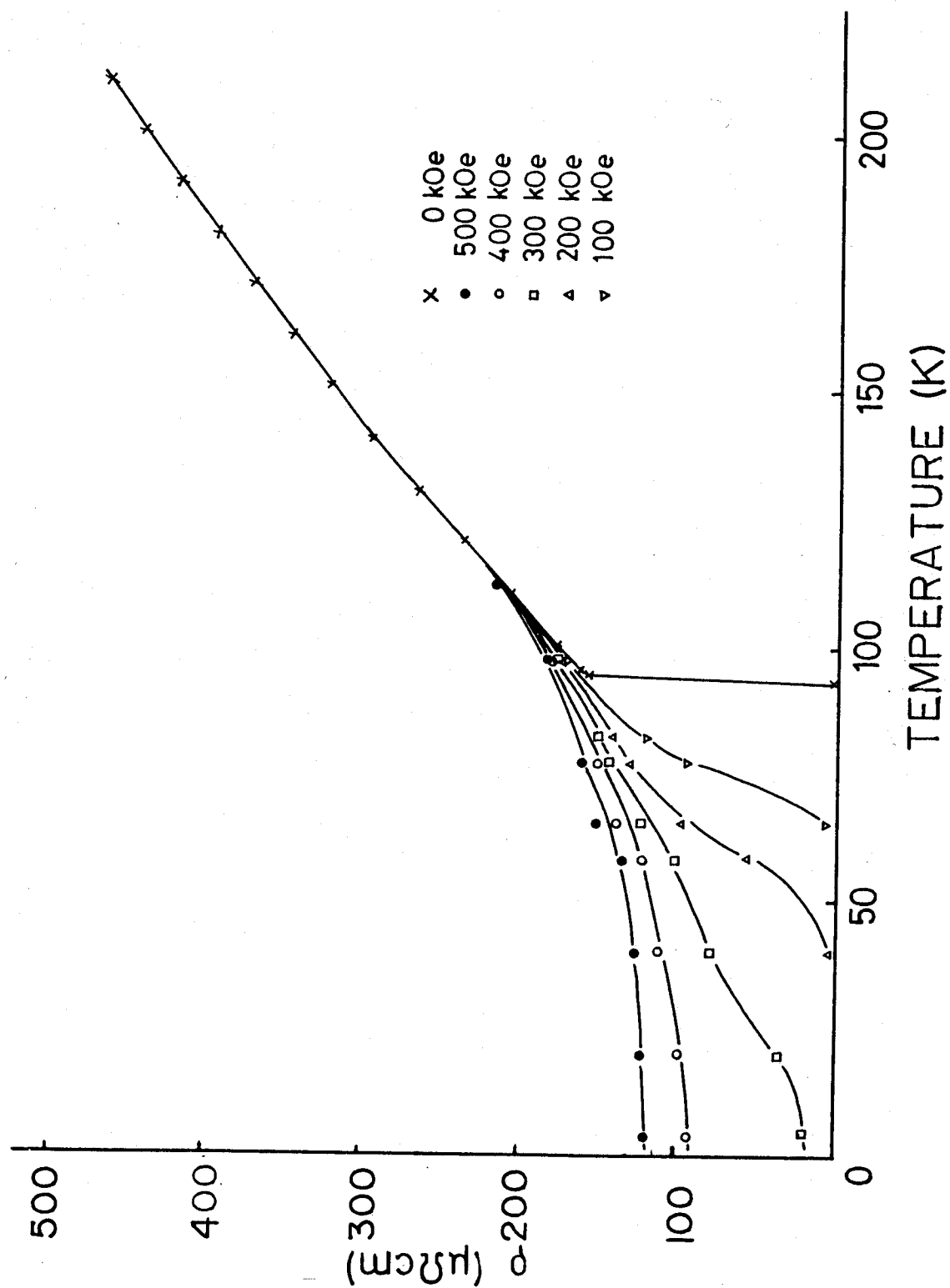


Fig. 66. Temperature dependence of the magnetoresistance in $\text{EuBa}_2\text{Cu}_3\text{O}_y$ ($H_0 \perp c\text{-plane}$).

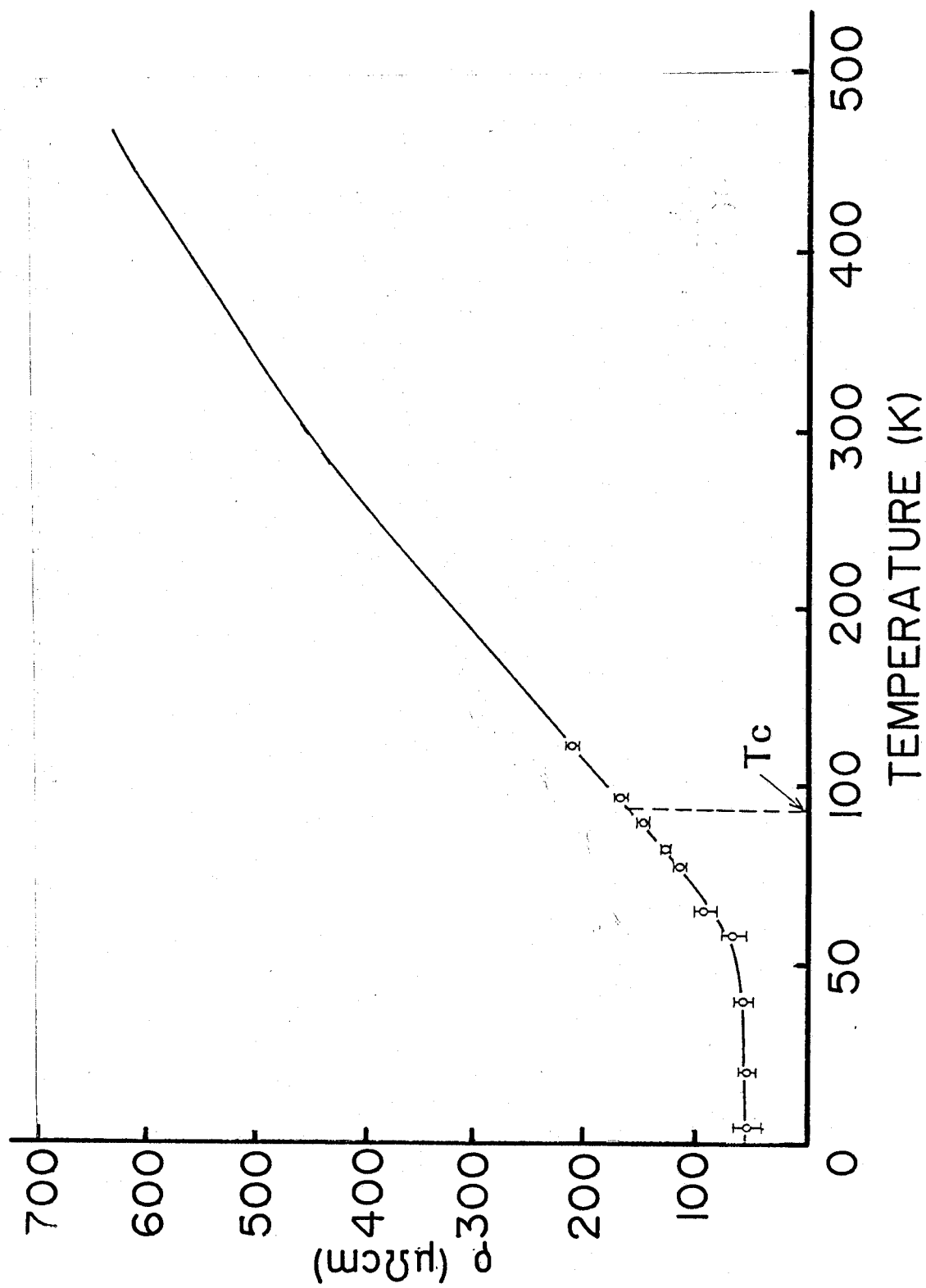


Fig. 67. Estimated normal resistance of $\text{EuBa}_2\text{Cu}_3\text{O}_y$.

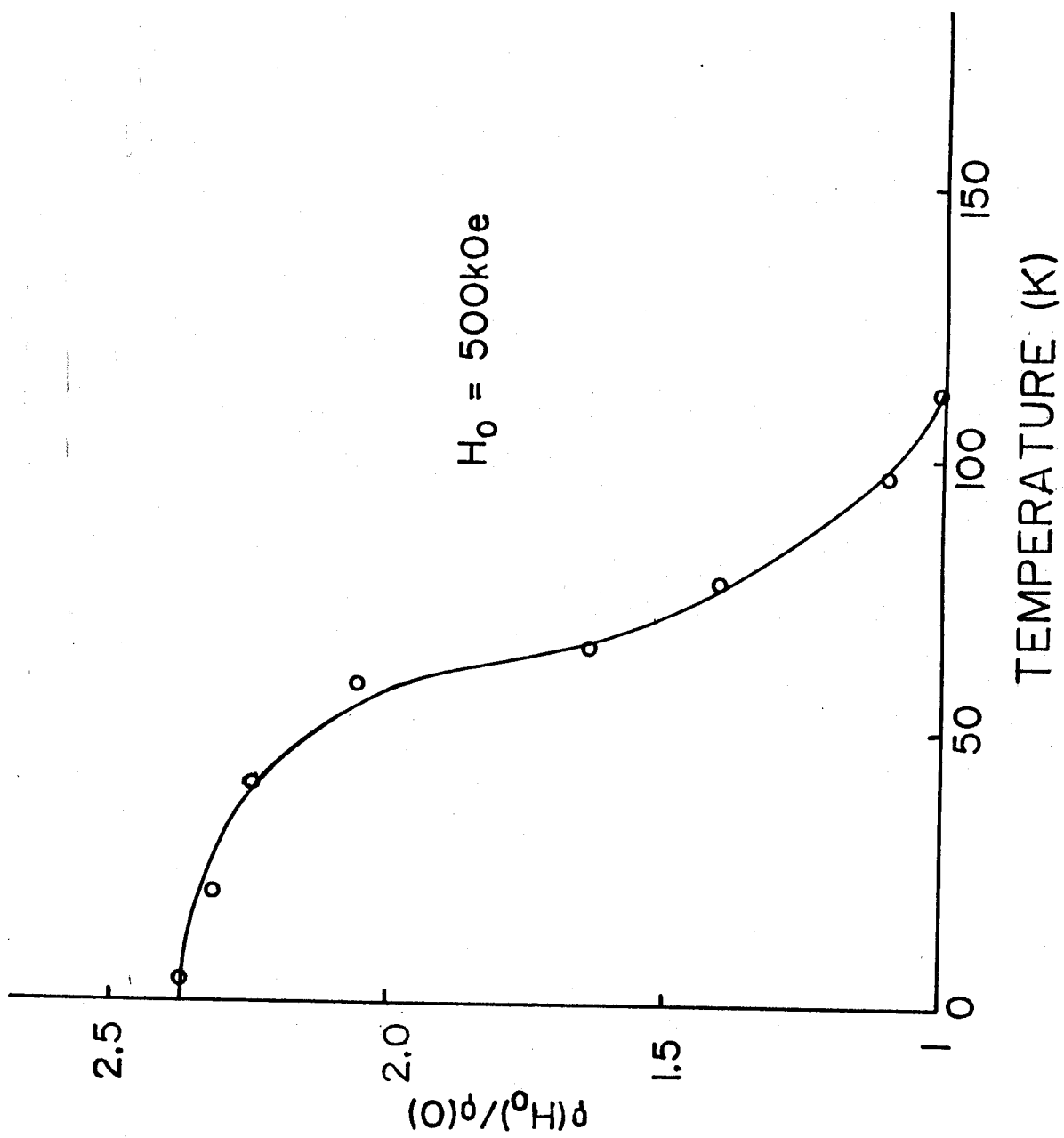


Fig. 68. Temperature dependence of the normal state magnetoresistance in $\text{EuBa}_2\text{Cu}_3\text{O}_y$ ($H_0 \perp c\text{-plane}$).

In conclusion, it should be noted that a highly qualified single crystal of $\text{EuBa}_2\text{Cu}_3\text{O}_y$ shows a clear type-II superconductivity under a strong magnetic field up to 500 kOe. The whole profile of the H_{c2} -T curve shows that the WHH theory based on the BCS dirty limit model well explains the experimental results whose coherent lengths are $\xi_{\parallel} = 35$ Å and $\xi_{\perp} = 3.8$ Å. The whole aspect of the in-plane normal resistivity down to liquid helium temperature does not show any peculiarity and the magnetoresistance is positive. The remaining or rather enhanced problem is why the superconducting critical temperature T_c is so high in such a "normal" metal.

REFERENCES

- 1) J. G. Bednorz and K. A. Muller: Z. Phys. B64 (1986) 186.
- 2) M. K. Wu, J. R. Ashburn, C. J. Torng, P. H. Hor, R. L. Merg, L. Gao, Z. J. Huang, Y. Q. Wang and C. W. Chu, Phys. Rev. Lett. 58 (1987) 908.
- 3) T. W. Worthington, W. J. Gallagher and T. R. Dinger: Phys. Rev. Lett. 59 (1987) 1160.
- 4) Y. Iye, T. Tamegai, H. Takeya and H. Takei: Jpn. J. Appl. Phys. 26 (1987) L1057.
- 5) H. Noel, P. Gougeon, J. C. Levet, M. Potel, O. Laborde and P. Monceau: Solid State Commun. 63 (1987) 915.
- 6) Y. Hidaka, M. Oda, M. Suzuki, A. Katsui, T. Murakami, N. Kobayashi and Y. Muto: to be published in Physica B (1988).
The Proceeding of the Yamada Conference XVIII on Superconductivity in Highly Correlated Fermion Systems.
- 7) W. J. Gallagher, T. K. Worthington, T. R. Dinger, F. Holtzberg, D. L. Kaiser, and R. L. Sandstrom: to be published in Physica B (1988). The Proceeding of the Yamada Conference XVIII on Superconductivity in Highly Correlated Fermion Systems.
- 8) M. Kikita, Y. Tajima, A. Katsui, Y. Hidaka, T. Iwata and S. Tsurumi: Phys. Rev. B36, Nov.(1987).
- 9) T. Sakakibara, T. Goto, Y. Iye, N. Miura, H. Takeya and H. Takei: Jpn. J. Appl. Phys. 26 (1987) L1892.
- 10) T. P. Orlando, K. A. Delin, S. Foner, E. J. McNiff, Jr., J. M. Tarascon, L. H. Greene, W. R. McKinnon and G. H. Hull: Phys. Rev. B36 (1987) 2394.

- 11) K. Okuda, S. Noguchi, A. Yamagishi, K. Sugiyama and M. Date:
Jpn. J. Appl. Phys. 26 (1987) L822.
- 12) M. Oussena, S. Senoussi, G. Collin, J. M. Broto, H. Rakoto,
S. Askenazy and J. C. Ousset: Phys. Rev. B36 (1987) 4014.
- 13) L. F. Mattheiss and D. R. Hamann: Solid State Commun. 63
(1987) 395.
- 14) S. Massidda, J. Yu, A. J. Freeman and D. D. Koelling: Phys.
Lett. A122 (1987) 198.
- 15) For example, P. W. Anderson: Science 235 (1987) 1196, P. A.
Lee and N. Reed: Phys. Rev. Lett. 58 (1987) 2691.
- 16) S. Hikami, T. Hirai and S. Kagoshima: Jpn. J. Appl. Phys. 26
(1987) L314.
- 17) R. J. Cava, B. Batlogg, R. B. van Dover, D. W. Murphy, S.
Sunshine, T. Siegrist, J. P. Remeika, E. A. Rietman, S.
Zahurak and G. P. Espinosa: Phys. Rev. Lett. 58 (1987) 1676.
- 18) P. M. Grant, R. B. Beyers, E. M. Enger, G. Lim, S. S. P.
Parkin, M. L. Ramirey, V. Y. Lee, A. Nazzal, J. E. Vargueyand
R. J. Savoy: Phys. Rev. B35 (1987) 7242.
- 19) K. Semba, S. Tsurumi, M. Hikita, T. Iwata, T. Noda and S.
Kurihara: Jpn. J. Appl. Phys. 26 (1987) L429.
- 20) H. Takagi, S. Uchida, H. Sato, K. Kishio, K. Kitazawa, K.
Fueki and S. Tanaka: Proc. 18th Int. Conf. on Low Temperature
Physics, Kyoto. 1987. J. Appl. Phys. Suppl. 26-3 (1987) 1029.
- 21) F. Isumi, H. Asano, T. Ishigaki, E. T. Muromachi, Y. Uchida,
N. Watanabe and T. Nishikawa: Jpn. J. Appl. Phys. 26 (1987)
L649.
- 22) A. Katsui, Y. Hidaka and H. Ohtsuka: Jpn. J. Appl. Phys. 26
(1987) L1521.

- 23) Y. Hidaka, Y. Enomoto, M. Suzuki, M. Oda and T. Murakami: to be published in J. Crystal Growth Nov/Dec(1987).
- 24) J. L. Vicent, S. J. Hillenius and R. V. Coleman: Phys. Rev. Lett. 44 (1980) 892.
- 25) B. J. Dalymple and D. E. Prober: J. Low. Temp. Phys. 56 (1987) 545.
- 26) N. R. Werthaner, E. Helffand and P. C. Hohenberg: Phys. Rev. 147 (1966) 295.
- 27) T. Iwata, M. Hikita, Y. Tajima and S. Tsurumi: to be published in J. Crystal Growth Nov/Dec(1987).
- 28) R. A. Klemm, A. Luther and M. R. Beasley: Phys. Rev. B12 (1975) 877.
- 29) P. P. Freitas, C. C. Tsuei and T. S. Plaskett: Phys. Rev. B36 (1987) 833.
- 30) T. R. Dinger, T. K. Worthington, W. J. Gallagher and R. L. Sandstrom: Phys. Rev. Lett. 58 (1987) 2687.
- 31) K. Kadowaki, K. Okuda and M. Date: J. Phys. Soc. Jpn. 51 (1982) 2433.
- 32) T. R. McGuire, T. R. Dinger, P. J. Freitas, W. J. Gallagher, T. S. Plaskett, R. L. Sandstrom and T. M. Show: Phys. Rev. B36 (1987) 4032.

ACKNOWLEDGEMENTS

The author wishes to express his sincere gratitude to Professor Muneyuki Date for his valuable suggestions and enlightening discussions, and for his continuous encouragement throughout the present work.

Thanks are also due to Professor Akio Yamagishi for his valuable suggestions and many stimulating discussions.

The author would like to thank Professor Tadao Kasuya, Professor Mitsuo Kasaya and Dr. Satoru Kunii of Department of Physics, Faculty of Science, Tohoku University for supplying GdB_6 and YbB_{12} crystals and for their valuable suggestions about the problem. He would also like to thank Dr. Makoto Hikita, Dr. Yukimichi Tajima and Takao Ishii of NTT Laboratory for supplying high- T_c superconductors and their helpful discussions about the problem.

He is indebted to Mr. Akihiko Ohya, Mr. Yukio Koyoshi, Mr. Hiroyuki Fuke and Mr. Osamu Kondo for the cooperation in the magnetization and magnetoresistance measurements. He is also indebted to Mr. Kenji Shimohata and Mr. Kenji Yonenobu for the cooperation in the development of long-pulse magnet. He is also indebted to Mr. Kimikazu Hazumi and Mr. Mitsuru Ono for the cooperation in the development of data processing system. Finally, the author wishes to thank all the member of Date laboratory.